NTNU
Norwegian University of
Science and Technology

Numerical Simulation of Flow Around a Prolate Spheroid

Stian Nevland

Norwegian University of Science and Technology
Department of Marine Technology

NTNU
Norwegian University of Science and Technology
Department of Marine Technology

MASTER THESIS IN MARINE HYDRODYNAMICS

FALL 2016

FOR

Stud.techn. Stian Nevland

NUMERICAL SIMULATION OF FLOW AROUND A PROLATE SPHEROID
(Numerisk simulering av strømning omkring en rotasjons spheroide)

The candidate shall investigate the wake flow behind prolate spheroids. A sphere can be a good starting point, where results can be compared with data available in the literature. Choice of design parameters can be motivated by the newly published concept from Marin Harvest ("egget").
The CFD code OpenFOAM shall be used to map the wake flow in detail. Different Reynolds numbers shall be chosen. All choices of parameters must be documented and argued for.

In the thesis the candidate shall present his personal contribution to the resolution of the problem within the scope of the thesis work. Theories and conclusions should be based on mathematical derivation and logic reasoning identifying the various steps in the deduction. The original contribution of the candidate and material taken from other sources shall be clearly defined. Work from other sources shall be properly referenced. The candidate should utilize the existing possibilities for obtaining relevant literature.
The thesis should be organized in a rational manner to give a clear exposition of results, assessments and conclusions. The text should be brief and to the point, with a clear language.

The thesis shall contain the following elements: A text defining the scope, preface, list of contents, summary, main body of thesis, conclusions with recommendations for further work, list of symbols and acronyms, references and appendices. All figures, tables and equations shall be numerated.
It is supposed that Department of Marine Technology, NTNU, can use the results freely in its research work by referring to the student's thesis.
The thesis shall be submitted February 12th, 2017.

Bjørnar Pettersen
Professor/supervisor

Abstract

The concept of closed containment fish cages is promising when coping with sea lice and escaped fish challenges in the aquaculture industry. Unlike the traditional open net cages, the external flow caused by current and waves has to flow entirely around the fully closed walls. Hence, the importance to consider the hydrodynamic loads, as well as the behavior of the disturbed flow.

In the present study, a closed containment fish cage has been simplified as a ($L_R = L/D$ = 4/3) prolate spheroid. The model is assumed fully submerged in a steady current, and oriented with its major axis normal to the incoming flow. The flow has been simulated numerically by a finite volume method in the software OpenFOAM for five different Reynolds numbers, Re = 100, 200, 250, 300 and 500. The resulting pressure, velocity and vorticity fields are presented using various visualization techniques, whereas quantities related to hydrodynamic force coefficients, separation and vortex shedding frequencies are computed. Due to the low aspect ratio, the main goal of the present study was to relate the present results to flow features appearing in the wake of a sphere.

For the two lowest Reynolds numbers Re = 100 and 200, the flow was found to be steady and symmetric in the major plane. At the former Re, a similar planar symmetry aligned with the minor plane of the prolate spheroid was observed. The flow separates and rejoins a certain distance downstream. A maximum separation length equal to $L_s = 1.26D$ and $1.75D$ was obtained for Re = 100 and 200, respectively.

An unsteady wake flow was apparent for Reynolds numbers $Re \geq 250$, with consequent oscillating hydrodynamic forces. At Re = 250, a pair of counter-rotating vortices were found to twist around each other as they propagate downstream. The most striking discovery, relating the present results to the flow around a sphere, is the periodic shedding of hairpin-shaped vortices of constant orientation, at Re = 300. The topology of the vortical structures, as well as the associated shedding frequency, were found to coincide with the results of a sphere. A planar symmetry is evident and aligned with the major axis of the L_R = 4/3 prolate spheroid. As a Reynolds number of Re = 500 is reached, the symmetry features of the wake are lost. Unlike the vortex structures of fixed orientation at Re = 300, the present visualizations at Re = 500 revealed a chaotic wake of alternately shed vortices. The dominant shedding frequency in terms of Strouhal number, St = 0.137 and 0.183, were found for Re = 300 and 500, respectively.

The resemblance between the results of the L_R = 4/3 prolate spheroid and the sphere was found to be strong concerning hydrodynamic force coefficients and separation. At Re = 300 an averaged drag and lift coefficient of $C_D' = 0.664$ and $C_L' = 0.052$ were computed after the flow had reached a steady state. For increasing Re, the point of separation was found to move upstream. The separation angle from the front stagnation point in the middle minor plane decreased from 121° at Re = 100 to 103° at Re = 500.

The outline of the wake $1D$ behind the prolate spheroid was found to maintain its projected area at all Re. However, at the two highest tested Reynolds numbers, the major axis of the wake was found to rotate and align with the minor axis of the prolate spheroid, somewhere between $4D$ and $7D$ downstream. A comparable axis switching phenomenon has been reported for similar asymmetric bodies as a L_R = 6 prolate spheroid and L_R = 3 elliptic disk.

Therefore, the present results indicate that flow features appearing in the wake of a

sphere are maintained for the low aspect ratio ($L_R = 4/3$) prolate spheroid, at the tested Re. However, the presence of an asymmetric cross-section is seen to introduce similarities toward results of higher aspect ratio bluff bodies.

For further work, it is recommended to increase the practical relevance of the numerical simulations. This may be done by increasing the Reynolds number to simulate turbulent flow or change the boundary conditions to introduce e.g. a free surface or a shallow water condition.

Sammendrag

Lukkede oppdrettsanlegg er et lovende konsept for å takle utfordringer innen akvakultur, relatert til lakselus og rømming av fisk. I motsetning til tradisjonelle åpne notposer må innkommende bølger og undervannsstrømninger strømme fullstendig rundt de lukkede veggene. Derav viktigheten av å betrakte de hydrodynamiske kreftene og kjølvannets oppførsel.

I dette studiet har et kjent lukket opprdretsanlegg blitt forenklet som en prolat sfæroide med lengde/bredde-forhold $L_R = 4/3$. Modellen er totalt nedsenket i en jevn vannstrøm, og med den lengste aksen plassert perpendikulært i forhold til den innkommende strømningen. Numeriske simuleringer har blitt gjennomført i programvaren OpenFOAM, ved fem forskjellige Reynoldstall, henholdsvis $Re = 100, 200, 250, 300$ og 500. Resulterende trykk, hastighet og vortisitet er visualisert ved hjelp av respektive metoder, mens hydrodynamiske koeffisienter, separasjonpunkt og virvelavløsningsfrekvens er gitt som tallsvar. Hovedmålet med studiet har vært å relatere resultatene fra en prolat sfæroide med lavt aspektforhold med resultatene til en sfære.

For de to laveste Reynoldstallene $Re = 100$ og 200 ble det funnet et stabilt og stasjonært strømningsbilde med et symmetriplan parallelt med sfæroidens lengste akse. Ved det laveste Reynoldstallet $Re = 100$ var strømningsbildet også symmetrisk langs den korteste aksen. Strømnigen rundt sfæroiden separeres fra overflaten og møtes igjen i kjølvannet. Den største avstanden fra bakenden av legemet til der den separerte strømningen gjenforenes ble funnet lik $1.26D$ og $1.75D$ for henholdsvis $Re = 100$ og 200.

Fra og med Reynoldstall 250 ble det observert en ustabil strømning i kjølvannet som resulterte i en oscillerende løft- og dragkraft på legemet. Ved $Re = 250$ dannes et par kontraroterende virvler i kjølvannet som vrir seg om hverandre etterhvert som de beveger seg nedstrøms. Den mest oppsynsvekkende oppdagelsen som relaterer studiets resultater til strømningen rundt en sfære, er dannelsen av en periodisk virvelavløsning, bestående av hårnålformede virvler med konstant retning ved $Re = 300$. Både formen til virvelstrukturene og virvelavløsningsfrekvensen sammenfaller med resultatene til en sfære. Ved dette Reynoldstallet er et symmetriplan synlig i kjølvannet, og på linje med den største aksen til sfæroiden. Ved det høyeste Reynoldstallet $Re = 500$ ble et langt mer uryddig kjølvann observert med ingen synlig symmetri og en virvelavløsning av varierende retning, i motsetning til de konstante virvelstrukturene ved $Re = 300$. Virvelavløsningsfrekvensen ved $Re = 300$ og 500 ble funnet til henholdsvis $St = 0.137$ og 0.183.

Resultatene av en $L_R = 4/3$ prolat sfæroide og en sfære viste en klar likhet ved de kalkulerte hydrodynamiske kreftene og separasjonspunktene ved de testede Reynoldstallene. Ved $Re = 300$ ble en gjennomsnittlig drag- og løftkoeffisient funnet til $C_D' = 0.664$ og $C_L' = 0.052$, utregnet etter at strømningen hadde blitt periodisk. For et økende Reynoldstall ble separasjonspunktet om sfæroiden funnet å bevege seg oppstrøms. Vinkelen mellom det fremre stagnasjonspunktet og separasjonspunktet avtok fra $121°$ ved $Re = 100$ til $103°$ ved $Re = 500$.

Omrisset av kjølvannet lokalisert $1D$ nedstrøms var lik det projiserte tverrsnittet av sfæroiden for alle Re. For de to høyeste Reynoldstallene ble imidlertid den lengste aksen til omrisset av kjølvannet rotert slik at den ble parallell med den korteste aksen til sfæroiden, et sted mellom $4D$ og $7D$ nedstrøms. Et tilsvarende akseskift er funnet for lignende asymmetriske legemer som en $L_R = 6$ prolat sfæroide og en $L_R = 3$ elliptisk plate.

Derfor er det konkludert at flere av egenskapene til strømningen rundt en kule er ivaretatt for en ($L_R = 4/3$) prolat sfæroide med lavt aspektforhold ved de testede Reynoldstallene. Samtidig vil det asymmetriske tverrsnittet til sfæroiden føre til likheter sammenlignet med legemer av høyere aspektforhold.

For videre arbeid er det anbefalt å øke den praktiske tilnærmingen til de numeriske simuleringene. Dette kan eksempelvis gjøres ved å simulere turbulent strømning, eller ved å endre randbetingelsene slik at en fri-væskeoverflate eller grunt vann simuleres.

Preface

This report presents the final results of a master thesis in marine hydrodynamics for Marine Technology, at the Norwegian University of Science and Technology (NTNU). The master thesis is the final work of a five-year M.Sc. of Engineering Science and Technology. Numerical simulations of the three-dimensional flow around a prolate spheroid have been performed in the software OpenFOAM.

The topic of the assignment was outlined by my supervisor, Professor Bjørnar Pettersen. Ever since the commence of my project thesis, at the beginning of spring semester 2016, Pettersen has been very helpful with recommendations and inspiring with his continuous enthusiastic attitude towards the subject. In addition to providing challenging objectives, he has been supportive of my ideas and suggestions.

Before my final year at Marine Technology, I had no experience with the software Open-FOAM. Therefore, a significant part of the work has involved acquiring knowledge of the pre- and post-processing techniques included in Computational Fluid Dynamics. Regarding the mesh generation software Mega, I would like to thank Professor Håvard Holm for his time and willingness to help solve the issues I have faced throughout the duration of my work.

Due to the demanding numerical simulations, the present study has not been possible without high-performance computations at the supercomputer Vilje. I am truly grateful to Dr. Tufan Arslan for providing me with an in-depth introduction on how to run an OpenFOAM case on Vilje.

Trondheim, February 2017

Stian Nevland

Contents

Nomenclature

Latin letters

a	parameter defining the domain size
A	reference area, m^2
C_D	drag coefficient $= F_D/0.5\rho U_\infty^2 A$
C_L	lift coefficient $= F_L/0.5\rho U_\infty^2 A$
ΔC_D	drag coefficient amplitude $= (C_D^{max} - C_D^{min})/2$
ΔC_L	lift coefficient amplitude $= (C_L^{max} - C_L^{min})/2$
$C_D^{'}$	averaged drag coefficient $= F_D^{'}/0.5\rho U_\infty^2 A$
$C_L^{'}$	averaged lift coefficient $= F_L^{'}/0.5\rho U_\infty^2 A$
dx, dy, dz	infinitesimal length in x, y and $z-$direction, respectively
dr	infinitesimal arc lengt
D	diameter of cylinder/sphere/spheroid, m
f	cell face
f_v	vortex shedding frequency, s^{-1}
$F_D, F_D^{'}$	drag force and average drag force, N
$F_L, F_L^{'}$	lift force and average lift force, N
$F_{inertial}$	inertial force, N
$F_{viscous}$	viscous force, N
$\vec{i}, \vec{j}, \vec{k}$	unit vector in x, y and $z-$direction, respectively
L	length of spheroid/cylinder, m
L_R	spheroid/cylinder aspect ratio $= L/D$
L_s	separation length, m
L_x, L_y, L_z	domain length in x, y and $z-$direction, respectively
$\vec{n}$	normal vector
$p, p^{'}$	pressure and averaged pressure, N/m^2
Re	Reynolds number $= U_0 D/\nu$
Re_c	critical Reynolds number
S	cell surface
$\vec{S_c}$	vector connecting cell centres
$\vec{S_f}$	face normal vector
S_{ij}	strain rate tensor, s^{-1}
St	Strouhal number $= f_v D/U_0$
t	time, s
Δt	time step, s

u, v, w	velocity in x, y and $z-$direction, respectively, m/s
U, V	magnitude of local velocity, m/s
$\mathbf{U}, \vec{U}, \vec{V}$	velocity vector
U_0, U_∞, V_0	free stream velocity, m/s
x, y, z	Cartesian coordinates
$\Delta x, \Delta y, \Delta z$	cell length in x, y and $z-$direction, respectively
$*, **, * * *$	denotes temporary parameters in the PISO algorithm

Greek letters

δ	boundary layer thickness, m
δ_{ij}	Kronecker delta function
θ_s	angle between front stagnation point and separation point in (x,y)-plane
λ_2	second largest eigenvalue of the tensor $S_{ij}S_{ij} + \Omega_{ij}\Omega_{ij}$
Λ	cell aspect ratio
ν	kinematic viscosity, m^2/s
ρ	fluid density, kg/m^3
$\nabla, \vec{\nabla}$	differential operator
σ_{ij}	stress tensor, N/m^2
ϕ_s	angle between front stagnation point and separation point in (x,z)-plane
Ω	control volume
$\omega_x, \omega_y, \omega_z$	vorticity components in x, y and $z-$direction, respectively.
Ω_{ij}	vorticity tensor
$\vec{\omega}$	vorticity vector

Abbreviations

CFD	computational fluid dynamics
CFL	Courant-Friedrich-Lewy number
DNS	direct numerical simulation
FFT	Fast Fourier Transform
FVM	finite volume method
NTNU	Norwegian University of Science and Technology
PDE	partial differential equations
RMS	root-mean-square
VIV	vortex induced vibrations
UV	ultraviolet

Chapter 1

Introduction

1.1 Motivation and Background

Along with the increase in computational power, the numerical simulation of fluid flow has become a necessary tool in engineering design. Typical applications in marine technology have been in the design of bluff body structures. According to Zdravkovich (1997), a bluff body can be defined as a body that, from the result of its shape, separates the flow and develops similar flow structures in the regions of disturbed flow. The two most commonly studied bluff bodies are the sphere and the circular cylinder, which are frequently encountered in industry. For instance, cylinders as risers connecting the oil reservoir to the top side, submarine pipelines with a free span, subsea installations and the hull of platforms in the offshore oil industry. As well as the fish nets in marine aquaculture, consisting of twines and knots, simulated as cylinders connected by spheres having the shape of a cross (cruciform model). The most important flow feature appearing in the wake of bluff bodies is the vortex shedding phenomenon (Sumer and Fredsøe, 1997), which induces oscillating forces. These forces may excite vortex induced vibrations (VIV), which are crucial to include in the design considerations.

1.1.1 Salmon Farming in Norway

According to The Norwegian Ministry of Trade and Fisheries (2014), the aquaculture industry in Norway has turned into an industry of great importance, ever since its commercial advent in the 1970s. The numerous fjords of cold and fresh seawater have ensured excellent conditions for inshore aquaculture. From years of production growth, Norway has become the leading producer of Atlantic salmon worldwide (The Norwegian Ministry of Trade and Fisheries, 2014). However, the Norwegian fish farmers are currently facing a range of challenges. Environmental concerns such as sea lice and escaped fish are threatening a sustainable growth of the industry. Therefore, the Government has decided temporarily not to grant new aquaculture licenses for salmon farming. Instead, in 2015, development concessions were introduced, providing new and promising concepts an opportunity to be put to use. According to the Norwegian Minister of Fisheries, from his 2016 speech at Danske Bank Seafood Seminar, the introduction of development concessions has to lead to a wave of innovation through the industry (Sandberg, 2016).
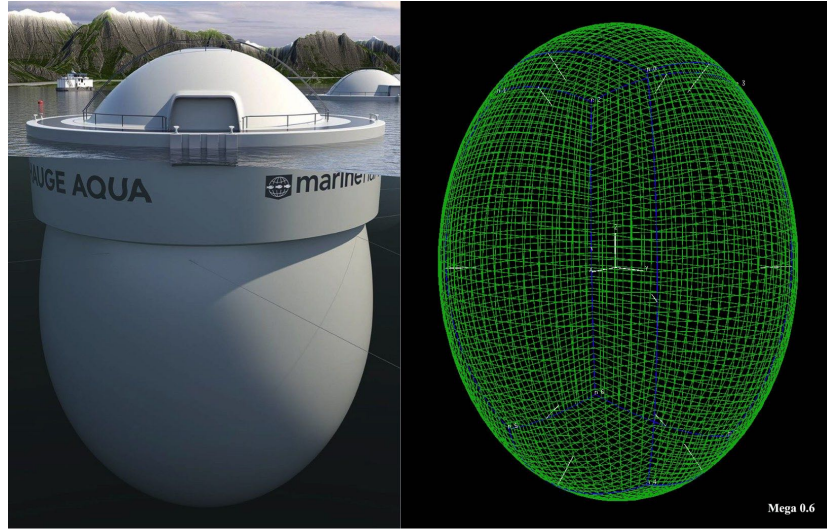
Figure 1.1: Numerical model simplification. (left image) Closed cage fish farm by Hauge Aqua (2016); (right image) computational mesh in Mega.

One of the new and possible solutions to cope with the challenges in marine aquaculture is to build fish cages with fully closed walls. One concept that has raised much attention is "The Egg" developed by Hauge Aqua. In 2016, Marine Harvest and Hauge Aqua signed a joint venture contract for development and testing of the concept (Hauge Aqua, 2016). Recently, it was announced that Marine Harvest has been granted four concessions, leading to the commencement of the production of the concept (Hauge Aqua, 2016).

The shape of the fish cage is well described by its name, depicted in the left image of figure 1.1. The overall height and width are supposed to be 44 *m* and 33 *m*, respectively, with 90 percent of the structure submerged (Hauge Aqua, 2016). Due to the size and shape, it is important to consider the hydrodynamic loads as well as the behavior of the disturbed flow when the fish farm is exposed to current and waves. As shown in figure 1.1, the shape of the fish cage is closely related to a sphere. However, with a major axis slightly longer than the minor. Hence, the value of investigating whether or not the flow around the enclosed fish farm behaves like that of a sphere, or if it resembles the flow features in the wake of higher aspect ratio bluff bodies.

1.1.2 Flow Around a Circular Cylinder

The circular cylinder is one of the most studied body forms in hydrodynamics, and the flow around it has been subject to a vast amount of numerical and experimental research. Based on the value of the Reynolds number, the fluid motion around the cylinder can be divided into several regimes. The Reynolds number represents the ratio between inertial and viscous forces and is defined as:

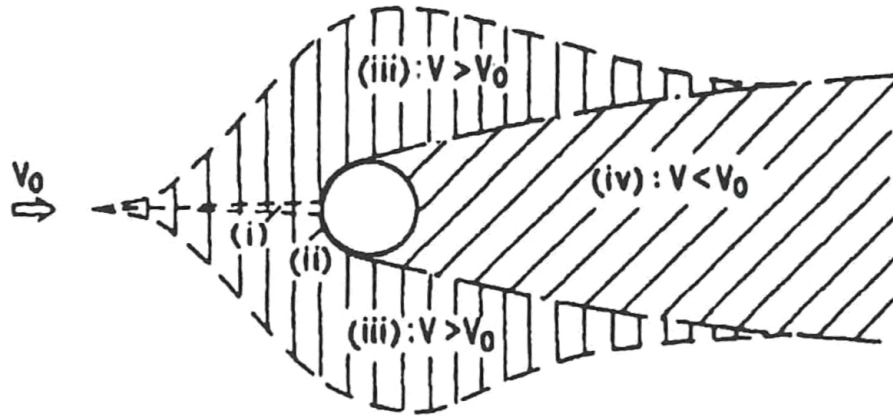$$Re = \frac{U_0 D}{\nu} = \frac{F_{inertial}}{F_{viscous}} \tag{1.1}$$

Figure 1.2: Regions of disturbed flow around a circular cylinder (Zdravkovich, 1997).

where U_0 is the velocity of the undisturbed fluid flow, D is the cylinder diameter and ν is the kinematic viscosity.

In the comprehensive guide through flow phenomena around bluff bodies of circular cross-sections by Zdravkovich (1997), the author divides the disturbed flow into the four following regions:

(i) one narrow region of retarded flow

(ii) two boundary layers attached to the surface of the cylinder

(iii) two side-wise regions of displaced and accelerated flow

(iv) one wide downstream region of separated flow called the wake

The regions of disturbed flow are illustrated in figure 1.2, where the velocity of the undisturbed flow is given by V_0, and the local velocities by V. The first region (i) is a narrow band of retarded flow upstream of the body, containing the stagnation point at the cylinder surface. The no-slip condition gives rise to the second region (ii), which is boundary layers around the cylinder, characterized by large velocity gradients. The boundary layers are attached to the surface until an adverse pressure gradient occurs, and the flow separates from the body. The third region (iii) contains the displaced and accelerated part of the disturbed fluid flow. According to Zdravkovich (1997) this is the least explored region, and it is strongly affected by the absence of walls in the vicinity of the cylinder, known as blockage effects. The wake region (iv) is the most studied part of bluff body flows. The characteristic flow features appearing in the wake are dependent on the Reynolds number, defining whether the flow is laminar, turbulent or in a transition between the two states.

The following description of the flow features appearing in the wake of circular cylinders is suggested by Sumer and Fredsøe (1997). The flow regimes varying with Reynolds number are illustrated in figure 1.3. For $Re < 5$, there is no flow separation, and the flow is attached to the surface over the entire circumference. Hence, no distinct wake region is formed. However, as Re exceeds 5, the flow starts to separate, forming a pair of steady toroidal vortices, until
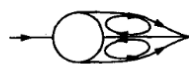
a)	No separation. Creeping flow	$Re < 5$
b)	A fixed pair of symmetric vortices	$5 < Re < 40$
c)	Laminar vortex street	$40 < Re < 200$
d)	Transition to turbulence in the wake	$200 < Re < 300$
e)	Wake completely turbulent. A:Laminar boundary layer separation	$300 < Re < 3 \times 10^5$ Subcritical
f)	A:Laminar boundary layer separation B:Turbulent boundary layer separation;but boundary layer laminar	$3 \times 10^5 < Re < 3.5 \times 10^5$ Critical (Lower transition)
g)	B: Turbulent boundary layer separation;the boundary layer partly laminar partly turbulent	$3.5 \times 10^5 < Re < 1.5 \times 10^6$ Supercritical
h)	C: Boundary layer completely turbulent at one side	$1.5 \times 10^6 < Re < 4 \times 10^6$ Upper transition
i)	C: Boundary layer completely turbulent at two sides	$4 \times 10^6 < Re$ Transcritical

Figure 1.3: Flow around a smooth, circular cylinder in steady current (Sumer and Fredsøe, 1997).

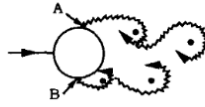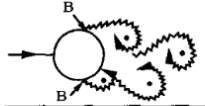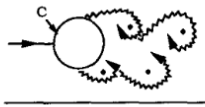a Reynolds number of 40 is reached. As shown in figure 1.3(c), the wake turns unsteady and forms a laminar vortex street for the Reynolds number range $40 < Re < 200$. The street of alternately shed vortices is commonly denoted as a Kármán vortex street. For this Re range, the wake features are considered two-dimensional. However, as the Reynolds number is further increased, the wake gradually turns chaotic, and spanwise variations occur. For Re above approximately 200, the wake is considered to be three-dimensional, with vortices shed in cells along the span of the cylinder (Sumer and Fredsøe, 1997). When $Re > 300$, the wake is completely turbulent. However, the boundary layer at the cylinder surface remains laminar for the entire subcritical flow regime, up to $Re = 3 \times 10^5$, shown in figure 1.3(e). For the supercritical and transcritical regions, in figures 1.3(f-i), the level of turbulence in the boundary layer increases.

The alternating vortices for $Re > 40$ are shed with a certain frequency, dependent on the Reynolds number. To present the shedding frequency as a function of Re, it is normalized by the velocity of the undisturbed fluid flow U_0, and the cylinder diameter D. The normalized
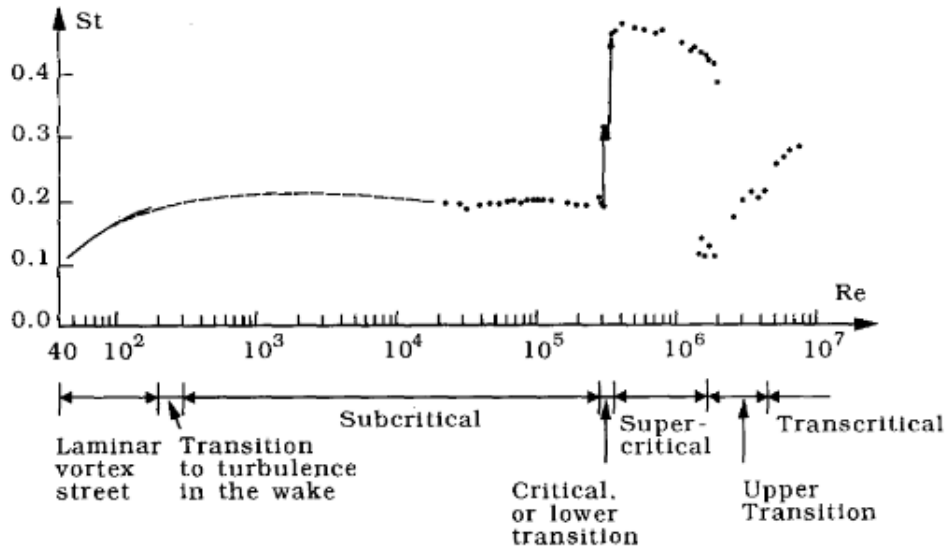
Figure 1.4: Strouhal number over a range of Reynolds numbers for a circular cylinder (Sumer and Fredsøe, 1997).

vortex-shedding frequency is given by the Strouhal number:

$$St = \frac{f_v D}{U_0} \tag{1.2}$$

where f_v is the vortex-shedding frequency. Figure 1.4 shows how the Strouhal number varies with Re, from the laminar vortex shedding, through subcritical, supercritical and up to the transcritical flow regime. The shedding frequency, St, is approximately 0.1 when the vortex shedding first appears. The Strouhal number will steadily increase when Re is increased and attains a value of $St \approx 0.2$ at the lower end of the subcritical flow regime, $Re = 300$. From this value of Re, St will remain more or less constant throughout the subcritical range at the value of 0.2 (Sumer and Fredsøe, 1997).

Mechanism of Vortex Shedding

For Reynolds numbers above 5, the boundary layer flow starts to separate from the cylinder surface, due to an adverse pressure gradient as it approaches the rear part of the body. Because of the strong velocity gradient in the boundary layer, vorticity is fed into the wake, forming a shear layer in the downstream area, as seen in figure 1.5(a). Eventually, the shear layer rolls up and forms a vortex which rotates in the same direction as the incoming vorticity (Sumer and Fredsøe, 1997). Consequently, a vortex pair is formed, one on each side of the cylinder, rotating in opposite directions.

For $Re > 40$ these vortices turn out to be unstable when exposed to small disturbances. The wake becomes unsteady as a result of a so-called Hopf bifurcation. The disturbances will make one vortex grow larger than the other, and eventually strong enough to draw the
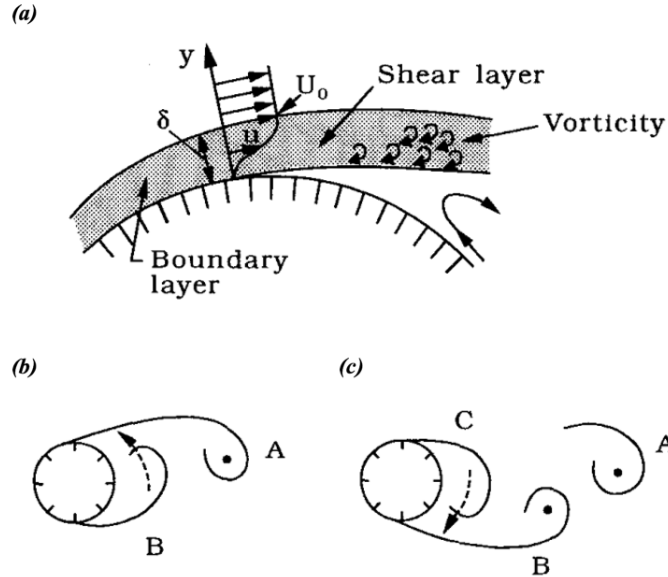
Figure 1.5: Mechanism of vortex shedding. (a) Shear layer; (b) prior to shedding of *Vortex A*; (c) prior to shedding of *Vortex B*. Reproduced from Sumer and Fredsøe (1997).

opposite vortex across the wake. This scenario is outlined by Sumer and Fredsøe (1997) and sketched in figure 1.5(b,c). The local pressure minimum caused by *Vortex A* pulls the opposing *Vortex B*. Thus, the oppositely rotating *Vortex B* will cut off further supply of vorticity from the boundary layer, and *Vortex A* will be shed. Figure 1.5(c) illustrates the instant when *Vortex A* has propagated a distance downstream as a free vortex, and *Vortex B* has grown strong enough to pull the new *Vortex C*. Consequently, *Vortex B* will be shed, in a similar fashion as *Vortex A*. The described process will continue, with alternately shed vortices, resulting in the characteristic Kármán vortex street.

1.1.3 Flow Around a Sphere

The flow around a sphere is relevant for a vast number of engineering applications, and therefore a significant amount of research has been conducted. In this section, the numerical findings by Johnson and Patel (1999); Tomboulides and Orszag (2000), as well as the experimental flow visualization and hot-wire measurements by Sakamoto and Haniu (1990), are used to present the flow features in the wake of a sphere. The different flow regimes appearing for varying Reynolds number are presented in figure 1.6. The left column contains schematic illustrations, whereas the right column presents experimental photos from the flow visualization by Sakamoto and Haniu (1990).

From early experiments Taneda (1956) found that the flow around a sphere starts to separate at $Re \approx 24$, generating a steady axisymmetric vortex ring, with a cross-section equal to the wake of a cylinder at $5 < Re < 40$. According to Johnson and Patel (1999) and Tomboulides and Orszag (2000), the steady and axial symmetric flow is maintained until a $Re \approx 210$ is reached. Although the axisymmetry is lost, the flow retains a planar symmetry. For the approximate Reynolds number range between 210 and 270, the wake consists of two
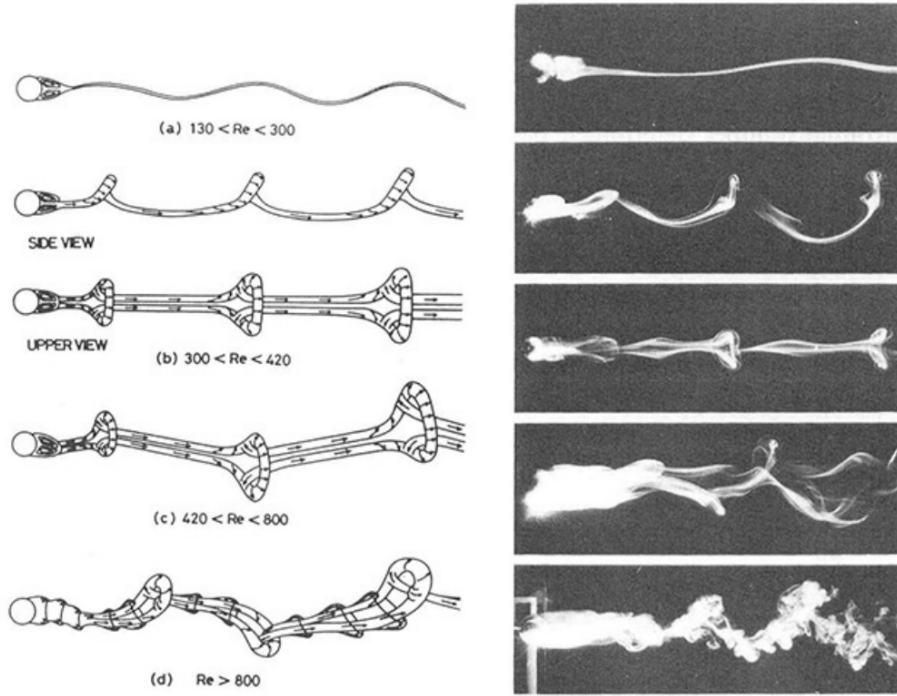
Figure 1.6: Flow structures in the wake of a sphere. (left images) Schematic illustrations; (right images) experimental photos (Sakamoto and Haniu, 1990).

counter-rotating streamwise vortices which extend far downstream of the sphere. The wake steadiness for the mentioned Re range deviates from the experimental results of Sakamoto and Haniu (1990). As depicted in figure 1.6(a), the authors observed an unsteady wavelike wake with a very long period for $130 < Re < 300$. However, all reviewed literature agrees on an unsteady periodic flow as Re reaches $270 < Re < 300$. From this Re onward the near-wake vortex ring starts to oscillate, and the wake turns into hairpin-shaped vortices, forming a ladder-like chain of overlapping loops. The characteristic hairpin vortices as well as the planar symmetry, are illustrated by the upper view, in figure 1.6(b). A fascinating property of the wake at this Re is the single-sided vortex shedding, which differs from the double-sided shedding seen for the circular cylinder in figure 1.3(c). For increasing Reynolds number, the planar symmetry and periodicity of the wake are lost at $Re \approx 420$, depicted in figure 1.6(c). The laminar vortices are shed until Re reaches about 800. When the Reynolds number is further increased, the hairpin-shaped vortices start to change from laminar to turbulent with an alternate orientation. This flow pattern continues to the upper critical Reynolds number $Re = 3.7 \times 10^5$ (Sakamoto and Haniu, 1990).

To provide a clear picture of the vortex structures, Tomboulides and Orszag (2000) computed isosurfaces of constant streamwise vorticity ω_x, in the wake of a sphere. The vorticity vector ($\vec{\omega} = \omega_x \vec{i} + \omega_y \vec{j} + \omega_z \vec{k}$) is mathematically defined as the curl of the velocity vector. As stated by Çengel and Cimbala (2008), a non-zero vorticity at one point in a flow field means that the particular flow particle is rotating. In Cartesian coordinates, the orientation and magnitude of the rotating motion are defined as:
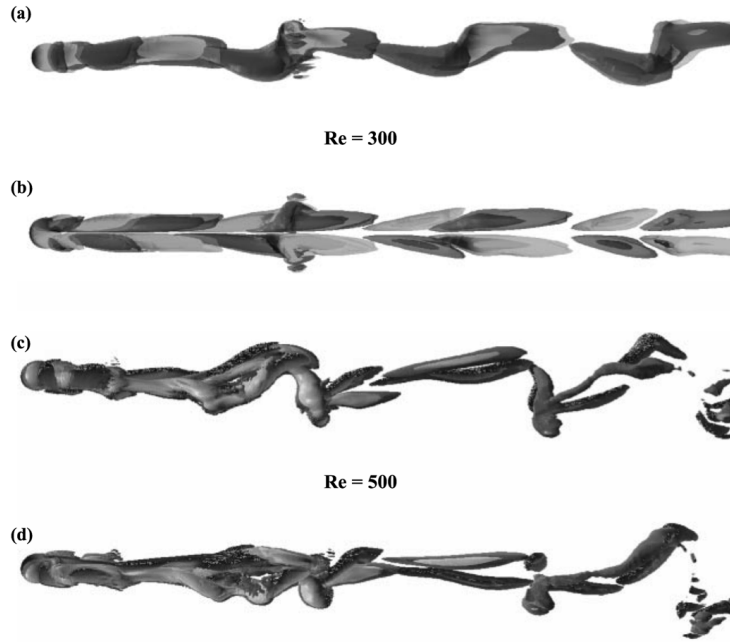
Figure 1.7: Isosurface plots of streamwise vorticity in the wake of a sphere at $Re = 300$ (a,b) and $Re = 500$ (c,d). (a,c) side view; (b,d) upper view. Reproduced from Tomboulides and Orszag (2000).

$$\vec{\omega} = \omega_x \vec{i} + \omega_y \vec{j} + \omega_z \vec{k} = \left(\frac{\partial w}{\partial y} - \frac{\partial v}{\partial z} \right) \vec{i} + \left(\frac{\partial u}{\partial z} - \frac{\partial w}{\partial x} \right) \vec{j} + \left(\frac{\partial v}{\partial x} - \frac{\partial u}{\partial y} \right) \vec{k} \qquad (1.3)$$

where u, v and w are the velocity components in x, y and $z-$direction, respectively.

Figures 1.7(a,b) present orthogonal views of the streamwise vorticity at $Re = 300$. Corresponding to the side view and upper view of figure 1.6(b). The dark and light gray denote positive and negative streamwise vorticity of the same magnitude. Hence, the shedding of single-sided vortices with a plane of symmetry at $Re = 300$, seems to be in agreement with the experimental results by Sakamoto and Haniu (1990). The vortex structures at $Re = 500$ in figures 1.7(c,d), suggest that the planar symmetry of the wake is lost, in accordance with the previously reported loss of symmetry at $Re \approx 420$ (Sakamoto and Haniu, 1990).

Figure 1.8 shows the resulting Strouhal number in the wake of a sphere for $300 < Re < 1.5 \times 10^4$. When $Re = 300$ is reached, a Strouhal number of approximately $St = 0.15$ - 0.165 is given by the shedding frequency of the hairpin-shaped vortices. This Strouhal number agrees well with the numerically obtained $St = 0.136$ and $St = 0.137$ of Tomboulides and Orszag (2000) and Johnson and Patel (1999), respectively. A single frequency dominates the wake until the Reynolds number reaches 800, and then the Strouhal number has increased to about 0.2. For a further increase in Re from 800 to 1.5×10^4, a second frequency is observed. Resulting in two Strouhal numbers, i.e., a low-frequency mode and a high-frequency mode. Sakamoto and Haniu (1990) suggests that the low mode St is caused by the wave motion of the wake due to the alternately shed vortices. This wave motion is easily observed in
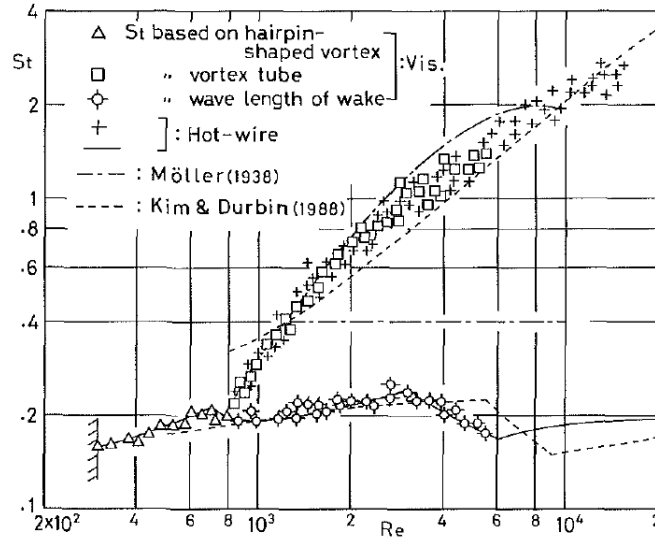
Figure 1.8: Dominant frequencies in the wake of a sphere (Sakamoto and Haniu, 1990).

the experimental photo of figure 1.6(d). The higher frequency mode St is hard to detect from the flow visualization. However, Sakamoto and Haniu (1990) states that, "The higher mode is caused by the periodic fluctuation in the vortex tube formed by the pulsation of the vortex sheet separated from the surface of the sphere". When the Reynolds number exceeds 1.5×10^4 the high-frequency mode is no longer present in the wake, and only the low-mode is observed. This was also found by Taneda (1978), who claimed that for Reynolds number above approximately $Re = 10^4$, a single constant Strouhal number exists, of about $St = 0.19$ - 0.20.

1.1.4 Flow Around a Prolate Spheroid

A prolate spheroid is an ellipse of revolution, thus, with a major and a minor axis. Dependent on its orientation, the prolate spheroid may be considered a slender or a bluff body. In this study, the orientation of interest has been when the major axis is perpendicular to the incoming flow. Hence, the spheroid is considered a bluff body. Following is a description of the wake formed behind a prolate spheroid with length to diameter ratio, $L_R = L/D = 6$, for Reynolds numbers up to 300. The numerical findings by El Khoury et al. (2012) are briefly compared with the experimental results of Kiya and Abe (1999) of the flow around an elliptical disk set normal to the undisturbed inflow.

For the particular aspect ratio, El Khoury et al. (2012) observed that the resulting flow features differ from the wake of a sphere. However, the endpoints of the major axis are close enough to affect the vortex shedding at the mid-span. For $Re = 50$ and $Re = 75$, the flow is separated, forming a steady vortex ring in the wake, similar to the near-wake of a sphere. Unlike the axisymmetry of the vortex ring behind a sphere for $Re < 210$, the symmetry is in this case broken by the elliptical cross-section, stretching the wake. When the Reynolds number exceeds 75, the wake turns unsteady, starting a periodic shedding of hairpin-shaped vortices, resulting in a ladder-like wake pattern. To illustrate the vortex structures in the
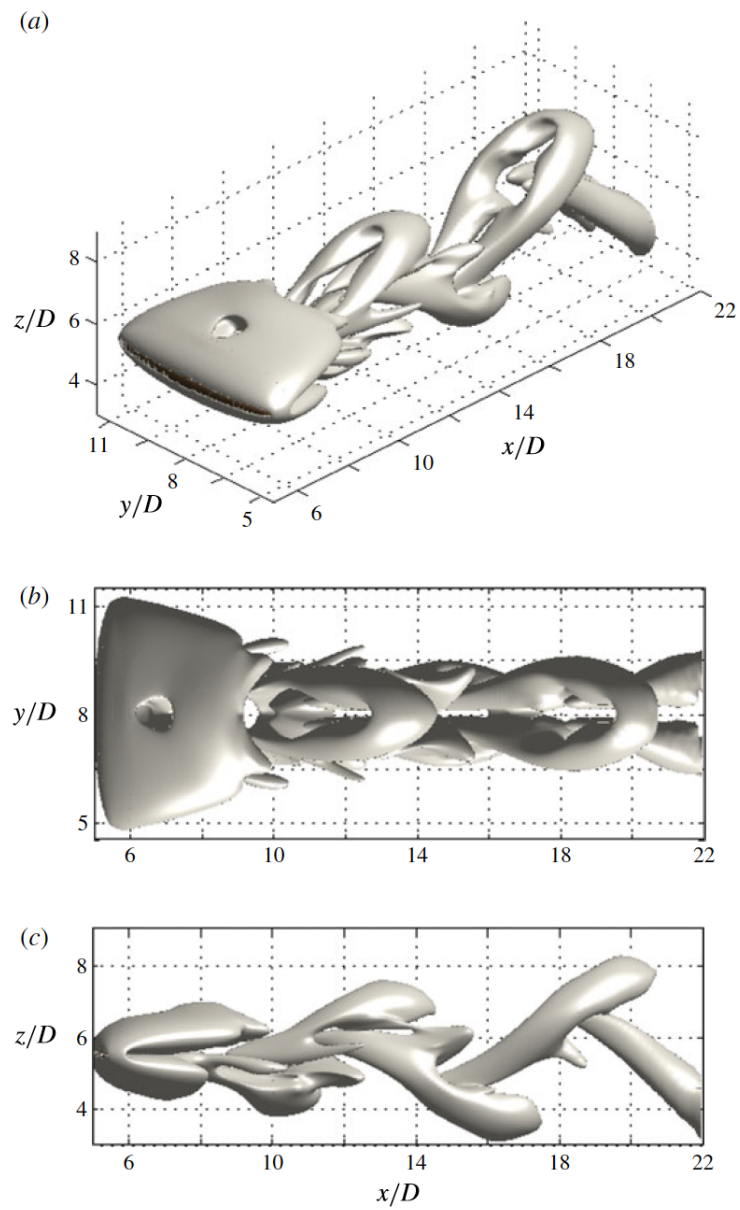
Figure 1.9: Instantaneous vortical structures in the wake of a $L_R = 6$ prolate spheroid at Re = 100. (a) perspective view; (b) top view; (c) side view (El Khoury et al., 2012).

wake, El Khoury et al. (2012) employed the λ_2-criterion, established by Jeong and Hussain (1995). Their method uses the role of the swirling motion in a vortex in generating local pressure minimum, as a starting point. To get information on local pressure extrema, Jeong and Hussain (1995) assessed the Hessian of the pressure, given by equation 1.4.

$$-\frac{1}{\rho}\left[\frac{\partial^2 p}{\partial x_i \partial x_j}\right] = \frac{DS_{ij}}{Dt} - \nu\frac{\partial^2 S_{ij}}{\partial x_k \partial x_k} + S_{ik}S_{kj} + \Omega_{ik}\Omega_{kj} \tag{1.4}$$

Here, the strain rate tensor S_{ij} and the vorticity tensor Ω_{ij} are expressed as follows:

$$S_{ij} = \frac{1}{2}\left(\frac{\partial u_i}{\partial x_j} + \frac{\partial u_j}{\partial x_i}\right), \quad \Omega_{ij} = \frac{1}{2}\left(\frac{\partial u_i}{\partial x_j} - \frac{\partial u_j}{\partial x_i}\right) \tag{1.5}$$

For the above equations, a Cartesian tensor notation is applied, with the indices i, j, k = 1, 2, 3. Hence, x_1, x_2, x_3, equal the x, y and $z-$direction, respectively. The components of the velocity vector are denoted u_1, u_2 and u_3.

To identify a vortex core, Jeong and Hussain (1995) neglects the first two terms on the right hand side of equation 1.4. The neglected terms represent unsteady straining and viscous effects that could contribute to a pressure minimum without the existence of a vortex core. Therefore, a local pressure minimum due to vortical motion is determined by examining $S_{ij}S_{ij}+\Omega_{ij}\Omega_{ij}$. Consequently, a vortex core is defined as a connected region with two negative eigenvalues of $S_{ij}S_{ij} + \Omega_{ij}\Omega_{ij}$ (Jeong and Hussain, 1995).

The result of the λ_2-method applied to the flow around a prolate spheroid at $Re = 100$ is shown in figure 1.9. In figures 1.9(a,b,c), the vortical structures in the wake of the spheroid are shown in perspective, upper and side view, respectively. The three different views clearly indicate the shape and orientation of the alternately shed hairpin vortices. The numerical results are comparable to the flow visualization experiments by Kiya and Abe (1999) in figure 1.11. Kiya and Abe (1999) studied the wake of two elliptic disks set normal to the inflow, whose major diameter is 2 or 3 minor diameters. Flow visualization was made in a water tunnel, by injecting fluorescent dye under UV illumination, upstream of the disk with the highest aspect ratio $L_R = 3$ for $Re = 200$. Despite the aspect ratio and Reynolds number differences, the results of the prolate spheroid at $Re = 100$, and the elliptical disk at $Re = 200$ are seen to resemble one another. The characteristic hairpin-shaped vortices are well illustrated in figure 1.9(a), and the two bottom images of figure 1.11(a). Additionally, the visualization of the wake in the minor plane, shown in figure 1.9(c) and 1.11(b), reveal a quickly increasing width of the vortices when propagating downstream, compared with the growth of the wake in the major plane. This leads to the axis switching phenomenon, suggested by El Khoury et al. (2012) in figure 1.10. By plotting slices of the streamwise velocity u/U_0, at three different downstream positions, El Khoury et al. (2012) found that the switching seems to take place about $10D$ downstream of the $L_R = 6$ prolate spheroid. A similar axis switching was found by Kiya and Abe (1999) for the elliptic disk, occurring approximately $4D$ downstream.

The wake of the $L_R = 6$ prolate spheroid becomes unsteady at a Reynolds number which lies between the case of a circular cylinder ($Re = 40$) and a sphere ($Re \approx 300$), specified in sections 1.1.2 and 1.1.3. Additionally, the vortex shedding shown in figure 1.9 is double-
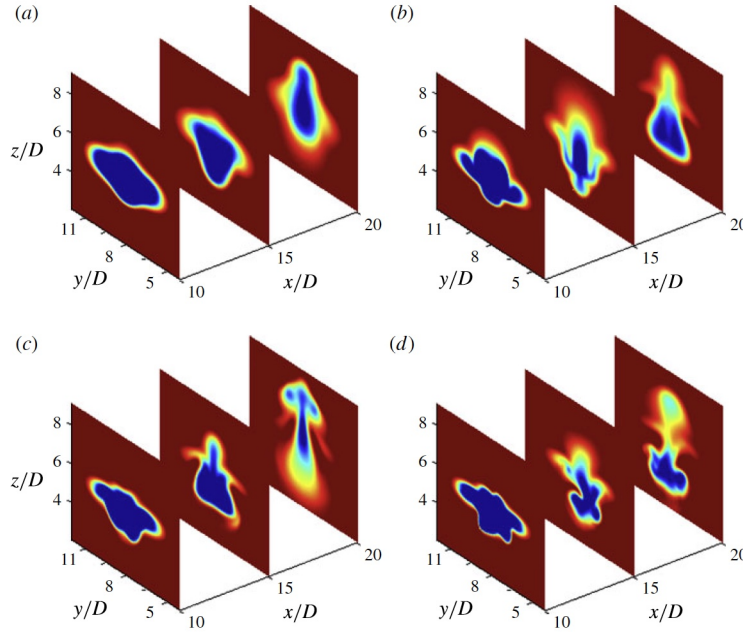
Figure 1.10: Slices in the cross-stream direction showing instantaneous streamwise velocity u/U_0. The colours vary from 0.7 (dark blue) to 1 (dark red). (a) $Re = 100$; (b) $Re = 150$; (c) $Re = 200$; (d) $Re = 300$ (El Khoury et al., 2012).

sided, which deviates from the single-sided shedding behind a sphere, presented by Sakamoto and Haniu (1990). For a further increase of Reynolds number up to $Re = 300$, the vortical structures gradually become more irregular. Along with the dominating hairpin-shaped vortices, El Khoury et al. (2012) detected smaller randomly shaped vortex structures. The corresponding wake frequencies from the shedding were found by assessing the time evolution of the transverse velocity components in the wake. The resulting Strouhal number increases from $St = 0.109$ to $St = 0.151$ as the Reynolds number is increased from $Re = 100$ to 300. By comparing Strouhal numbers at $Re = 300$, the $L_R = 6$ prolate spheroid has a significantly lower St than a circular cylinder of $St \approx 0.2$. Whereas compared with a sphere, the St by El Khoury et al. (2012) is slightly greater than the numerically obtained Strouhal number of $St = 0.136$ - 0.137, presented in section 1.1.3. El Khoury et al. (2012) concludes that the wake behind the $L_R = 6$ prolate spheroid, shares flow features with the wake of both a cylinder and a sphere.
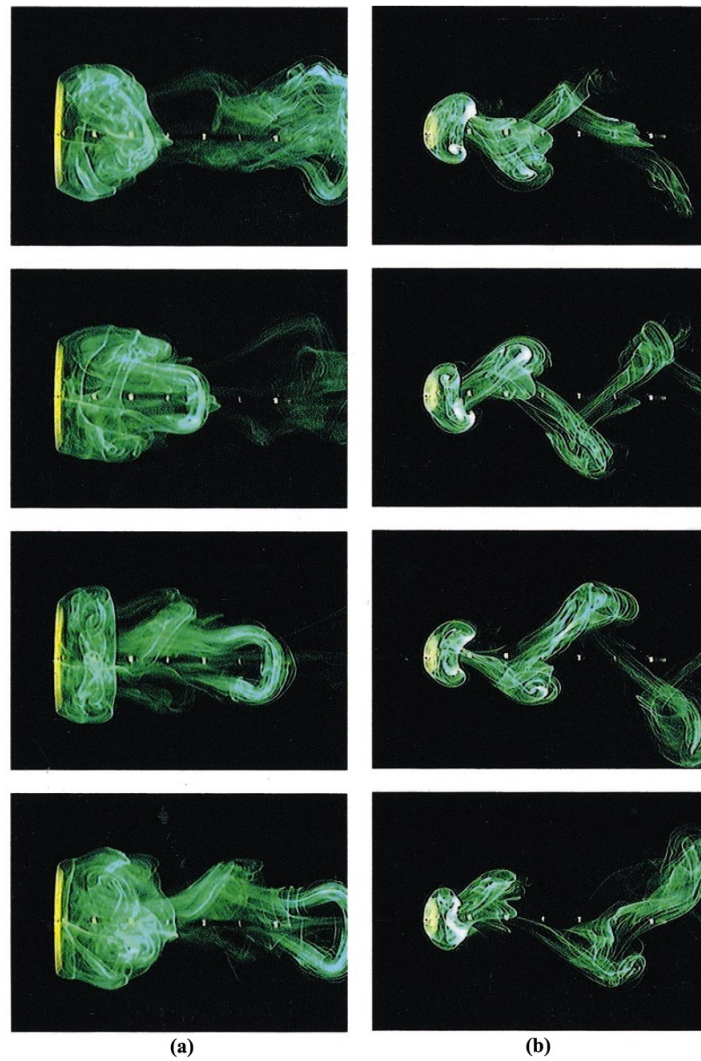
Figure 1.11: Flow visualization results for a $L_R = 3$ elliptical disk at $Re = 200$. (a) major plane; (b) minor plane (Kiya and Abe, 1999).

1.2   Scope of the Present Study

The aim of the present study is to simulate the flow around a prolate spheroid in cross-flow by utilizing the Computational Fluid Dynamics (CFD) software, OpenFOAM. The prolate spheroid of interest has an aspect ratio $L_R = 4/3$. The motivation for this particular shape and dimension is the enclosed fish farm concept, "The Egg", newly invented by Hauge Aqua. Fully enclosed fish farms are one of the possible solutions to cope with the salmon louse problem, to ensure a sustainable growth of the marine aquaculture in Norway. The simplified numerical model, with the appendices of the real model removed, is depicted in the right image of figure 1.1. The model is assumed fully submerged in an infinite fluid. Since it exists no previous literature for this particular geometric shape, the present study is limited to low Reynolds number flow, up to $Re = 500$.

Based on the background theory presented in section 1.1, it is shown that the flow features appearing in the wake of a prolate spheroid with aspect ratio $L_R = 6$, resemble the flow phenomena seen for both cylinder and a sphere. Therefore, it is of interest to investigate the flow as the aspect ratio is lowered, and the spheroid approaches the form of a sphere.

First, a grid dependency study is to be performed, for $Re = 300$. This particular Reynolds number was chosen since it is included in the reviewed literature for both the cylinder, sphere and prolate spheroid. The numerical properties of importance are considered to be the grid cell size, cell geometry, domain size and the time step. For every part of the dependency study, flow parameters as lift and drag coefficient, pressure and shedding frequency, are used to assess convergence. Velocity profiles close to the spheroid surface, as well as pressure and velocity changes close to the domain boundaries, are sampled to evaluate the cell and domain size, respectively.

For the adequate grid, suitable post-processing techniques are used to answer the following research question:

To what degree does the flow around a low aspect ratio ($L_R = 4/3$) prolate spheroid resemble the flow features appearing in the wake of a sphere?

To answer the question properly, the present results are compared to similarly shaped bluff bodies, including a sphere, $L_R = 6$ prolate spheroid and a cylinder. The flow will mainly be assessed by the following features:

- Wake topology

- Wake fluctuations

- Resulting hydrodynamic loads

The results of the present study might reveal some of the challenges related to closed containment fish cages. Contrary to the traditional open net cage, the closed walls will force the water to flow around the cage. The resulting hydrodynamic forces and motions may cause limitations and requirements that are not included in today's technical standards. Also, the study is supposed to generate a flow study of high quality for a prolate spheroid of low aspect ratio.

1.3 Structure of the Present Thesis

The present thesis is divided into six different chapters. Following is a brief description of each part of the report.

Chapter 1 presents an overview of the flow features appearing in the wake of cylinders, spheres and prolate spheroids. Both numerical and experimental findings from various authors are presented to give a reliable presentation. Based on the background theory, the goal of the present study is outlined.

Chapter 2 sums up the reviewed literature, categorized by the shape of the studied bluff body.

Chapter 3 presents the governing differential equations for the particular flow situation. Additionally, aspects of the applied numerical method are described.

Chapter 4 outlines the performed numerical work, including important features of pre- and post-processing.

Chapter 5 presents the results from the simulation of flow around the $L_R = 4/3$ prolate spheroid. The results are discussed and compared with previous findings in the literature.

Chapter 6 summarizes and concludes the findings. Ultimately, a proposal for further work is given.

Chapter 2

Literature Review

The literature review contains a study of the flow around bluff bodies, with and without an aspect ratio. It will mainly investigate the flow around circular cylinders, spheres and prolate spheroids. The purpose of the literature study is to get an overview and understanding of flow phenomena arising in the wake of bluff bodies in a steady flow. This knowledge is crucial for being able to perform high-quality CFD simulations.

Relevant literature has been found using Google Scholar and Oria. The latter, being a literature search engine provided by the library of NTNU. Professor Bjørnar Pettersen has also been helpful with suggesting useful articles. Printed books and doctoral theses are borrowed from the collection at the Marine Technology Library.

The present chapter provides a brief introduction to the reviewed literature, categorized by the shape of the studied bluff body. Mainly introducing the scope, method and relevant discoveries of each study. If possible, the accuracy and reliability of the findings are assessed.

2.1 Flow Around a Circular Cylinder

An introductory literature study is performed for a circular cylinder of both infinite and finite length. The main sources of information regarding infinite cylinders are the two textbooks by Sumer and Fredsøe (1997) and Zdravkovich (1997). A summary of their findings is presented in section 1.1.2. Additionally, the article by Qu et al. (2013) is studied to obtain numerical and more recent data. Finite cylinders of varying length are investigated in the numerical work by Sheard et al. (2004).

2.1.1 Infinite Cylinder

Sumer and Fredsøe (1997) describe the flow pattern and resulting loads when cylindrical structures are exposed to current and waves. The literature study is limited to the first two chapters of the book, presenting the flow around an infinite cylinder in steady current and the resulting hydrodynamic forces. The first chapter gives a brief introduction of the flow regimes, from creeping flow ($Re < 5$) up to complete turbulent flow for transcritical Reynolds numbers. Extra attention was given to the flow regime at $40 < Re < 200$, leading to a laminar vortex street in the wake of the cylinder. Both the mechanism and frequency of the vortex shedding, are described. The second chapter addresses the resultant forces exerted
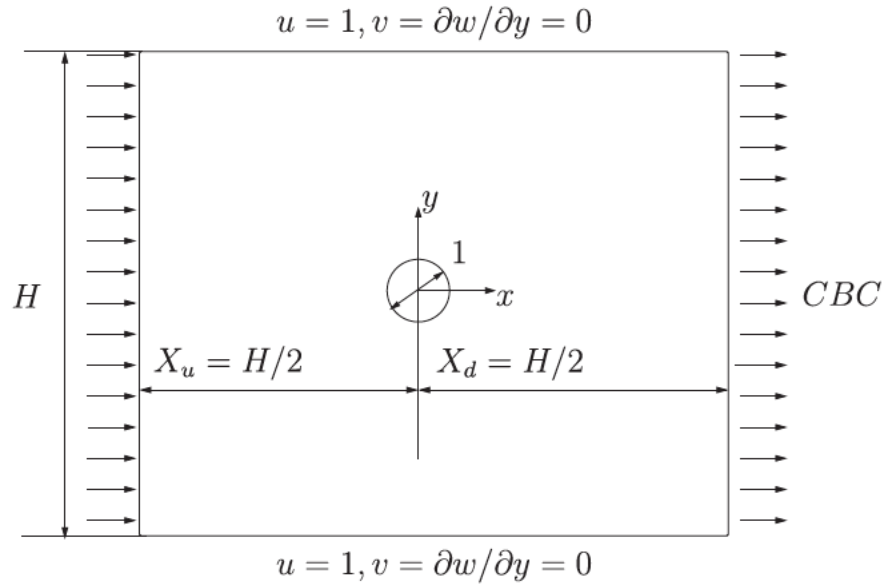
Figure 2.1: The computational domain employed to model the flow past a cylinder (Qu et al., 2013).

by the flow around the cylinder, presenting the details of the oscillatory lift and drag force as a consequence of vortex shedding.

The extensive study of the flow around circular cylinders by Zdravkovich (1997) is included to support the findings of Sumer and Fredsøe (1997). The literature study is limited to the first three chapters of the book, including a conceptual overview, and a description of the steady and unsteady, laminar flow regimes. Hence, covering similar topics, like those studied in Sumer and Fredsøe (1997). Even though the references to both textbooks are considered to be old, the presented data are of high quality and still being used to validate recent numerical methods.

The numerical study by Qu et al. (2013) investigates the flow past a stationary cylinder at Reynolds numbers in the range $50 \leq Re \leq 200$. Employing a second order accurate fractional step method by a finite volume code. The authors applied a square domain, with H defining the domain size, as shown in figure 2.1. The inflow boundary was set to a constant streamwise velocity $u = 1$, whereas a convective boundary condition was assigned at the outlet. The sides of the domain were given free stream conditions, specified in figure 2.1. At $Re = 100$, a sensitivity study was performed, concerning grid refinement, domain size and time step. By comparing global time-averaged results with previous findings, a grid consisting of 386 circumferential cells, was found sufficient. The required domain size and time step for obtaining grid independent results, were $H = 120D$ and $\Delta t = 0.01 \ s$. Final results by Qu et al. (2013), regarding force coefficients and separation angle, are compared with the present results in section 5.2.
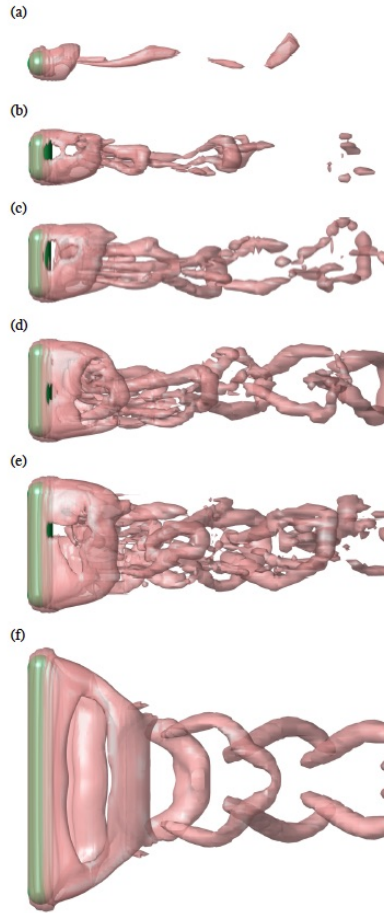
Figure 2.2: Isosurface plots of the vortical structures in wakes of cylinders with free hemi-spherical ends. At $Re = 300$ for: (a) $L_R = 1$; (b) $L_R = 2$; (c) $L_R = 3$; (d) $L_R = 4$; (e) $L_R = 5$; and at $Re = 100$ for: (f) $L_R = 10$ (Sheard et al., 2004).

2.1.2   Finite Cylinder

In the article by Sheard et al. (2004), the flow around a cylinder with free hemispherical ends for length ratios up to $L_R = L/D = 10$, is studied numerically. Hence, for the $L_R = 1$ case, the flow around a sphere is obtained. For $L_R > 1$, the flow direction is set normal to the symmetry axis of the cylinder. A spherical domain, extending $30D$ from the sphere, was used for all simulations. Applying a spectral element scheme, using a Fourier expansion of the velocity and pressure fields. Details about the numerical method may be found in Sheard et al. (2004). To confirm the accuracy of the results, mean drag coefficients up to $Re = 300$, were compared with previous data. The authors state that their errors are within 0.5%, throughout the Reynolds number range.

One of the primary aims of the study was to determine how the hairpin-shaped vortices in the flow past a sphere relate to the Kármán vortex street behind an infinite cylinder. In figure 2.2, are isosurface plots of the vortical structures, visualized by the λ_2-definition. Figures 2.2(a-e) depict the wake flow at $Re = 300$ for $1 \leq L_R \leq 5$, whereas figure 2.2(f)

shows the result for $L_R = 10$ at $Re = 100$. It may be seen that for the smaller L_R, the wakes are not symmetric about the mid-span of the cylinder. For length ratios up to $L_R = 4$, Sheard et al. (2004) found a decreasing Strouhal number for the spanwise component of the force, acting on the cylinder. Also, the magnitude of the spanwise force itself is decreased, in contrast to an increasing force magnitude in the transverse direction. At the onset of symmetry, for L_R between 5 and 10, the development of Kármán-like shedding in the near-wake region of the cylinder mid-span is observed in figure 2.2(f). The author highlights the interesting observation that even at a length ratio $L_R = 10$, the influence of the free ends on the two-dimensional vortex street, is significant.

The article by Sheard et al. (2004) is considered to be relevant for the present work since it compares the flow around a cylinder at different low aspect ratios, including $L_R = 1$ and 2.

2.2 Flow Around a Sphere

The basis for the study of three-dimensional flow around a sphere, is a number of scientific articles, presenting both numerical and experimental results. A brief summary of the flow features submitted by the different authors is given in section 1.1.3.

The article by Johnson and Patel (1999) provides an in-depth analysis of the flow past a sphere for Reynolds number up to 300. The Reynolds number range covers the first three flow regimes of the flow past a sphere, including steady axisymmetric flow, steady non-axisymmetric flow, and unsteady periodic flow. The goal of the work was to give a description of the flow around a sphere, from symmetry breaking to unsteadiness. Flow visualization experiments were performed to validate the numerical results.

The numerical simulations were computed on a spherical grid, extended $15D$ from the sphere center. At least ten grid points were placed within the boundary layer, with a minimum grid spacing of 0.005, adjacent to the sphere. The boundary layer thickness, δ/D, was assumed equal to $1.13/\sqrt{Re}$, according to theory by Schlichting (1979). A four-stage Runge-Kutta method was used to numerically solve the Navier-Stokes equation, while a pressure Poisson equation was formulated to satisfy the continuity equation. For details on the numerical method, reference is given to Johnson and Patel (1999).

Figure 2.3 shows the resulting wake structure from dye injection experiments at $Re = 300$, by using food coloring diluted in water as the dye. The pictures of figure 2.3(b,c) are captured, approximately $30D$ downstream of the sphere, whereas figure 2.3(a) depicts the near-wake region. The (x,y) and (x,z)-plane of the figure correspond to the side view and upper view of figure 1.6(b) in section 1.1.3. The results clearly reveal the unsteady periodic shedding of hairpin-shaped vortices. The regularity in orientation and vortex spacing is evident.

Johnson and Patel (1999) report that their results are in good agreement with previous experimental and numerical findings. Therefore, the article has been considered to provide useful knowledge of the flow around a sphere. The fact that they performed both numerical and experimental work strengthens the reliability of their findings.

By Sakamoto and Haniu (1990), a study on the vortex shedding from spheres in uniform flow was carried out by experimentally investigating the wake at Reynolds number in the
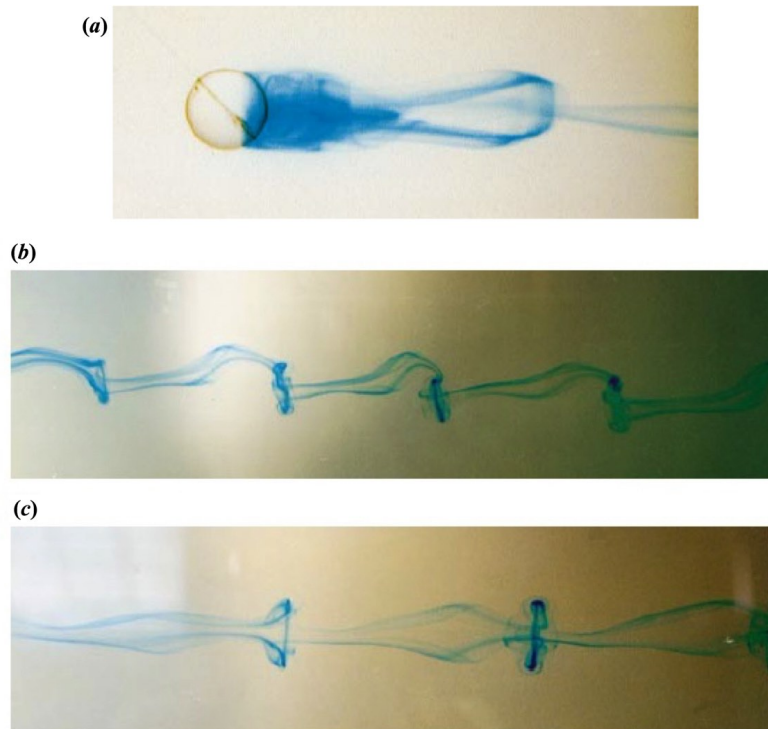
Figure 2.3: Dye visualization of hairpin-shaped vortices in the wake of a sphere at $Re = 300$. (a) (x,z)-plane of the near-wake; (b) (x,y)-plane; (c) (x,z)-plane. Reproduced from Johnson and Patel (1999).

range 300 to 4×10^4. Thus, starting at the highest tested Re by Johnson and Patel (1999), and covering the transition into an entirely turbulent vortex street as the Reynolds number exceeds 6×10^3. The vortex shedding frequency was obtained by hot-wire measurements in a wind tunnel, whereas the flow was visualized by injecting uranine dye in a water channel. The authors tested the accuracy of their hot-wire measurements by investigating the induced velocities of vortex shedding from circular cylinders. The uncertainty in the measured velocities was found to be less than ± 2 percent.

The article by Sakamoto and Haniu (1990) provided a good understanding of the flow structures appearing in the wake of a sphere and their associated frequencies. Additionally, the experimental flow visualizations have been useful to validate the numerical findings of the flow around a sphere.

In the article by Tomboulides and Orszag (2000), the flow around a sphere is simulated numerically for Reynolds numbers from 25 to 1000. The main goal was to identify the transitional regimes as the Reynolds number is increased, along with the physical mechanisms. The flow was investigated by using a direct numerical simulation (DNS) based on a mixed spectral element/Fourier spectral method. The simulations were carried out in a cylindrical domain, which extended $4.5D$ in the upstream and radial directions, from the sphere center. This particular extent was selected by considering the rate of decay of the disturbances away from the sphere, by potential theory. A decay rate of $1/r^3$, with r being the radial distance, was employed. Therefore, at $4.5D$ from the sphere center, the velocity differs only 0.1%

from the undisturbed velocity. Downstream of the sphere center, the domain extends $25D$ to ensure that it fits at least 3 to 4 vortical structures in the wake region.

Tomboulides and Orszag (2000) claim that their results are in good agreement with numerical and experimental findings of other authors, e.g. compared with the simulations by Johnson and Patel (1999) for $Re \leq 300$. The compared flow parameters are wake length, separation angle and drag coefficient.
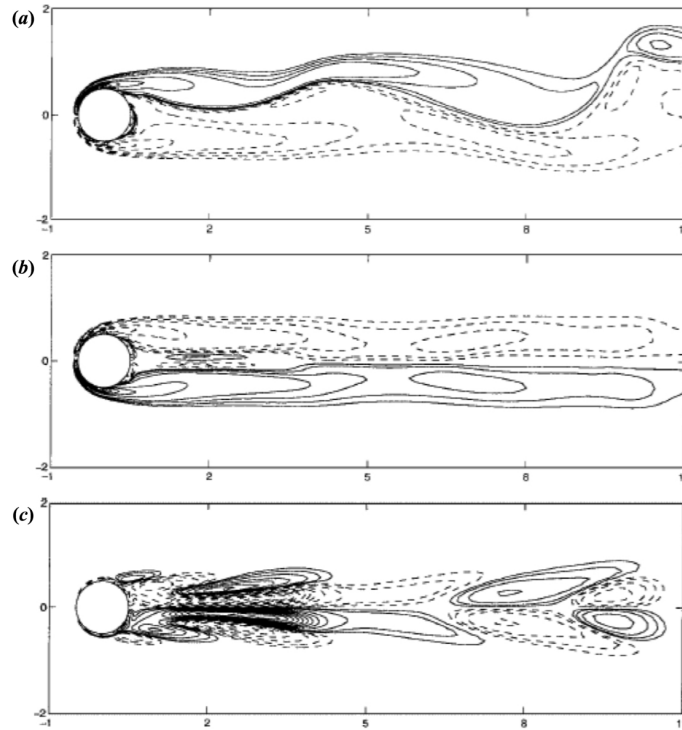

Figure 2.4: Instantaneous contours of vorticity in the wake of a sphere at $Re = 300$. (a) ω_x in the (x,y)-plane; (b) ω_y in the (x,z)-plane; (c) ω_z in the (x,z)-plane (Ploumhans et al., 2002).

The numerical study by Ploumhans et al. (2002) investigates the flow around a sphere at $Re = 300$, 500 and 1000, expecting each Reynolds number to correspond to different flow behavior. Direct numerical simulations were performed by a fast parallelized vortex method on a non-uniform grid. The method was validated by comparing the results at $Re = 300$ with previous findings from Tomboulides and Orszag (2000) and Johnson and Patel (1999). Computed mean values of the lift and drag coefficient, as well as the Strouhal number, showed a high level of concurrence with compared data. Contours of ω_x, ω_y and ω_z in the near wake at $Re = 300$, are plotted in figure 2.4. Figures 2.4(b,c) clearly reveal the symmetry of the flow in the (x,z)-plane. Contrary to the asymmetric flow in the middle (x,y)-plane of figure 2.4(a). The periodic flow regime was unveiled by plotting contours of the streamwise vorticity, ω_x, at five successive instants for every quarter shedding period. Thus, the first and last picture were identical and equal to figure 2.4(a).
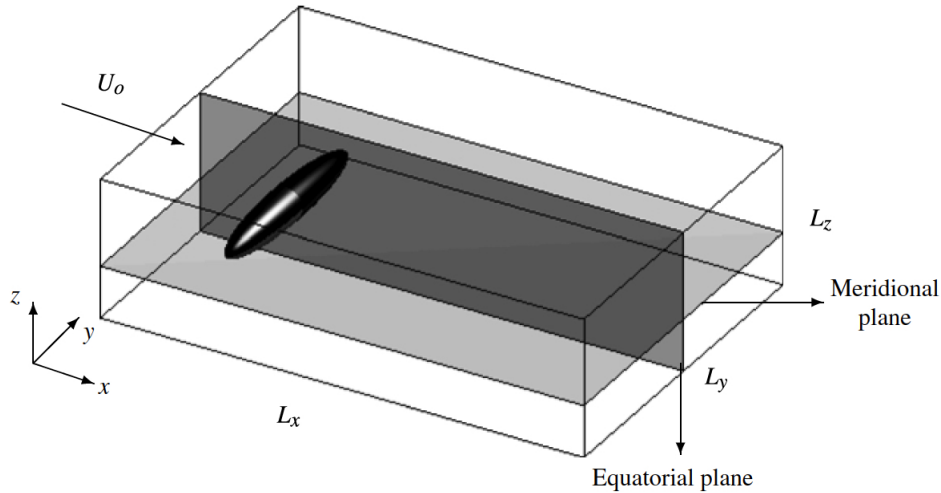
Figure 2.5: Overview of the computational domain and coordinate system used by El Khoury et al. (2012).

2.3 Flow Around Low Aspect Ratio Bluff Bodies

For the last part of the literature review, the flow around three-dimensional asymmetric bluff bodies has been considered. Limited to bodies with relatively low aspect ratio, and its principal axis oriented perpendicular to the inflow. The particular aspect ratios included are $L_R = 6$, investigated for a prolate spheroid, $L_R = 3$ and 2, for an elliptic disk, and $L_R = 1.6$, 1.3 and 1.04, for a cylinder with free hemispherical ends.

2.3.1 Aspect Ratio = 6

The numerical work by El Khoury et al. (2012), investigates the flow around a $L_R = 6$ prolate spheroid at seven different Reynolds numbers, $Re = 50$, 75, 100, 150, 200, 250 and 300. The author provides a detailed analysis of the flow computed by the DNS solver MGLET. According to El Khoury et al. (2012) MGLET uses a finite volume method, which discretizes the Navier-Stokes equation on a staggered Cartesian mesh. An explicit third order Runge-Kutta scheme was utilized for the time integration. The applied computational domain shown in figure 2.5, extends $L_x = 22D$, $L_y = 16D$ and $L_z = 11D$ in the streamwise, spanwise and transverse direction, respectively. Resulting in a minimum distance of $5D$ between the surface of the spheroid and the domain borders. The minimum cell sizes of the non-equidistant grid, are located closest to the spheroid surface, with $\Delta x = \Delta z = 0.025D$. In the spanwise direction the smallest grid spacing is found at each pole, and equal to $\Delta y = 0.0095D$. Each simulation was computed with a constant time step of $\Delta t = 0.002D/U_0$ until $t = 400D/U_0$ was reached.

The results from the numerical study are presented in section 1.1.4, and compared with the experimental findings by Kiya and Abe (1999). The computational setup by El Khoury et al. (2012) has served as the basis for the present work, because of the similarities in both geometric shape and Reynolds number range.
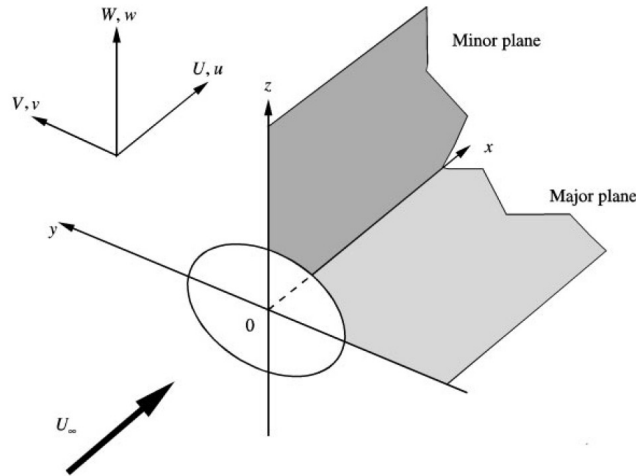
Figure 2.6: Experimental setup to investigate the flow around elliptical disks (Kiya and Abe, 1999).

2.3.2 Aspect Ratio = 2 and 3

Kiya and Abe (1999) present the experimental results of the flow around elliptical disks with aspect ratio $L_R = 2$ and 3. Both high Re wind tunnel experiments and low Re water channel experiments were carried out. The objective was to investigate the wake behind the disk oriented with its major axis normal to the incoming flow. Therefore, the shape of the projected area of the elliptical disk and prolate spheroid studied in El Khoury et al. (2012) is equal. The experimental setup is depicted in figure 2.6. According to the figure, the (x,y)-plane is referred to as the major plane, whereas the (x,z)-plane is the minor.

The flow visualization experiments at low Reynolds number, $Re = 200$, were considered to be useful for validation of the numerically computed flow structures by El Khoury et al. (2012). The results of the visualization experiment are described in section 1.1.4, and depicted in figure 1.11. Two periodic components of velocity fluctuations were found, one in the minor, and one in the major plane. The fluctuations in the minor plane correspond to the alternate shedding of hairpin-shaped vortices, similar to the wake of a $L_R = 6$ prolate spheroid, at $Re = 100$. A meandering motion in the major plane was found to be the reason for the second wake frequency. The most striking discoveries relating the $L_R = 6$ prolate spheroid and the elliptical disks are the hairpin-shaped and double-sided vortices and the observed axis switching phenomenon in the wake.

2.3.3 Aspect Ratio = 1.3 and 1.6

In the article by Schouveiler and Provansal (2001), the periodic wake behind finite-length cylinders with free hemispherical ends is studied experimentally. A total of nine different aspect ratios from $L/D = 1$ to 5, were tested. However, $L/D = 1.3$ and 1.6 are of highest interest since they are closely related to the aspect ratio of the prolate spheroid considered in the present work. The main focus of the study was to detect the transition from stationary
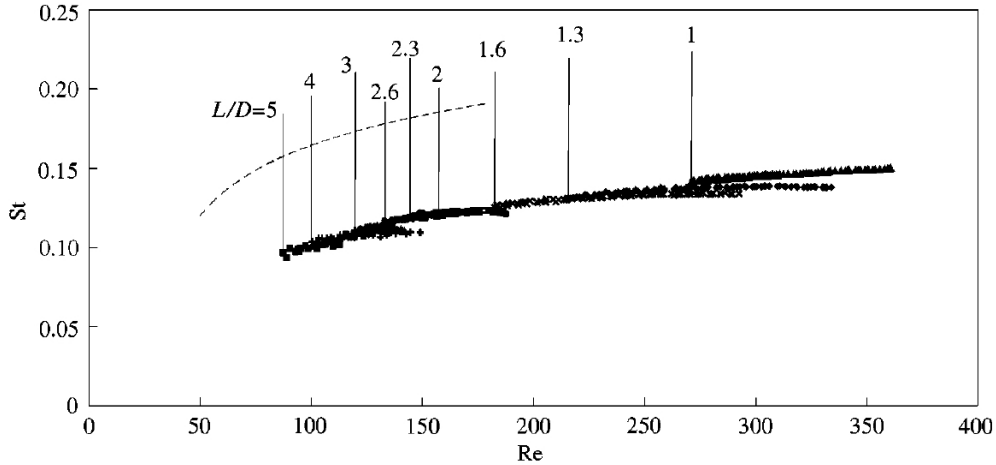
Figure 2.7: Strouhal number as function of Re for varying aspect ratio. The vertical lines define the critical Reynolds number Re_c at each aspect ratio (Schouveiler and Provansal, 2001).

flow to the time-dependent periodic flow, in the Reynolds number range from 50 to 400. For Reynolds numbers above the first critical value, the authors observed a single dominant frequency by spectral analysis of the measured streamwise velocities. To measure the wake velocities, a laser Doppler anemometer was used. A detailed description of the experimental setup is given in Schouveiler and Provansal (2001). Resulting Strouhal numbers for the single-frequency domain, are shown in figure 2.7. The figure suggests a decreasing trend of the critical Reynolds number as the aspect ratio is increased. For $L_R = 1.3$ and 1.6 the flow is seen to turn unsteady at $Re \approx 210$ - 220 and $Re \approx 170$ - 180, respectively.

2.3.4 Aspect Ratio = 1.04

The work outlined by Sheard et al. (2008) studies the flow normal to a short cylinder with hemispherical ends, employing a spectral-element/Fourier method. The numerical method is closely related to the algorithm used by Tomboulides and Orszag (2000) and the previous work by the same authors in Sheard et al. (2004). An accuracy better than 1% was found for the case of a sphere at $Re = 300$ when comparing averaged drag and Strouhal number with previous data. Different length ratios, $L_R \leq 5$, were employed. A very short cylinder, $L_R = 1.04$, was examined to investigate the relationship between azimuthal asymmetry of a nearly spherical body and the resulting wake symmetries. The resulting vortical structures visualised by the λ_2-definition are shown in figure 2.8 at $Re = 250$ and 300. At $Re = 250$, a steady non-axisymmetric wake consisting of a pair of counter-rotating vortices is found, according to figures 2.8(a,b). The planar symmetry evident in figure 2.8(a), is closely related to the flow around a sphere at corresponding Re. As the Reynolds number is increased to $Re = 300$, the wake turns unsteady, and the familiar hairpin-shaped vortices appear. However, for the asymmetric body, a preferred orientation of the wake aligned with the minor axis, is eventually apparent. Whereas, for the axisymmetric spherical body, there is no preference to the wake orientation. By studying the transverse force components, Sheard et al. (2008)
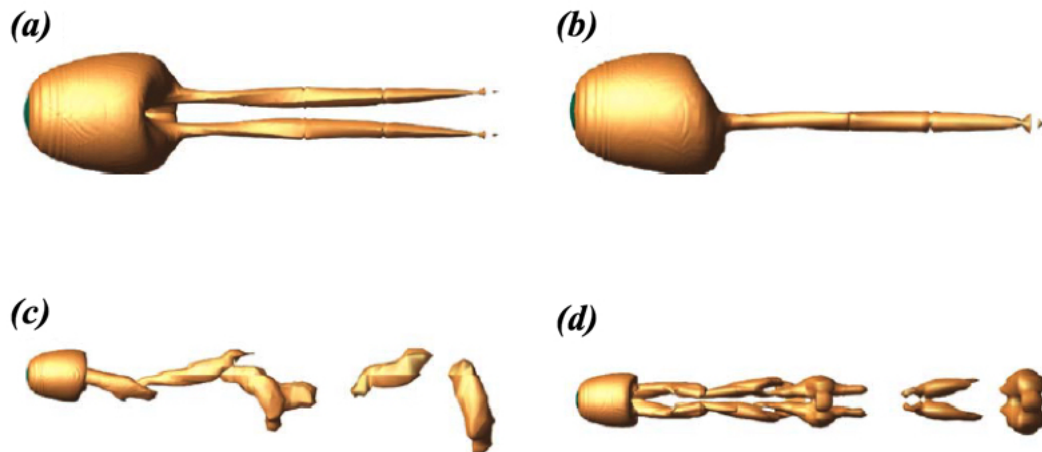
Figure 2.8: Vortical structures in the wake of a $L_R = 1.04$ cylinder. $Re = 250$ for the upper figures, and 300 for the lower. (a) top view; (b) side view; (c) initial orientation to emerge from the steady-state solution at $Re = 250$; (d) preferred orientation after 130 shedding periods (Sheard et al., 2008).

found a loss of planar symmetry as the Reynolds number reaches $Re = 350$ - 360, by the evolution of a non-zero and fluctuating side force.

The article by Sheard et al. (2008) is of relevance for the present study since it investigates the flow changes as the sphere is slightly elongated along what becomes the major axis. Hence, the value to compare the results as the aspect ratio is further increased in the present study.

Chapter 3

Governing Equations and Numerical Aspects

This chapter presents the partial differential equations (PDEs) of fluid flow and explains briefly how they are solved, numerically, in CFD. The software OpenFOAM utilizes a finite volume discretization. According to Greenshields (2015a), the discretization of a problem, means dividing it into discrete quantities, and for the finite volume method, the problem is discretized as follows:

Spatial discretization. Defining a computational domain, and dividing it into several small control volumes, called cells. Each cell in a three-dimensional domain is a volume.

Temporal discretization. For a flow that changes with time (transient problem), the time domain has to be divided into a finite number of time steps.

Equation discretization. By linearizing the governing PDEs, a system of algebraic equations is generated in terms of discrete quantities defined at each cell in the domain.

The discretized problem is subsequently solved, iteratively, by a numerical solver algorithm. The algorithm iterates, until a user-specified residual is reached. It exists a vast number of numerical solvers, and to explain all, is out of the scope of this thesis. However, the algorithm used in this work, along with the governing equations and finite volume method, will be described in the following sections.

3.1 Governing Equations

The fluid flow considered throughout the present study is considered to be unsteady laminar flow, of a viscous, incompressible, Newtonian fluid without free-surface effects. In this case the governing equations of motion are the continuity equation and the Navier-Stokes equation, given by equation 3.1 and 3.2, in accordance with Çengel and Cimbala (2008).

$$\vec{\nabla} \cdot \vec{V} = 0 \tag{3.1}$$

$$\frac{\partial \vec{V}}{\partial t} + (\vec{V} \cdot \vec{\nabla})\vec{V} = -\frac{1}{\rho}\vec{\nabla}p + \nu\nabla^2\vec{V} \tag{3.2}$$

The continuity equation is derived from the conservation of mass, while the Navier-Stokes equation represents transport of momentum through the computational domain. The continuity equation is a scalar equation, whereas the Navier-Stokes equation is presented on vector form. Thus, for three-dimensional flow in Cartesian coordinates, there are four equations and four unknowns u, v, w and p (Çengel and Cimbala, 2008). Where p is the modified pressure as a result of eliminating the gravity term from the Navier-Stokes equation. This is possible since the free-surface effect is neglected. The governing equations can be written in tonsorial form, as:

$$\frac{\partial u_i}{\partial x_i} = 0 \tag{3.3}$$

$$\frac{\partial u_i}{\partial t} + u_j\frac{\partial u_i}{\partial x_j} = -\frac{1}{\rho}\frac{\partial p}{\partial x_i} + \nu\frac{\partial^2 u_i}{\partial x_i \partial x_j} \tag{3.4}$$

here, $i = 1,2$ and 3 representing the three Cartesian directions x, y and z, and u_i stands for the velocity in these directions. The density of the fluid is denoted ρ, and ν is its kinematic viscosity. The Navier-Stokes equation may also be written:

$$\frac{\partial u_i}{\partial t} + u_j\frac{\partial u_i}{\partial x_j} = \frac{1}{\rho}\frac{\partial \sigma_{ij}}{\partial x_j} \tag{3.5}$$

where, $\sigma_{ij} = -p\delta_{ij} + 2\mu S_{ij}$, is called the stress tensor. The δ_{ij} is called the Kronecker delta function, and has the property of being equal to unity when $i = j$, and zero otherwise. The rate of strain tensor is given as $S_{ij} = \frac{1}{2}\left(\frac{\partial u_i}{\partial x_j} + \frac{\partial u_j}{\partial x_i}\right)$.

3.2 Boundary Conditions

To solve the governing partial differential equations, boundary conditions are required at all boundaries of the computational domain. The type of flow that is modeled is determined by the imposed boundary conditions. Therefore, it is important that the user specify these correctly and understands their role in the numerical algorithm (Versteeg and Malalasekera, 2007). If the value of the dependent variable is prescribed on the boundary, it is called a Dirichlet boundary condition. Whereas, if the gradient of the variable normal to the boundary is prescribed, it is referred to as a Neumann condition. The user may also apply a weighted combination of the Dirichlet and Neumann condition, named Robin boundary condition. In the present study, the boundary conditions are either velocity-specified or pressure-specified.

For transient problems, the initial values of the flow field variables have to be specified for the entire mesh. The assigned initial values are the starting point for the iterative solver.
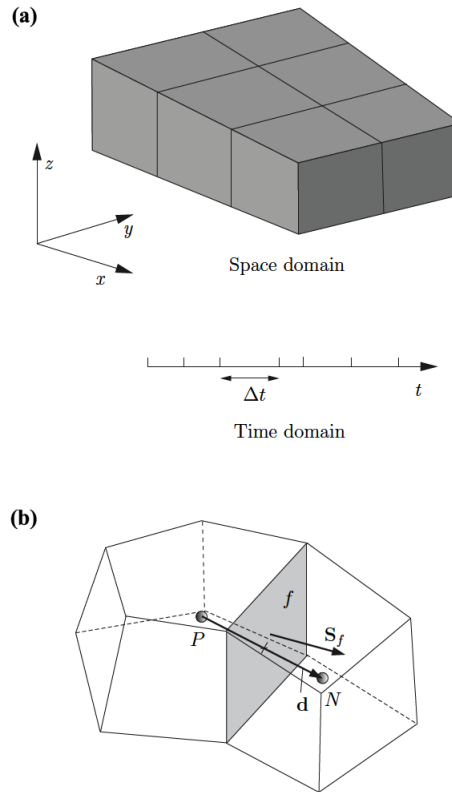
Figure 3.1:   (a) Spatial and temporal discretisation; (b) parameters in finite volume discretization (Greenshields, 2015a).

3.3   Finite Volume Method

Discretization of the space domain into a computational mesh consisting of cells is shown in figure 3.1(a). According to Çengel and Cimbala (2008), one can think of each cell as a control volume in which discretized versions of the continuity and Navier-Stokes equations are solved. The cells may have various shapes. However, the mesh used in the present work consists of hexahedral elements. The hexahedral's are built up of eight nodes, one in each corner, connected by lines. The lines form a total of six faces.

Two arbitrary, neighboring cells with some of the parameters defined in the FV method, are shown in figure 3.1(b). P and N denote the center of each control volume, and the distance between the neighboring centers is labeled d. The cell faces are named f, and the surface normal vector is $\vec{S_f}$. In OpenFOAM, the solution variables are defined at the center of each cell. Hence, the values at the cell faces, or boundaries, have to be interpolated from the values of the neighboring cell centers.

The solution procedure by finite volume discretization starts by integrating each term over a cell control volume Ω, bounded by a surface S. The resulting integral form of the continuity equation and the Navier-Stokes equation, is shown in equation 3.6 and 3.7, respectively.

$$\oint_S \vec{V} \cdot \vec{n} \, dS = 0 \tag{3.6}$$

$$\frac{\partial}{\partial t} \int_\Omega \vec{V} \, d\Omega + \vec{V} \oint_S V_n \, dS = \oint_S \left(\vec{\sigma} \cdot \vec{n} \right) dS \tag{3.7}$$

here, the $\vec{n}$ and V_n denote the normal vector and the velocity component which is normal to the surface S, respectively. Both the normal vector and the normal component of the velocity, are pointing out of the control volume.

Next, the volume and surface integrals in equation 3.6 and 3.7, are linearised using appropriate numerical schemes. Thus, by evaluating the linearised integral equations at all control volumes of the domain, a system of algebraic equations are constructed, that are commonly expressed in matrix form as:

$$[A][x] = [b] \tag{3.8}$$

Here, [A] is a symmetric matrix, [x] is the dependent variable and [b] is the source vector, suggested by Greenshields (2015a). These equations may then be solved through iterative methods. OpenFOAM offers several different solvers, suitable for specific applications. For the simulations in the present study, the pisoFOAM solver has been used, which utilizes the PISO algorithm.

3.4 The PISO Algorithm

"The PISO algorithm, which stands for Pressure Implicit with Splitting of Operators, (Issa, 1986) is a pressure-velocity calculation procedure developed originally for non-iterative computation of unsteady compressible flow" (Versteeg and Malalasekera, 2007). However, the PISO algorithm has successfully been applied as an iterative solver of the incompressible Navier-Stokes equation. The algorithm involves one predictor step and two corrector steps. Following is a brief overview of each step, based on the suggestions by Versteeg and Malalasekera (2007).

Predictor Step

In the predictor step, the algebraic equation system is solved, based on an initially guessed pressure field p^*. Thus, the temporary velocity components u_i^* are found. Here, $i = 1,2$ and 3 corresponding to the velocity in x, y and z-direction, respectively. However, the velocity components will not satisfy the continuity equation, unless the guessed pressure field is correct.

Corrector Steps

The first corrector step is introduced to obtain a corrected velocity field, u_i^{**}, that satisfies the continuity equation, by defining the correction fields $p^{'}$ and $u_i^{'}$, as shown in equation 3.9 and 3.10.

$$p^{**} = p^{*} + p^{'} \tag{3.9}$$

$$u_i^{**} = u_i^{*} + u_i^{'} \tag{3.10}$$

Hence, the pressure correction field $p^{'}$ is defined as the difference between the correct pressure p^{**} and the initial pressure p^{*}. The velocity correction $u_i^{'}$ are defined correspondingly. The resulting equations for the corrected velocity field, are substituted into the discretized continuity equation, which yields the first pressure correction equation. This pressure correction equation has to be solved, in order obtain the correction field $p^{'}$. Subsequently, the corrected pressure is used to calculate the correct velocity components u_i^{**}.

In the second corrector step, a twice-corrected velocity field u_i^{***}, is computed by solving the Navier-Stokes equation, once more. New pressure and velocity correction fields, $p^{''}$ and $u_i^{''}$, are defined such that:

$$p^{***} = p^{**} + p^{''} \tag{3.11}$$

$$u_i^{***} = u_i^{**} + u_i^{''} \tag{3.12}$$

In a similar fashion as the first corrector step, the pressure correction field $p^{''}$, is obtained by substituting the twice-corrected velocity field into the continuity equation. By inserting equation 3.9 into 3.11, the twice-corrected pressure field is obtained from:

$$p^{***} = p^{*} + p^{'} + p^{''} \tag{3.13}$$

Finally, the two times corrected pressure field p^{***}, is used to calculate the twice-corrected velocity components u_i^{***}. For the iterative PISO solver in OpenFOAM, the described sequence is repeated, until a user-specified residual is reached.

3.5 Properties of Numerical Solution Methods

When the governing equations are known accurately, Ferziger and Peric (2012) states that the differences between computed results and realistic results i.e. errors, arise from each part of the numerical solution procedure. Mainly, including approximations made in the discretization process and errors attained when solving the discretized equations by an iterative solver. The discretization errors may be reduced by dividing the computational domain into smaller cells, or by using interpolation schemes of higher accuracy. However, this may increase the computation time, drastically.

Although numerical results are always approximate, there are certain properties that the numerical solution should have, for obtaining the required accuracy and efficiency. According to Ferziger and Peric (2012), some of the most important properties include consistency, stability and convergence.

3.5.1 Consistency

When the governing equations are discretized by applying numerical schemes, a truncation error is introduced. The truncation error is estimated by replacing all the nodal values in

the discrete approximation by a Taylor Series expansion about a single point. This leads to a recovery of the original differential equation, in addition to a remainder which represents the truncation error. The truncation error must become zero when the mesh spacing $\Delta x_i \to 0$ and/or the time step $\Delta t \to 0$ to provide a consistent method. Truncation error is commonly proportional to a power of the grid spacing Δx_i and/or the time step Δt. If the most important term is proportional to $(\Delta x)^n$ or $(\Delta t)^n$ the method is called an nth-order order approximation (Ferziger and Peric, 2012). In OpenFOAM, the user is free to choose appropriate discretization schemes for every term of the governing equations.

In addition to applying consistent discretization schemes, the solution method has to be stable to obtain the exact solution as the step sizes go to zero ($\Delta t, \Delta x_i \to 0$).

3.5.2 Stability

A stable iterative method is one that does not diverge, which means that the numerical solution method will not magnify the errors. To obtain stability for an explicit method when diffusion is considered negligible, Ferziger and Peric (2012) outlines the following criterion:

$$\frac{U\Delta t}{\Delta x_i} < 1 \tag{3.14}$$

The term on the left-hand side of equation 3.14 is called the Courant-Friedrichs-Lewy (CFL) number. Where Δt is the time step, Δx_i is the cell size, and U is the local velocity at the evaluated cell. Therefore, the CFL number is calculated for every cell in the computational domain at every time step of the simulation. To maintain numerical stability, the maximum Courant number appearing in the simulation should be kept significantly lower than unity. In OpenFOAM, the maximum and mean CFL number are computed and displayed at every time step, and the user may assure numerical stability by adjusting the time step Δt.

3.5.3 Convergence

"A numerical method is said to be convergent if the solution of the discretized equations tends to the exact solution of the differential equation as the grid spacing tends to zero" (Ferziger and Peric, 2012). For non-linear problems, the convergence of a method is hard to demonstrate. This is also the case in the present study, with the non-linear convective term of the governing Navier-Stokes equation. For such problems, the convergence is usually examined by repeating the simulations on a successively refined grid. Thus, if the method is stable and the numerical schemes are consistent, the solution will normally converge to a grid independent solution for adequately small cell sizes. In the present work, the convergence is thoroughly investigated by varying the grid resolution, domain size and time step, in the grid dependency study.

Chapter 4

Computational Setup

4.1 Solution Procedure in OpenFOAM

Open Source Field Operation and Manipulation (OpenFOAM) is a C++ library, mainly used to produce executable codes, also known as applications. The applications consist of numerical solvers and utilities for solving continuum mechanics problems, which includes problems related to CFD. It is an open source software, owned by the OpenFOAM Foundation. The version used in the present work was released December 2015 (version 3.0.1). As illustrated in figure 4.1, the solution procedure in OpenFOAM consists of the three main components, pre-processing, solving and post-processing. Based on the solution procedure outlined by Çengel and Cimbala (2008), the components include the following steps:

1. A computational domain is chosen, and a grid is generated by dividing the domain into many small cells or control volumes. The quality of the results is highly dependent on the quality of the grid.

2. Appropriate boundary conditions are specified on each face of the computational domain. The type of boundary conditions is dependent on the kind of flow being simulated.
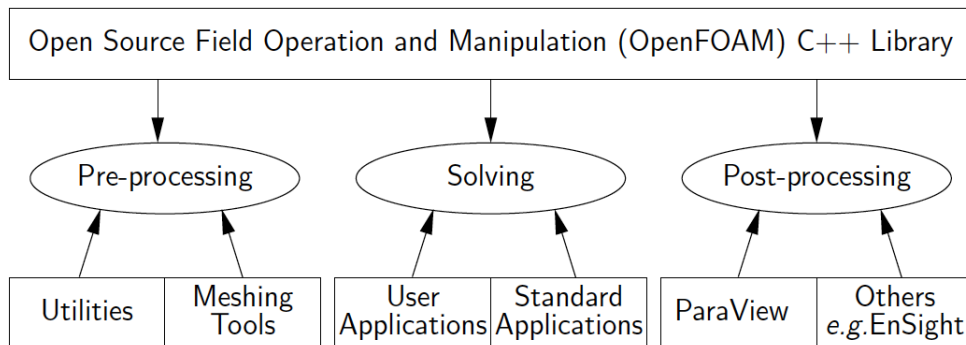
Figure 4.1: Overview of OpenFOAM structure (Greenshields, 2015b).

32

3. Starting values for the flow variables called initial conditions are specified over the entire grid.

4. The type of fluid and its associated properties are specified.

5. Numerical discretization schemes and solvers are chosen. Numerical schemes are typically applied to derivatives or interpolation of values from one point to another. In OpenFOAM, the user is completely free to choose the most appropriate schemes and solvers.

6. Starting from the initial conditions, discretized versions of the governing equations are solved at the center of each cell in the computational domain. The numerical solver iterates until a user-specified error tolerance is reached.

7. The calculated pressure and velocity fields are evaluated and visualized by different post-processing techniques.

4.2   File Structure of OpenFOAM Cases

OpenFOAM requires a certain file structure to start a simulation. The structure consists of three main directories as shown in figure 4.2. The solver settings and the numerical schemes are specified in the two files of the *system* directory, called *fvSolution* and *fvSchemes*, respectively. In *controlDict* the run parameters are set, such as start/end time, time step and write interval. The *constant* directory holds the entire description of the grid with the associated boundary conditions in the subdirectory *polyMesh*. Also, the *constant* directory specifies the physical properties of the fluid. The 'time' directories, which contain the flow field data at each time step, are named by the actual instant for each directory. The initial and boundary conditions for the pressure and velocity fields are stored in a directory, named *0*. As the simulation runs, new directories will be constructed with a time step given by the write interval, specified in the *controlDict*.

   Examples of the *fvSchemes*, *fvSolution* and *controlDict* files applied in the present numerical simulations, are respectively included in appendix A.1, A.2 and A.3.

4.3   Pre-Processing

Before the simulations are started, the points 1 to 5 described in the solution procedure of section 4.1 have to be performed. This sequence is called the pre-processing. The crucial step to obtain realistic results is the grid generation, which is also the most time-consuming part of the pre-processing.

4.3.1   Grid Generation

The grid generation is basically to define the cells in which the governing equations are solved. This is either done in the CFD software or by a third-party grid generation program. In this work, the meshing is done in Mega, which is developed in-house by Professor Håvard Holm.
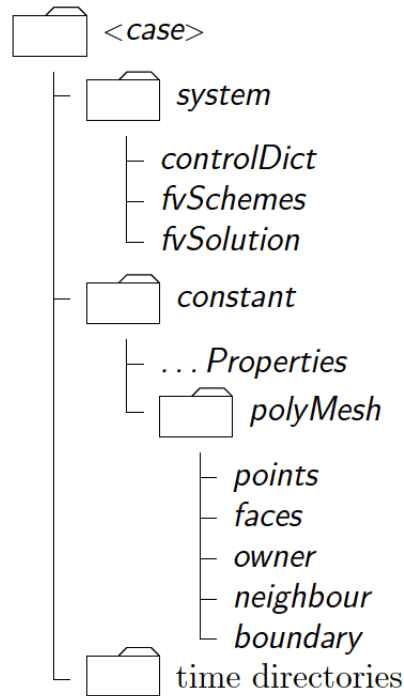
Figure 4.2: Structure of a case directory in OpenFOAM (Greenshields, 2015b).

Grids are either structured or unstructured. A structured grid contains equally shaped cells, whereas an unstructured grid consists of cells of various forms. Typical shapes for three-dimensional cells are hexahedrons, prisms or tetrahedrons (Çengel and Cimbala, 2008). The three types are shown in figure 4.3, along with the number of faces for each case. In the present thesis, a structured multiblock grid consisting of hexahedral cells with six faces, is utilized. Since the evaluated geometry of the present work is fairly straightforward, the structured grid is favorable, instead of an unstructured. Additionally, when computing boundary layers, the grid has to be highly resolved close to the no-slip wall. Therefore, a structured grid is favorable, since it enables a much finer grid resolution than an unstructured, for the same amount of cells (Çengel and Cimbala, 2008).

However, of much greater importance than the type of grid, is the quality of the grid. In OpenFOAM, the *checkMesh* utility checks the validity of the mesh, by calculating various parameters. Some of the factors that affect the quality of the grid are the cell skewness, change in cell size, aspect ratio and mesh non-orthogonality. The following is a brief explanation of the mentioned factors, and how they are calculated in the *checkMesh* utility.

Skewness

Stated by Çengel and Cimbala (2008), the skewness of a cell is defined as the departure from symmetry and is the most important metric to consider when constructing a mesh. To avoid convergence difficulties and inaccuracies in the numerical solution, the operator has to make sure that the individual cells are not highly skewed. There are different ways of evaluating skewness. The *checkMesh* utility evaluates the skewness by measuring the distance between
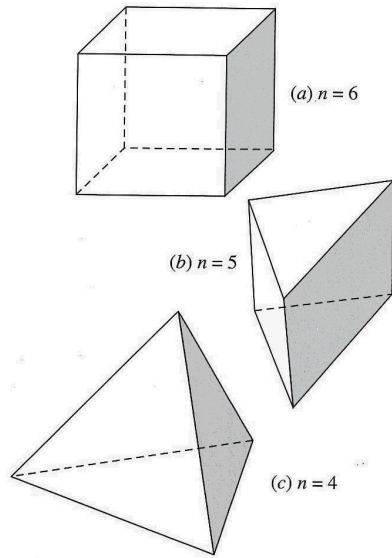
Figure 4.3: Typical three-dimensional cells in CFD along with the number of faces n for each type. (a) Hexahedral; (b) prism; (c) tetrahedral (Çengel and Cimbala, 2008).

the intersection of the line connecting two cell centers with their common face and the center of that face. The skewness is illustrated as δ in figure 4.4(a) for two neighboring cells with cell centres P and N, and common face f. If the skewness of the left cell in figure 4.4(a) is decreased, the distance δ will decrease. Hence, the magnitude of the computed skewness should be kept as low as possible. Both mean and maximum skewness for the entire mesh, are calculated in the *checkMesh* utility.

Non-Orthogonality

The non-orthogonality is expressed as the angle between the line connecting two cell centers and the normal vector of their common face. In figure 4.4(b), the non-orthogonality is given by the angle θ, for two neighbouring cells with cell centres P and N, and common face f.
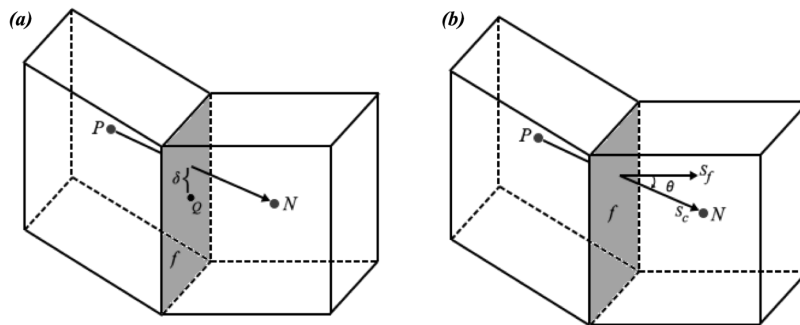
Figure 4.4: Skewness and non-orthogonality calculated for two neighbouring hexahedral cells. (a) Skewness; (b) non-orthogonality.
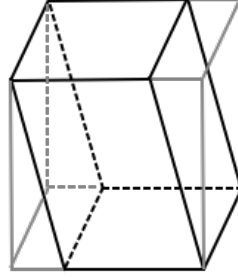
Figure 4.5: Bounding box of a hexahedral cell. The cell is drawn with black lines, whereas the bounding box is extended by the light gray lines.

The vector $\vec{S}_c$ connects the cell centres, and $\vec{S}_f$ is the normal vector of *f*. Similarly, as the skewness, the optimal magnitude of the non-orthogonality is zero, meaning that the cells are orthogonal. The *checkMesh* utility calculates the maximum and average non-orthogonality for the entire mesh. Based on the degree of orthogonality, the OpenFOAM user may introduce a non-orthogonal correction factor, for both the numerical schemes and solvers. "Generally, the uncorrected and orthogonal schemes are only recommended for meshes with very low non-orthogonality (e.g. maximum 5°). At non-orthogonality above 80°, convergence is generally hard to achieve" (Greenshields, 2015b).

Aspect Ratio and Abrupt Change in Cell Size

Other factors that affect the quality of the mesh are the abrupt change in cell size and high aspect ratio. These factors may cause problems, worsening the numerical accuracy and convergence (Çengel and Cimbala, 2008). In OpenFOAM, the aspect ratio of a particular cell is set to the largest of either the face aspect ratio (Λ_{face}), or the cell aspect ratio (Λ_{cell}). The face aspect ratio is simply the ratio between longest and shortest edge of each face. The *checkMesh* utility calculates the cell aspect ratio by the following equation:

$$\Lambda_{cell} = \frac{\mid ax \mid + \mid ay \mid + \mid az \mid}{6v^{2/3}} \tag{4.1}$$

here, *ax*, *ay* and *az*, are the area for each defining face of the bounding box of the cell, and *v* is the volume. The bounding box of a moderately skewed hexahedral cell, is drawn by the light grey lines of figure 4.5. The optimal aspect ratio is $\Lambda = 1$.

4.3.2 Computational Domain and Grid

Figure 4.6(a) depicts a perspective view of the three-dimensional domain, used to study the flow around a prolate spheroid. The overall dimensions of the domain in x, y and z-direction, are given by L_x, L_y and L_z, respectively. A clip filter in the (x,z)-plane at the middle of the domain y-axis, is applied to give an overview of the grid, and the location of the prolate spheroid. Half of the prolate spheroid surface is seen by the light gray area, inside the mesh. It is placed with its center at the origin of the right-handed coordinate system, and the major axis aligned with the z-axis. The length of the major axis is 4/3 times the minor axis,
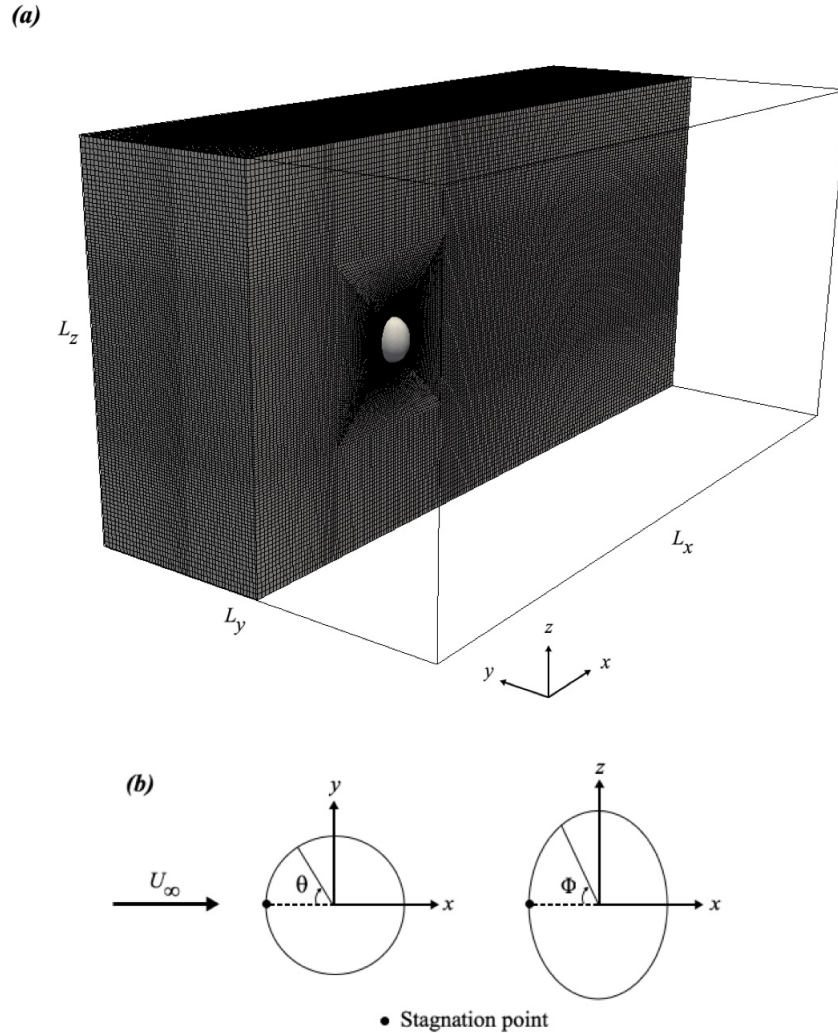
Figure 4.6: Computational domain. (a) A cut of the computational domain; (b) cross sections of the minor and major plane, illustrating how a point on the prolate spheroid surface is defined by θ and ϕ.

with the length of the minor given by the diameter, D. Because of the low aspect ratio, the spanwise length L_z, and transverse length L_y of the domain are equal. The grid is designed for the flow to propagate in the positive x-direction.

The cross-sectional slices in figure 4.6(b), show how a unique point on the surface of the prolate spheroid is defined. The angles, θ and ϕ, are measured from the front stagnation point in the (x,y) and (x,z)-plane, respectively. This way of describing a point on the surface is inspired by El Khoury et al. (2012).

A two-dimensional slice of the mesh at the middle (x,y)-plane, is shown in figure 4.7(a), illustrating the relative length of the domain in the x- and y-direction. The two dotted black lines in the figure, intersect at the center of the spheroid. Hence, the domain extends a distance a, both upstream and in the cross-flow y-direction from the spheroid's center. Similarly, the domain extends a distance a in the spanwise z-direction. Downstream of the
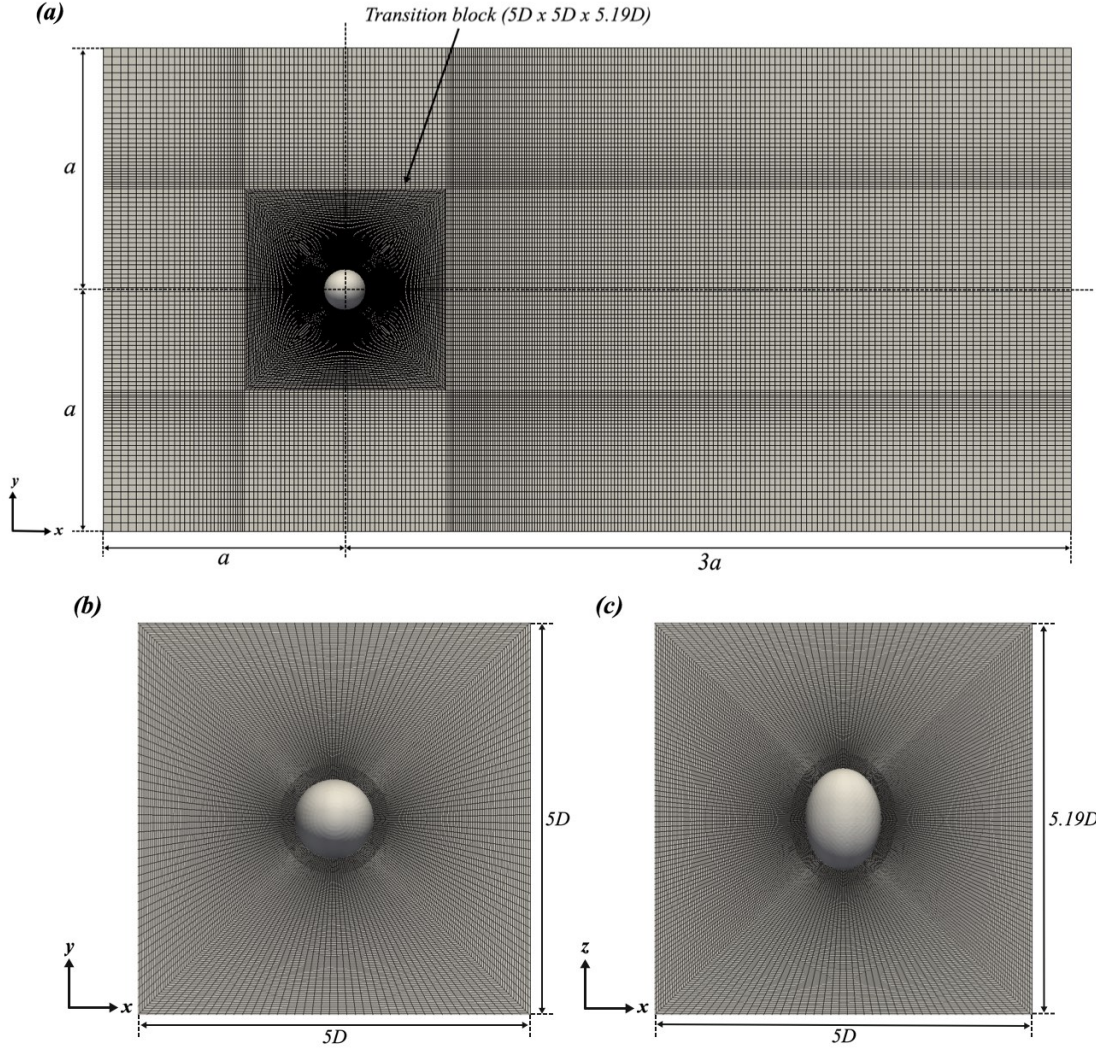
Figure 4.7: Two-dimensional slices of the grid. (a) (x,y)-plane of the entire grid; (b) (x,y)-plane of the *transition block*; (c) (x,z)-plane of the *transition block*.

spheroid center, the domain stretches a distance *3a*, to fit several wake structures. Different values of *a* will be tested in the grid dependency study to find a sufficient domain size.

The block structure of the mesh is indicated by the regions of changing cell size, in figure 4.7. The outer parts of the mesh, contain blocks of relatively coarse hexahedral cells. In the x, y and z-directions, the grid is slightly graded with smaller cell sizes toward the prolate spheroid. As the surface of the prolate spheroid is approached, the cell sizes are significantly reduced, to resolve the rapid flow variations in the boundary layer. Closest to the surface, the prolate spheroid is embedded in a body-fitted O-shaped mesh, named the *inner block*. The *inner block* has a constant radial thickness of $0.2D$, to easily control the size, and maintain a high quality of the cells. In the *transition block*, the highly refined grid is gradually coarsened, to achieve a smooth cell size transition from the *inner block* to the outer parts of the grid. The *transition block* block has an overall size of $5D$ in both x and y-direction, and $5.19D$ in the spanwise z-direction.
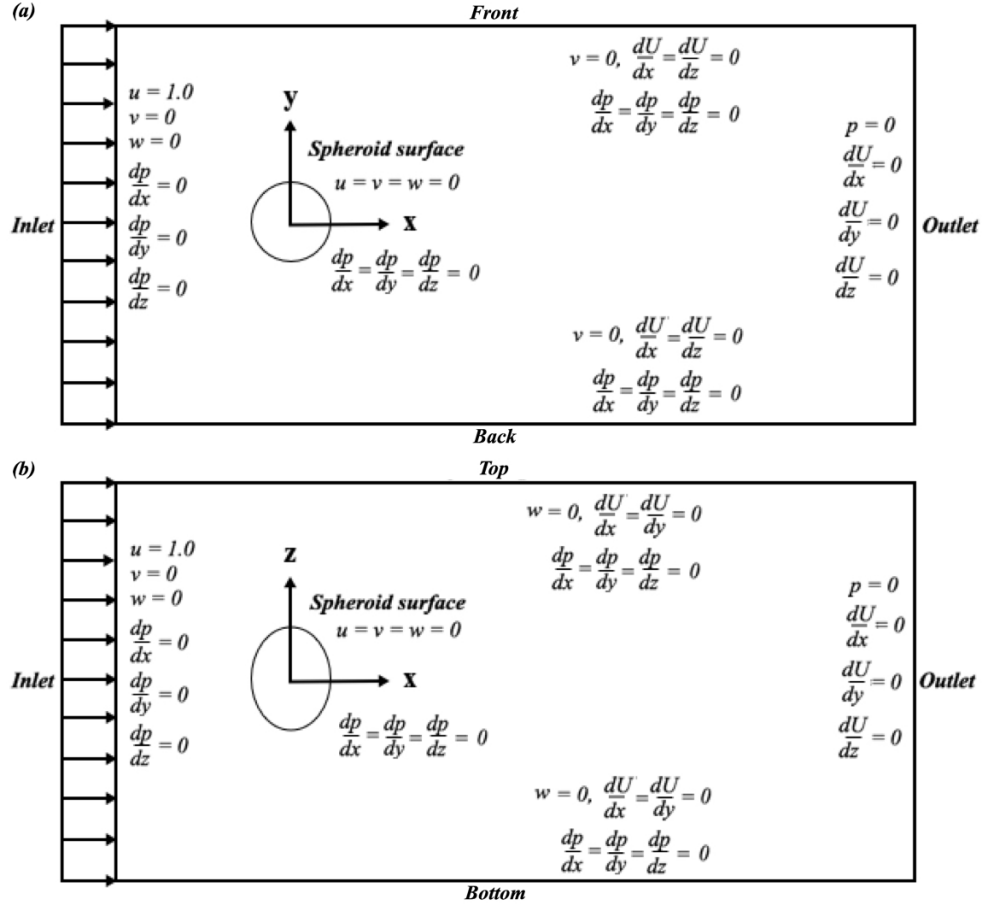
Figure 4.8: Employed boundary conditions. (a) (x,y)-plane; (b) (x,z)-plane.

Two-dimensional slices of the *transition block* in the middle (x,y) and (x,z)-plane, are shown in figure 4.7(a) and 4.7(b), respectively. The *inner block* is indicated by the darker colored regions in the close vicinity of the spheroid surface. As the cells in the *transition block* get gradually coarser, they also get more radially stretched towards the outer edges of the block, especially at the corners. The reason is that the body-fitted O-mesh in the *inner block* is slowly turned into a rectangular H-mesh. Hence, the cells located near the corners of the *transition block* will obtain a worsened quality by an increased skewness. However, the skewness was found to be sufficiently low, by the *checkMesh* utility in OpenFOAM.

4.3.3 Boundary Conditions and Initial Values

For the present work, the domain is supposed to represent an infinite fluid. Hence, the boundaries should not influence the flow field around the spheroid. In practice, this means that the boundary conditions should not impose any changes to the flow field variables.

The (x,y) and (x,z)-plane of the computational domain with its prescribed boundary conditions, are shown in figure 4.8(a) and 4.8(b), respectively. The spheroid surface is supposed to behave as a solid wall. Therefore, no fluid should be able to pass through the surface, in addition to a no-slip condition. The wall is modeled by putting all velocity components to

Table 4.1: Boundary conditions and the boundary types specified in the OpenFOAM case.

Patch	Boundary condition		Boundary type (OpenFOAM)
	Pressure	Velocity	
Spheroid	$\frac{dp}{dx} = \frac{dp}{dy} = \frac{dp}{dz} = 0$	$\boldsymbol{U} = (u,\ v,\ w) = 0$	*wall*
Inlet	$\frac{dp}{dx} = \frac{dp}{dy} = \frac{dp}{dz} = 0$	$u = 1.0,\ v = w = 0$	*patch*
Outlet	$p = 0$	$\frac{\partial \mathbf{U}}{\partial x} = \frac{\partial \mathbf{U}}{\partial y} = \frac{\partial \mathbf{U}}{\partial z} = 0$	*patch*
Front and back	$\frac{dp}{dx} = \frac{dp}{dy} = \frac{dp}{dz} = 0$	$v = 0,\ \frac{\partial \mathbf{U}}{\partial x} = \frac{\partial \mathbf{U}}{\partial z} = 0$	*slip*
Top and bottom	$\frac{dp}{dx} = \frac{dp}{dy} = \frac{dp}{dz} = 0$	$w = 0,\ \frac{\partial \mathbf{U}}{\partial x} = \frac{\partial \mathbf{U}}{\partial y} = 0$	*slip*

zero, as well as applying a zero gradient for the pressure. The inlet, shown at the left edge, is given a constant velocity $u = 1.0$, and $v = w = 0$. This boundary condition is referred to as a velocity inlet. For such inlet conditions Çengel and Cimbala (2008) states that the pressure is not specified, as that would lead to a mathematical over-specification since both pressure and velocity are coupled in the governing equations. Instead, the pressure is given a zero gradient. Thus, the pressure will not change in any direction, at the inlet. At the outlet, the pressure is set to zero, hence assumed to be equal to the pressure of the undisturbed flow. Similar to the inlet, the velocity is not specified at a pressure outlet. However, the velocity vector is prescribed a zero gradient. A free-slip condition is imposed along the sides of the computational domain, named *front, back, top* and *bottom* in figure 4.8. This means that the velocity component normal to the boundary face is set to zero, whereas a zero gradient is given for the tangential components. When the slip-condition is applied to a scalar, it is set to a zero gradient, which applies to the pressure.

As stated in section 4.2, the boundary conditions of an OpenFOAM case are specified in the *polyMesh* subdirectory, and in the initial time step directory *0*. The basic type of boundaries are stated in *polyMesh*, whereas more specific boundary and initial conditions are given in *0*. The boundary types used in this work are *wall, patch* and *slip*. An overview of the boundary types and conditions, is given in table 4.1.

Starting values of the internal fields for pressure and velocity are set to zero, for all simulations. Hence, the fluid starts at rest and is gradually accelerated until the inflow velocity is reached.

4.4   Numerical Schemes and Solvers

4.4.1   Numerical Schemes

The discretization schemes applied to each term in the governing equations are specified in the *system* directory, by the file *fvSchemes*. Numerical schemes are mainly applied to derivatives in time and space. However, since the equations are solved at the center of each cell, interpolations schemes are specified to compute values at the cell faces. An overview of the schemes applied in the present work is given in table 4.2. For an example of the complete *fvScheme* used in the present work, reference is given to appendix A.1.

The time derivative is discretised by the implicit, first order *Euler* scheme. Even though

this scheme is less accurate than the second order *backward Euler* and *Crank-Nicholson* schemes, it is chosen for its stability and convergence properties. A standard finite volume discretization of Gaussian integration is applied for the gradient term. As described in Greenshields (2015b) the Gaussian integration is based on summing values on cell faces. Therefore, an associated interpolation scheme has to be chosen. Linear interpolation is an effective choice, and therefore also selected in the present work. The same scheme for discretization and interpolation is also chosen for both the divergence and Laplacian terms. For the latter term, Gauss scheme is the only choice of discretization (Greenshields, 2015b). Also, for the Laplacian term, a surface normal gradient scheme has to be specified. The surface normal gradient is the component normal to a cell face, of the gradient in each cell that is connected to that face. In the present thesis, the second order *corrected* scheme was chosen for this purpose. For the general field interpolations, a linear scheme was selected.

Table 4.2: Numerical schemes applied in the present work.

Term description	Text expression	Numerical Scheme
Time derivative	$\frac{\partial \phi}{\partial t}$	Euler
Gradient	$\nabla \phi$	Gauss linear
Divergence	$\nabla \cdot \phi$	Gauss linear
Laplacian	$\nabla^2 \phi$	Gauss linear corrected
Surface normal gradient	$\mathbf{n}_f \cdot (\nabla \phi)_f$	Corrected
Interpolation	-	Linear

4.4.2 Solver Settings

The numerical solvers, algorithms and tolerances are specified by the *fvSolution* file, in the *system* directory. An example of the solver settings applied in this work is given in appendix A.2.

In addition to the solver *application*, which describes the set of equations and algorithms to solve the particular problem, linear solvers that are used for each discretized equation, have to be specified for an OpenFOAM case (Greenshields, 2015b). In the present work, equations for pressure and velocity are solved, hence solvers for p and U are prescribed in *fvSolution*. A geometric-algebraic multi-grid (GAMG) solver is applied to the pressure. The GAMG solver first computes a quick solution on a coarse grid and maps the solution onto a gradually finer mesh, the final grid being the one specified by the user. The coarsest mesh level is specified by *nCellsInCoarsestLevel*. A conceptual illustration of the method is shown in figure 4.9. As the algorithm is refining the mesh, two Gauss-Seidel smoother sweeps are executed, specified by *smoother* and *nPostSweeps* in the *fvSolution* file. The solver for the velocity U, is a preconditioned bi-conjugate gradient (PBiCG) solver, with a Diagonal incomplete-LU (DILU) preconditioner. The preconditioner is applied to acquire better convergence compared with the original system.

For the numerical solvers, the equation residual is decreased with successive iterations. According to Çengel and Cimbala (2008) a residual is a measure of how much the solution to a given transport equation deviates from the exact. In OpenFOAM, the residual is computed
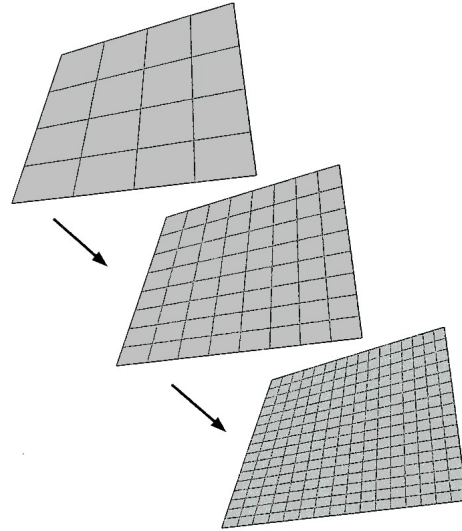
Figure 4.9: Multigrid method for solving the equations of motion. Solutions are obtained on a coarse grid first to speed up convergence (Çengel and Cimbala, 2008).

by substituting the temporary solution into the governing equation and taking the magnitude of the difference between the left and right-hand sides (Greenshields, 2015b). After each iteration, the current residual is re-evaluated. Thus, the solver stops either if the residual falls below the tolerance specified by *tolerance*, or if the ratio of the current residual to the initial falls below the relative tolerance provided by *relTol*. The solver tolerance for p and U are set to 10^{-6} and 10^{-5}, respectively.

4.5   Parallel Computing

The OpenFOAM simulations of the present study have been run in parallel, on the SGI Altix ICE X system, named Vilje. The system is procured by NTNU together with the Norwegian Meteorological Institute and UNINETT Sigma. Vilje consists of 1404 nodes with two eight-core 2.6 GHz processors per node.

As stated by Greenshields (2015b), "The process of parallel computation involves: decomposition of the mesh and fields; running the application in parallel; and, post-processing the decomposed case". Before running the solver, the mesh has to be decomposed into a number of sub-domains, equal to the number of cores used for the computations. For most of the simulations, 64 cores have been utilized. *Scotch* decomposition was chosen, which requires no geometric input. This method of decomposing the mesh tries to minimize the number of processor boundaries. After running the simulations in parallel, the user may post-process each part of the decomposed domain, or reconstruct the mesh to obtain the entire domain. The latter option was chosen for the post-processing in the present study.

4.6 Post-Processing

The final stage of the CFD solution procedure is the post-processing of the calculated pressure and velocity fields. Visualization of the OpenFOAM results was performed by the utility *paraFoam*. In addition to the visualization, drag and lift coefficients, as well as data probed at specific locations in the wake, were analyzed in MATLAB.

4.6.1 Flow Visualization

ParaFoam is the main post-processing tool in OpenFOAM. It uses the open source visualization software ParaView, which provides a wide variety of visualization possibilities. In the present thesis, the flow field is visualized by investigating contour and vector plots of two-dimensional slices, as well as three-dimensional isosurfaces. Both pressure, velocity and vorticity are presented by respective techniques.

Vorticity

When simulations in OpenFOAM are finished, the vorticity $(\omega_x, \omega_y, \omega_z)$ is calculated by the *vorticity* utility. In this case, the vorticity vector are calculated according to equation 1.3, given in section 1.1.3. The vorticity tells how the velocity vector changes as if we move in a direction perpendicular to it. Hence, its magnitude will be largest close to the vortex core and decrease as the distance to the core increases.

Another way of visualizing the vortex structures of the wake is by employing the λ_2-definition. In OpenFOAM, this is done by the utility *lambda2*, executed in a similar fashion as *vorticity*. The λ_2-definition is briefly described in section 1.1.4 of the present thesis.

Streamlines

A curve that is tangent everywhere to the instantaneous local velocity vector is a streamline (Çengel and Cimbala, 2008). Therefore, the streamlines are suitable to indicate the instantaneous local directions of a flow field. According to Çengel and Cimbala (2008), the mathematical expression for a streamline is as follows:

$$\frac{dr}{V} = \frac{dx}{u} = \frac{dy}{v} = \frac{dz}{w} \tag{4.2}$$

where V is the magnitude of the velocity vector $\vec{V} = u\vec{i} + v\vec{j} + w\vec{k}$, and dr is the magnitude of an infinitesimal arc length $d\vec{r} = dx\vec{i} + dy\vec{j} + dz\vec{k}$. By integrating equation 4.2 with the calculated velocity fields, equations for the streamlines are obtained.

4.6.2 Analysis of the Wake Fluctuations

The frequencies appearing in the wake are non-dimensionalised by the Strouhal number, defined by equation 1.2 in section 1.1.2. The shedding frequency, f_v, oscillates with the same frequency as the lift force acting on the body. However, lift is a result of integrating the pressure over the surface of the prolate spheroid. Thus, the computed lift might suffer

Table 4.3: Data sampled at eight different probe locations.

Probe	Location		
	x	y	z
Probe 1	1D	0.2D	0
Probe 2	1D	-0.2D	0
Probe 3	1D	0.2D	0.33D
Probe 4	1D	-0.2D	0.33D
Probe 5	1D	0.2D	-0.33D
Probe 6	1D	0.2D	-0.33D
Probe 7	5.75D	0.3D	0
Probe 8	5.75D	-0.3D	0

inaccurate numerical integration. A more reliable method to assess the wake fluctuations is by evaluating the oscillating pressure or velocity in the near-wake region. The vortex shedding frequency may be determined by a spectral analysis of a measured time series. In the present work, the spectral analysis was performed by the Fast Fourier Transform (FFT) algorithm in MATLAB. For a detailed example of the MATLAB script performing the FFT analysis, reference is given to appendix B.1.

Pressure and velocity data are sampled at eight probe locations in the wake, at every time step of the simulation. The different probe locations are specified in table 4.3. Hence, all probes are located in the wake of the prolate spheroid, either $1D$ or $5.75D$ downstream.

4.6.3 Force Coefficients

For the present simulations, the drag and lift coefficients are computed at every time step. The force coefficients are defined as:

$$C_D = \frac{F_D}{\frac{1}{2}\rho U_\infty^2 A} \tag{4.3}$$

$$C_L = \frac{F_L}{\frac{1}{2}\rho U_\infty^2 A} \tag{4.4}$$

Where F_D and F_L are the drag and lift force acting on the body. The density of the fluid is given by ρ, and U_∞ is the undisturbed inflow velocity. A is the projected area, which in this case has the shape of an ellipse. Both mean and maximum values of the force coefficients are calculated by inserting associated values for either F_D or F_L. The lift coefficient for the spheroid in an infinite fluid and uniform inflow, will might get an average value very close to zero, as seen for a circular cylinder. In that case, small changes in the lift will cause relatively large changes in the mean value. In that case, it does not make much sense to compute the mean lift. Therefore, the root-mean-square (RMS) value of the lift coefficient is calculated, according to equation 4.5.

$$C_L^{RMS} = \frac{\sqrt{\frac{1}{N}\sum_{i=1}^{N} F_{L,i}^2}}{\frac{1}{2}\rho U_\infty^2 A} \tag{4.5}$$

Where N is the total number of samples for the particular time series. The drag force will have a mean value $F_D^{'} > 0$. The associated mean drag coefficient is calculated as follows:

$$C_D^{'} = \frac{\frac{1}{N}\sum_{i=1}^{N} F_{D,i}}{\frac{1}{2}\rho U_\infty^2 A} \tag{4.6}$$

Chapter 5

Results

The results obtained from the numerical simulations are presented in this chapter. First, the outcome of a thorough grid dependency study for Reynolds number $Re = 300$, is given. This particular Re is chosen due to the fact that it is investigated for most of the reviewed literature included in chapter 2. Also, the flow at $Re = 300$, is expected to attain a periodic flow similar to a sphere, making it meaningful to compare the results as e.g. mean drag and shedding frequency. Subsequently, grid independent solutions for $Re = 100, 200, 250, 300$ and 500, are presented by means of various post-processing techniques. The results are continuously compared to existing literature, to validate the findings, and relate the $L_R = 4/3$ prolate spheroid to similarly shaped bluff bodies.

5.1 Grid Dependency Study

As stated by Çengel and Cimbala (2008), it is of great importance for CFD users to test if their solution is grid independent. A high-quality grid is crucial to obtain reliable results. In the present work, the grid dependency was studied by varying the grid resolution in the proximity of the prolate spheroid, domain size and time step. A convergence criterion of 5% change between following grids is utilized in the convergence study by Ong et al. (2010). However, due to the fact that Ong et al. (2010) simulated turbulent flow at Reynolds numbers in the range $Re = 10^4 - 10^6$, a more strict criterion of 1-3% is suggested for the present study simulating low Re flow. Hence, any of the assessed parameters, should not vary more than 1-3% between two successive grids when varying grid resolution, domain size or time step. To assess convergence, the following parameters were computed from a time series, after the simulation had reached steady state:

- Mean drag coefficient (C_D'). Computed as shown in equation 4.6.

- Maximum drag coefficient (C_D^{max}).

- Root-mean-square value of the lift coefficient (C_L^{RMS}). Calculated according to equation 4.5.

- Strouhal number of the dominant frequency appearing in the wake. St is determined by a Fast Fourier Transform of the transverse velocity sampled at *probe 7* defined in
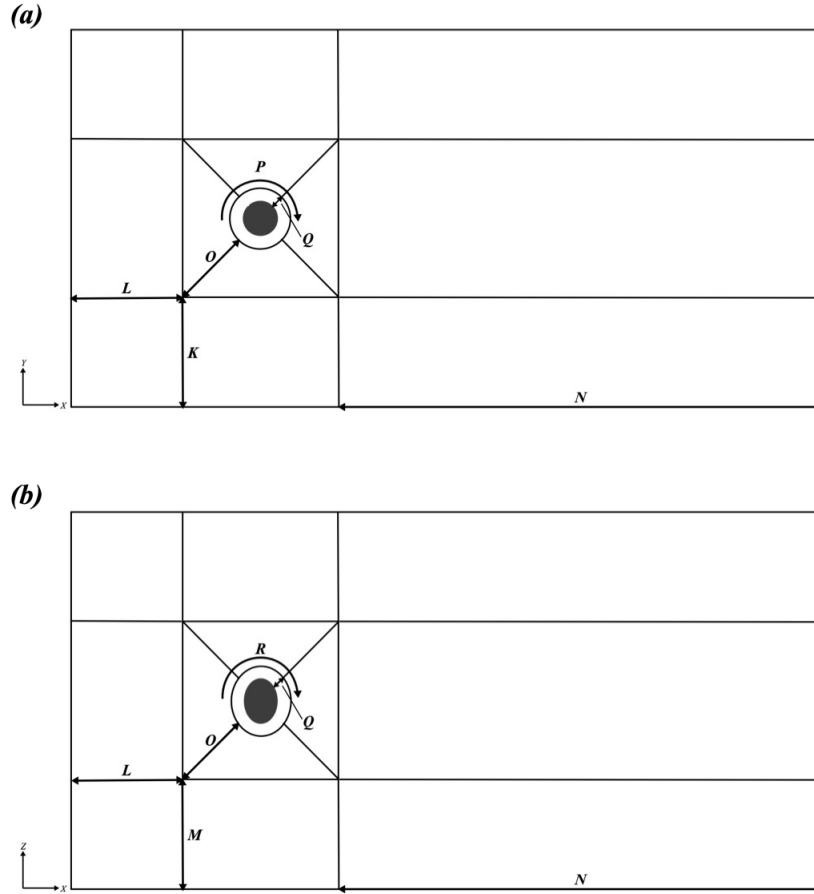
Figure 5.1: Element distribution. Number of cells is defined along the lines *K, L, M, N, O, P, Q, R*. (a) (x,y)-plane; (b) (x,z)-plane.

table 4.3.

- Mean pressure (p'), computed from the sampled pressure at all probes, defined in table 4.3.

5.1.1 Boundary Layer Resolution

The first part of the grid dependency study was performed by varying the number of cells close to the spheroid surface, to sufficiently resolve the velocity profile inside the boundary layer. It is the no-slip condition on the surface that gives rise to the rapid velocity change, normal to the wall. If the grid is too coarse, the velocity changes might not be captured properly, and therefore yield incorrect results. The boundary layer thickness, δ, is assumed to be in the order of $1/\sqrt{Re}$, according to theory by Schlichting (1979). Hence, the grid refinement should mainly be assessed within the $0.2D$ thick *inner block*, described in section 4.3.2.

Figure 5.1(a) and 5.1(b), outline the block structure in the mid (x,y) and (x,z)-plane

Table 5.1: Boundary layer refinements.

Mesh	Number of elements along line #								Minimum cell size			Number of cells
	P	Q	R	O	K	L	M	N	Δr/D	Δs_1/D	Δs_2/D	
Very coarse	180	10	240	50	30	30	30	100	0.0158	0.0174	0.0154	3 206 250
Coarse	180	20	240	50	30	30	30	100	0.0060	0.0174	0.0154	3 557 250
Medium	360	20	380	50	30	30	30	100	0.0060	0.0087	0.0097	8 124 000
Fine	360	30	400	60	30	30	30	100	0.0030	0.0087	0.0092	8 907 000
Very fine	400	40	420	60	30	30	30	100	0.0016	0.0079	0.0088	11 236 000

of the grid, respectively. The number of cells in the radial direction of the *inner block*, is specified by the number Q. Whereas the amount of cells along the spheroid surface in the (x,y) and (x,z)-plane, is given by P and R, respectively. For the *transition block*, only the radial number of cells has to be defined, given by O. The cell distribution of the outer blocks, is defined by K, L, M and N, as illustrated in figure 5.1.

The domain size and time step utilized when assessing the boundary layer resolution, are exclusively based on the numerical simulations in El Khoury et al. (2012). The computational setup presented by El Khoury et al. (2012) are briefly described in section 2.3.1. The authors used a domain with a minimum distance of $5D$ between the surface of the body and its borders. Therefore, the present domain size, a, was set equal to $6D$, resulting in a streamwise length $L_x = 24D$, transverse width and spanwise height, $L_y = L_z = 12D$. The time step was kept constant and equal to $\Delta t = 0.002D/U_\infty$. A Reynolds number of 300, was obtained by a spheroid diameter of $D = 2\ m$, inflow velocity of $u = 1.0\ m/s$, and kinematic viscosity of $\nu = 0.0067\ m^2/s$. For every grid configuration, the simulations were run for a total of $200D/U_\infty$, equal to 100 000 time steps, which was found to be sufficient for every grid to reach a steady state flow.

For the *inner block*, five different configurations were chosen, with a varying number of cells in the radial and tangential direction. An overview of the mesh refinements, named *very coarse, coarse, medium, fine* and *very fine*, is given in table 5.1. The radial distance to the first node from the spheroid surface is denoted Δr. Whereas, the cell length along the spheroid surface in the (x,y) and (x,z)-plane, is given by Δs_1 and Δs_2, respectively. The minimum radial thickness varies from $0.0158D$ for *very coarse*, to $0.0016D$ for *very fine*. Therefore, the minimum radial thickness for the coarsest grid is about ten times larger than the finest grid.

The results, in terms of force coefficients, pressure and Strouhal number, are shown in figure 5.2 and table 5.2. In the figure, the markers on each line, represent the computed result from each grid of different cell refinement. As seen in figure 5.2(a), the maximum and mean drag coefficient, vary analogous, with the maximum values slightly above the mean. Unexpectedly, the smallest changes in C_D' and C_D^{max}, were found for the coarsest grids, as demonstrated in the two leftmost columns of table 5.2. However, large relative changes are seen for both the mean pressure and Strouhal number, for the same grids. Therefore, the relative change between the *fine* and *very fine* grid, of $\Delta C_D' = $ -1.06% and $\Delta C_D^{max} = $ -1.46%, is considered to show best convergence. The RMS value of the lift coefficient was found to
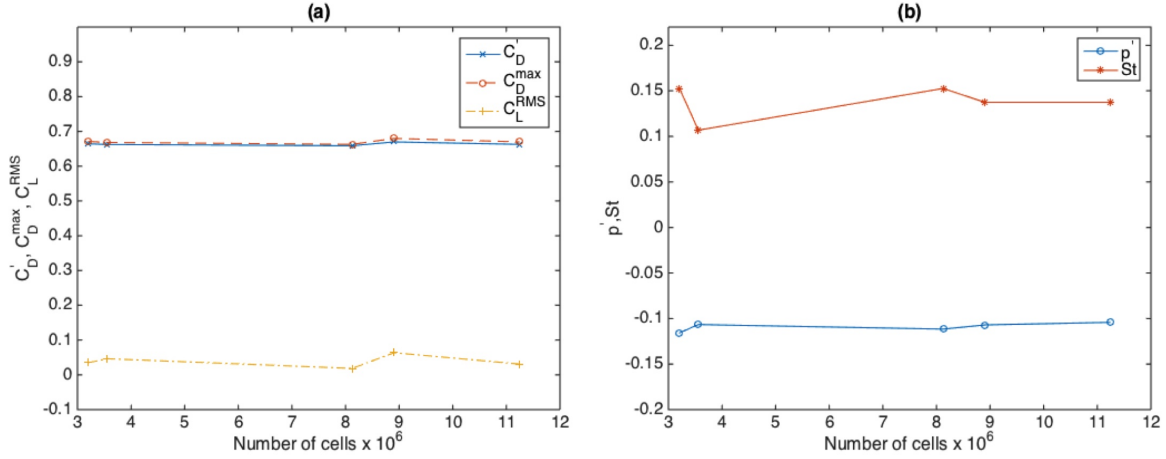
Figure 5.2: Results for varying grid refinement. (a) Mean drag coefficient, maximum drag coefficient and RMS of lift coefficient; (b) mean pressure at probes and Strouhal number.

Table 5.2: Percentage change in results between successive grid refinements.

Successive grids	Percentage change				
	$\Delta C_D'$	ΔC_D^{max}	ΔC_L^{RMS}	$\Delta p'$	ΔSt
Very coarse → coarse	-0.30	-0.42	31.91	7.87	-10.03
Coarse → medium	-0.53	-0.82	-59.83	-4.69	11.14
Medium → fine	1.67	2.58	241.94	4.12	-10.03
Fine → very fine	-1.06	-1.46	-51.10	2.62	0.00

be close to zero, in the range $C_L^{RMS} = 0.0186$ - 0.0636, for all the tested grids. As shown in table 5.2, large relative changes are obtained for C_L^{RMS} between successive grids, although the changes in magnitude are small. Hence, the percentage change of C_L^{RMS}, was considered a useless convergence indicator at this point of the convergence study.

Results in terms of mean pressure and Strouhal number are presented in figure 5.2(b), and in the two rightmost columns of table 5.2. The smallest percentage change for p', is between the *fine* and *very fine* grid, and equal to 2.62%. Additionally, no change in *St* was found between the two particular grids.

To further investigate the grid refinement in the boundary layer, velocity profiles close to the spheroid surface are plotted in figure 5.3 and 5.4. For both figures, instantaneous velocity for the *very coarse*, *medium* and *very fine* grids, are depicted. In figure 5.3, the velocity in the x-direction is sampled at each cell center, along a line normal to the surface. The leftmost images show the results, sampled up to a normal distance of $0.7D$, whereas the right images are zoomed in at the inner $0.2D$, to reveal how well the grid resolves the rapid velocity change in the vicinity of the wall. The velocity profiles are sampled at the spanwise middle section, corresponding to $\phi = 0$, at three different circumferential positions, making an angle of $\theta = 80°$, $100°$ and $120°$, from the stagnation point. Figure 5.3(b), indicates that the *very coarse* grid fails to smoothly resolve the velocity gradient, especially for $\theta = 120°$, when reversed flow occurs. However, the *medium* and *very fine* grids, with 20 and 40 cells
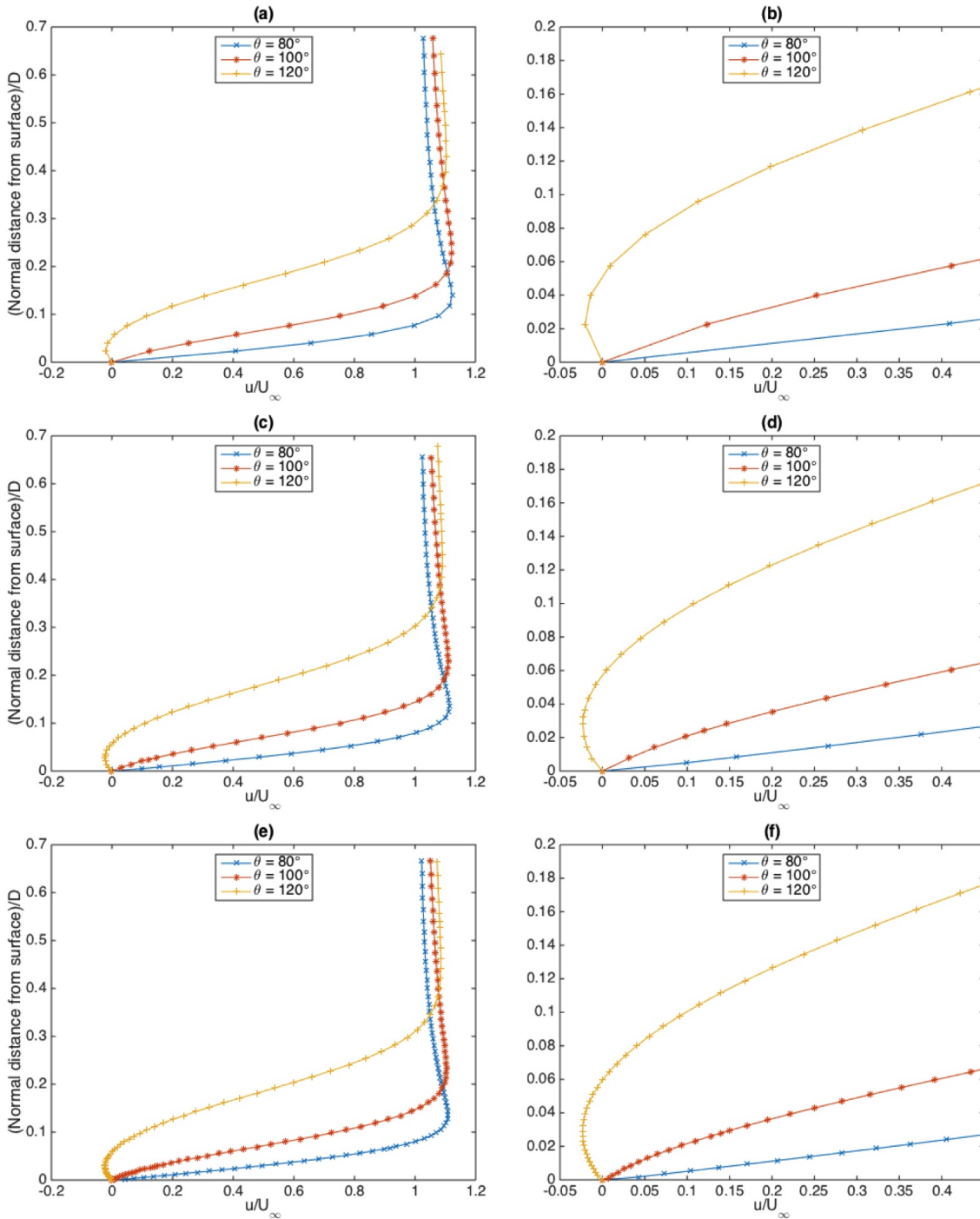
Figure 5.3: Velocity profiles in the boundary layer. The left images show velocity profiles up to a normal distance of 0.7D from the surface, whereas the right images show the inner 0.2D. The dots on the dotted lines, represent cell centres. (a,b) *very coarse*; (c,d) *medium*; (e,f) *very fine*.
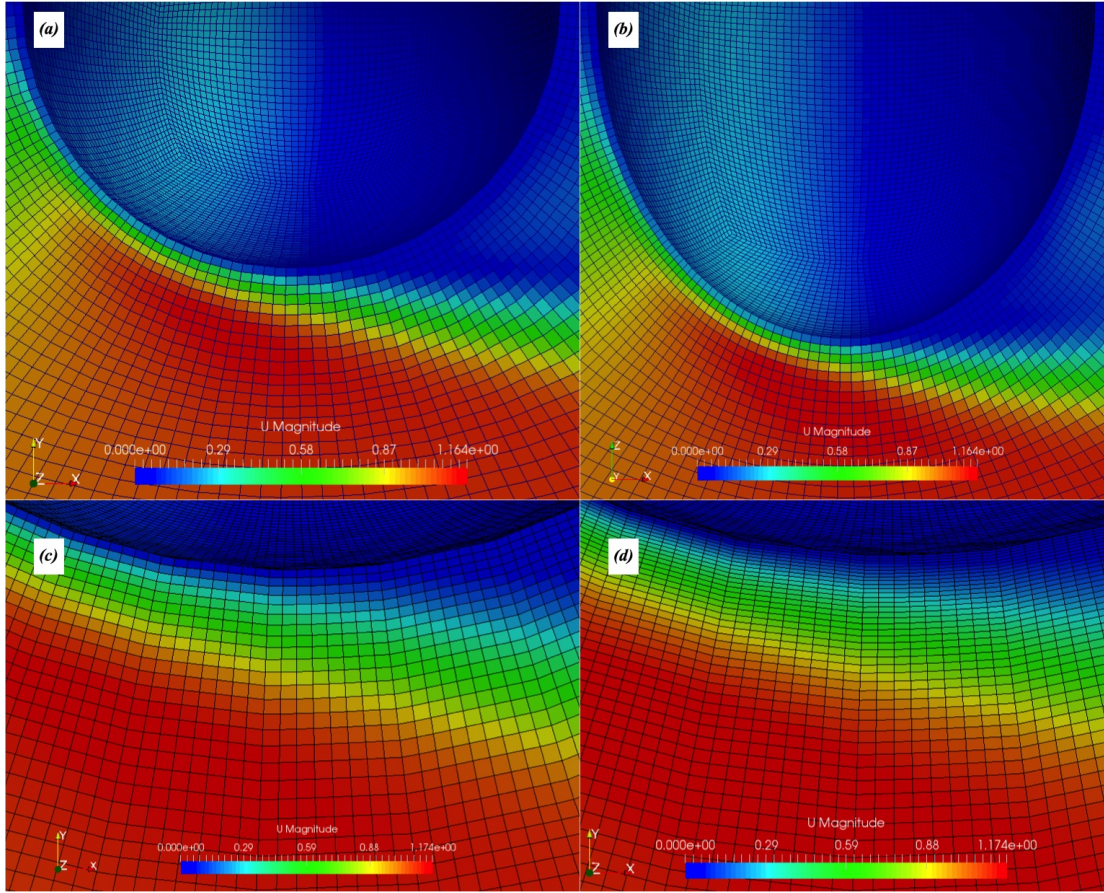
Figure 5.4: Magnitude of the flow velocity plotted along with the mesh. (a) (x,y)-plane, *very coarse* grid; (b) (x,z)-plane, *very coarse* grid. (c) (x,y)-plane, *medium* grid; (d) (x,y)-plane, *very fine* grid.

normal to the surface within the *inner block*, seem to resolve the boundary layer sufficiently.

The details of the flow separation are inspected by plotting the non-smoothed velocity field on top of the grid, shown in figure 5.4. For the *very coarse* grid in figure 5.4(a,b), the velocity magnitude increases from zero (dark blue) to U_∞ (red), over approximately 5 cells, at the separation region. An average velocity jump of 0.2 m/s between neighbouring cells, is considered too coarse. For the *medium* and *very fine* grids, the same velocity increase takes place over 12 and 25 cells, respectively, shown in figure 5.4(c,d). Thus, an average velocity jump of about 0.08 m/s and 0.04 m/s, is obtained for the *medium* and *very fine* grids.

Based on the results of the different boundary layer refinements, regarding C_D', C_D^{max}, p' and St, every grid fails to converge for a strict convergence criterion of 1%. However, if a less rigorous criterion of 3% is applied, the *fine* and *very fine* grids are assumed to be converged for the parameters mentioned above. By studying the velocity changes in the boundary layer, a sufficient grid refinement was indicated for the *medium* and *very fine* grids. Hence, it is suggested to apply the *fine* grid resolution in the continuous parts of the grid dependency study.

In figure 5.5, pressure contours in the near-wake region are plotted for the *fine* grid
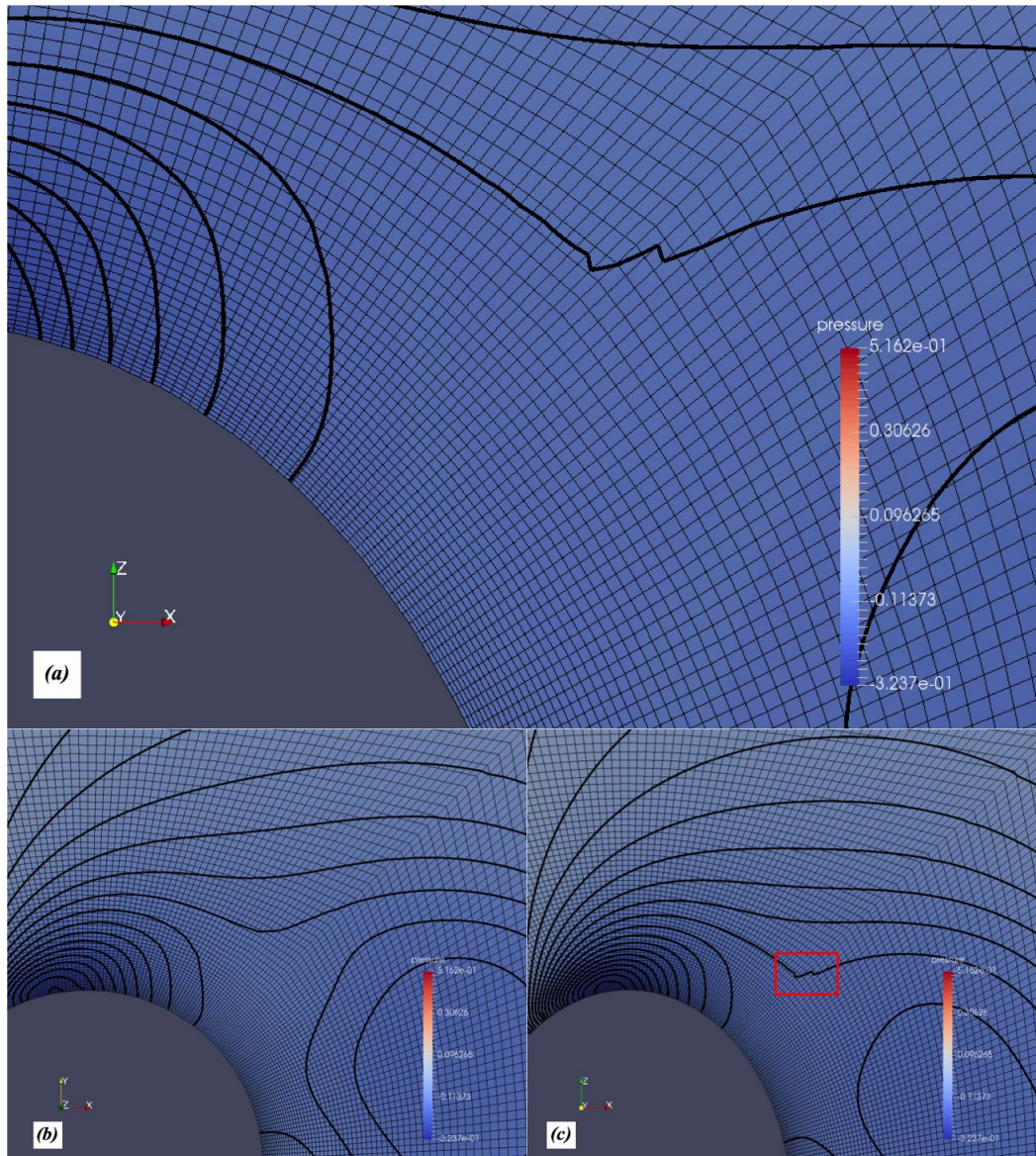
Figure 5.5: Pressure contours in the near-wake region, plotted along with the grid. (a) zoomed view of the (x,z)-plane; (b) (x,y)-plane; (c) (x,z)-plane with the pressure defect marked by the red rectangle.

resolution. The coloring represents the computed pressure magnitude, with the color bar covering the entire measured pressure range. For a sufficiently refined grid, the pressure is supposed to vary smoothly. A sudden pressure jump is not realistic and may indicate areas of bad grid quality. A minor pressure defect was observed for the contours in the (x,z)-plane, indicated by the red rectangle in figure 5.5(c). By the zoomed view of figure 5.5(a), it is clear that the pressure jump occurs between the most skewed cells of the *transition block*. However, none of the remaining contour lines in the same plane, reveals a pressure defect. Additionally, the pressure seems to vary smoothly in the (x,y)-plane, as shown in figure 5.5(b). Therefore, the observed pressure jump is not expected to influence the solution severely.

5.1.2 Domain Size

The extent of the computational domain is known to have a significant effect on the results of the simulations. E.g., if the domain is set too small, reversed flow from the outlet or blocking effects from the side walls, may pollute the results. However, by increasing the domain size, the computation time may increase considerably. Hence, the CFD operator has to compromise between domain size and quality of the results.

Table 5.3: The different domain sizes.

Mesh	Domain size (a)	Number of cells along line #				Number of cells
		K	L	M	N	
Smallest	6D	30	30	30	100	8 907 000
Small	8D	40	40	40	120	12 206 000
Big	10D	50	50	50	140	15 303 000
Biggest	12D	60	60	60	160	19 104 000

To determine a sufficient domain size, simulations were run for four different grids, including the original grid used to assess the boundary layer refinement. The domain sizes, $a = 6D$, $8D$, $10D$ and $12D$, were applied for the *smallest, small, big* and *biggest* grid, respectively. The details of each domain, are given in table 5.3. The minimum distance from the spheroid surface to the domain boundary varies from $5.3D$ for *smallest*, and increases by steps of $2D$, up to $11.3D$ for the *biggest* domain. Simultaneously, the downstream extent of the domain is increased from $18D$, up to $36D$ for the largest domain. The expected flow disturbances at the boundaries may be approximated, according to the decay rate of disturbances around a sphere, applied in Tomboulides and Orszag (2000), of $1/r^3$. Thus, the velocity at the domain boundary is expected to differ from 0.66% to 0.069%, from the free-stream velocity, for the smallest to the largest grid. To maintain a proper cell transition between the *transition block*, and the outer blocks, the number of elements along *K, L, M* and *N*, was increased for the enlarged domain sizes. The cell configuration of the *inner* and *transition block*, was kept constant and equal to the *fine* grid, specified in the previous section.

The results from varying the domain size, regarding drag and lift coefficient, pressure and Strouhal number, are shown in figure 5.6 and table 5.4. In figure 5.6 the results are plotted over the parameter *a*, defining the domain size. It is seen that none of the resulting
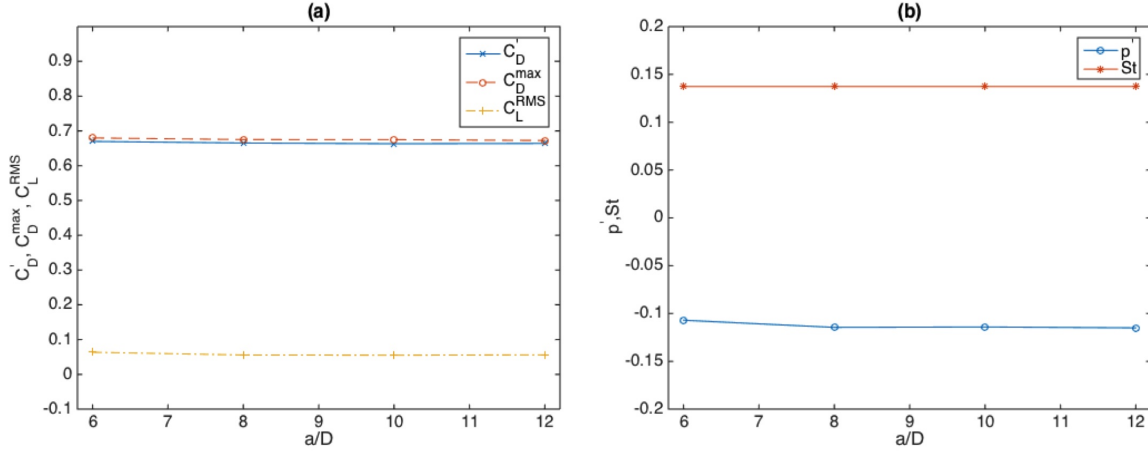
Figure 5.6: Results for varying domain size. Domain size defined by a. (a) Mean drag coefficient, maximum drag coefficient and RMS of lift coefficient; (b) mean probed pressure and Strouhal number.

Table 5.4: Percentage change in results for successive domain sizes.

Successive grids	Percentage change				
	$\Delta C_D'$	ΔC_D^{max}	ΔC_L^{RMS}	$\Delta p'$	ΔSt
Smallest → small	-0.69	-0.69	-12.42	-7.01	0.00
Small → Big	-0.29	-0.04	-1.08	0.35	0.00
Big → biggest	0.12	-0.36	1.45	-0.79	0.00

parameters, seems to change considerably between any of the different domain sizes. However, in table 5.4, relatively large changes are seen for C_L^{RMS}, due to its low magnitude. Between the *smallest* and *small* grids, an absolute change of 0.0079, causes a relative change ΔC_L^{RMS} = -12.42%. Therefore, the lift coefficient was neglected when choosing an appropriate domain size. For the remaining parameters, the biggest relative change is seen for the mean pressure, sampled at the downstream probe locations. Between the two smallest domains, an absolute change of 0.0075, and a relative difference $\Delta p' = $ -7.01 % is seen. However, between the three bigger grids, a maximum change $\Delta p' = $ -0.79%, is found. The Strouhal number obtained from the transverse velocity at *probe 7* is constant for all domain sizes and equal to $St = $ 0.1373.

To further assess the different domain sizes, the pressure and normal velocity component close to the domain boundaries, are investigated. As specified in section 4.3.3, the transverse and spanwise sides of the domain are given slip conditions. Hence, the normal component of the velocity relative to the boundary patch is set to zero. Similarly, at the downstream boundary, the magnitude of the pressure is set to $p = 0$. Since the particular parameters are set to specific values at the boundaries, discontinuities might occur if the domain is set too small.

To investigate the flow disturbances at the domain boundaries, pressure and velocity are sampled along lines consisting of 50 uniformly distributed points. Velocity profiles are
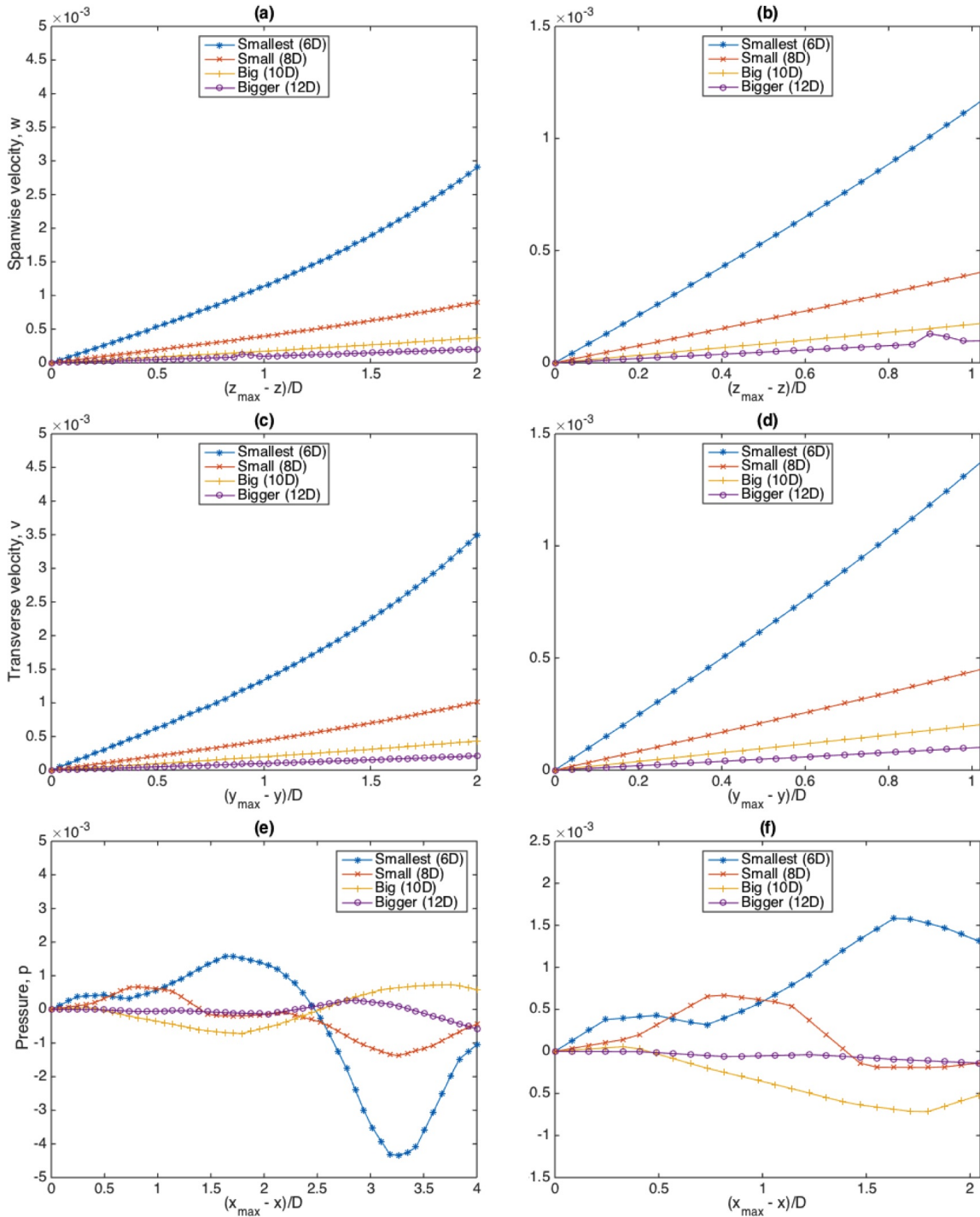
Figure 5.7: Velocity and pressure profiles at the domain boundaries. The right images show a zoomed view of the corresponding left image. (a,b) normal velocity close to *top* boundary; (c,d) normal velocity close to *front* boundary; (e,f) pressure close to *outlet* boundary.

probed at lines extending $2D$ from the border along the y and z-axis, at $x = 0$. Which is directly beside and above the prolate spheroid, where the distance from its surface to the domain boundaries is smallest. The pressure was sampled along a line, prolonged $4D$ from the downstream boundary along the x-axis, at $y = z = 0$.

Results for the four different domain sizes, $a = 6D$, $8D$, $10D$ and $12D$ are plotted in figure 5.7. The left images of the figure show the appropriate velocity component and pressure plotted over the entire sample, whereas the right images are zoomed in on the values closest to the boundary. The parameters x_{end}, y_{end} and z_{end}, are the outer coordinates of each domain, in respective directions. All the plotted values are in the order of 10^{-3}. In figures 5.7(a-d), the normal velocity component to the associated boundary, appears to decrease smoothly towards the boundary value, at the lower left corner of each image. Even so, the *smallest* grid stands out, with a v and w-velocity of about 0.35% and 0.30% of the free-stream velocity U_∞, measured at a distance of $2D$ from the *front* and *top* boundary, respectively. However, no discontinuities for the flow fields are seen for any of the tested domain sizes. Likewise, the pressure in figures 5.7(e-f) shows bigger changes close to the downstream boundary, for the smallest grid, compared to the other. Within $4D$ from the *outlet*, an absolute change of $\Delta p \approx 6 \times 10^{-3}$ is seen for the *smallest* grid, whereas $\Delta p \approx 0.85 \times 10^{-3}$ for the *biggest*. However, no sudden changes are observed in p close to the *outlet*.

Based on the results of the different domain sizes, with regard to C_D', C_D^{max}, p' and St, the *small, big* and *biggest* grids are considered converged according to the strict convergence criterion of 1%. The velocity and pressure profiles in figure 5.7, do not indicate discontinuous flow for any of the tested domain sizes. Therefore, the *small* grid may seem to be large enough to obtain proper results. However, when visualizing the wake flow in terms of velocity and vorticity fields, the author found that the *biggest* grid is favorable, compared with the smaller domains. The vortices appearing in the wake are retained further downstream, in addition to better symmetry features for the vortical structures visualized by the λ_2-criterion, at Re = 300. Since the scope of the present study, mainly involves investigating the flow features appearing in the wake, $a = 12D$ is assumed to be the sufficient domain size.

5.1.3 Time Step

To solve the time-dependent Navier-Stokes equation, both spatial and temporal discretizations are performed. Thus, in addition to the spatial properties of the grid, the results are dependent on the time step Δt. In the present study, the time step is chosen based on the stability criterion presented in section 3.5 by equation 3.14. Hence, the CFL number should be kept lower than unity for the entire mesh, at every time step of the simulation.

The physical meaning of the criterion is that the fluid particles should not propagate more than a grid cell length, per time step. Therefore, the product of the local velocity and time step has to be lower than the associated cell length. Since the smallest grid cells are located in the *inner block*, closest to the spheroid surface, this is expected to be the region of highest CFL number. However, since the local velocities are not known before the simulations, values of Δt have to be tested, to see if the stability criterion is fulfilled or not.

In OpenFOAM, the CFL number is calculated for the entire mesh at every time step of the simulation. If the stability criterion is violated and the numerical error grows, the simulation will be terminated, automatically. Based on the author's experience, a CFL
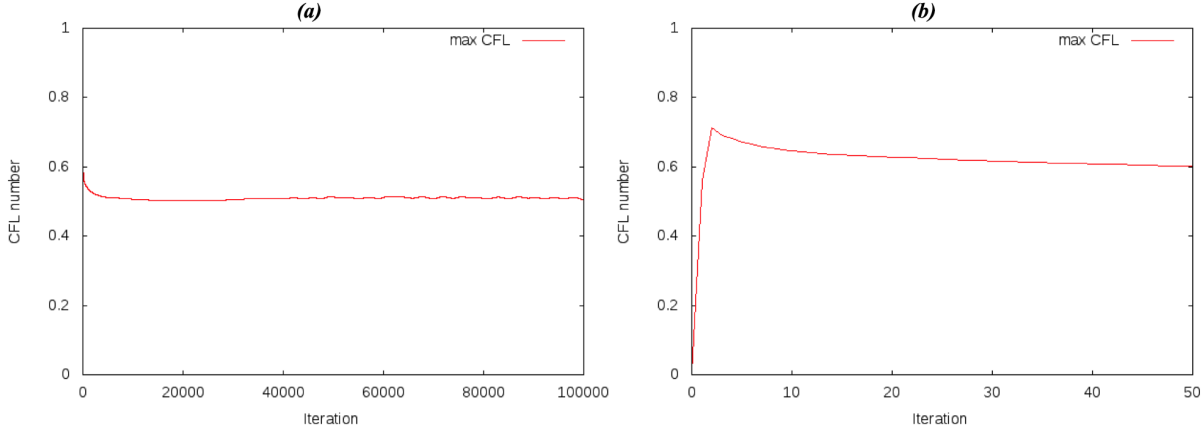
Figure 5.8: Maximum CFL number for the *fine* grid refinement and *biggest* domain size. (a) Entire simulation, 100 000 time steps; (b) the first 50 time steps.

number significantly lower than unity, and equal to about 0.5, is considered a good choice. Further reduction of Δt and CFL number, will only introduce minor changes to the results.

Figure 5.8 shows the maximum CFL number for the *fine* grid and *biggest* domain size, $a = 12D$. The results for this particular grid configuration are considered converged, based on the two previous sections. The applied time step, $\Delta t = 0.002D/U_\infty$, when assessing the grid refinement and domain size, was chosen based on the numerical study by El Khoury et al. (2012). For the entire simulation in figure 5.8(a), consisting of 100 000 time steps, the CFL number is found to stabilize at approximately 0.5. However, an increased CFL number is observed within the ten first time steps in figure 5.8(b). A maximum CFL number of 0.71 is encountered at the third time step before it gradually decreases towards 0.5. Hence, the time step, $\Delta t = 0.002D/U_\infty$, is considered adequate for the numerical method to be stable and provide accurate results.

To confirm whether the results are converged or not, an additional time step, $\Delta t = 0.001D/U_\infty$ was applied. For this Δt, the maximum CFL number stabilized at approximately 0.25, throughout the total simulated time, t $= 200D/U_\infty$. For the resulting flow parameters regarding $C_D^{'}, C_D^{max}, p^{'}$ and St, a relative percentage change below 1% was found, by comparing with the results of $\Delta t = 0.002D/U_\infty$. The RMS value of the lift coefficient showed highest relative change, $\Delta C_D^{RMS} = 2.86\%$, which satisfies the less rigorous convergence criterion of 3%. Therefore, the time step $\Delta t = 0.002D/U_\infty$, is confirmed adequate.

5.2 Final Results and Discussion

This section presents grid independent solutions for Reynolds numbers 100, 200, 250, 300 and 500. Similar to the grid dependency study, the simulations were run for a total time $t = 200D/U_\infty$, gathering statistics for the last quarter of the simulated time. An overview of the applied grid configuration is given in table 5.5. The final grid configuration is defined by the *fine* boundary layer resolution and the *biggest* domain presented in section 5.1. Resulting in a streamwise domain length of $L_x = 48D$, and transverse and spanwise length of $L_y = L_z$

$= 24D$. The number of circumferential cells in the spheroid's minor and major plane are 360 and 400, respectively. Details on the grid are given in section 5.1.

Table 5.5: Final grid configuration.

Domain size				Number of cells along line #								Number of cells
a	L_x	L_y	L_z	P	Q	R	O	K	L	M	N	
12D	48D	24D	24D	360	30	400	60	60	60	60	160	19 104 000

The results from running the *checkMesh* utility in OpenFOAM are shown in appendix C. Therefore, a maximum skewness and non-orthogonality of respectively 0.77 and 55.41° are found. The cells of lowest quality are mainly located at the corners of the *transition block*. To reduce the influence of the non-orthogonal cells, a corrector step, defined by *nNonOrthogonal-Correctors* in the *fvSolution* file is applied. A maximum aspect ratio of $\Lambda = 8.83$, are found for the cells in the outer regions of the grid. Altogether, the quality of the mesh is found sufficient. The cell quality in the regions close to the surface and near-wake is considered to be of greatest importance, due to significant flow disturbances.

5.2.1 Drag and Lift Coefficients

An overview of the resulting force coefficients is given by table 5.6. In addition to the present findings, results from comparable studies are included. Computed mean value and amplitude for both drag and lift are shown for every Reynolds number tested. The amplitude of the drag and lift coefficients are denoted ΔC_D and ΔC_L.

By comparing the mean drag coefficient at $Re = 300$ with previous studies, we see that the present results are closely related to the results of a sphere. The averaged drag of $C_D' = 0.664$ lies between the comparable values for a sphere of $C_D'^{sph} = 0.656$ and 0.683, by Johnson and Patel (1999) and Ploumhans et al. (2002), respectively. The authors report an amplitude of the drag coefficient equal to $\Delta C_D = 3.5 \times 10^{-3}$ and 2.5×10^{-3}, at the same Re. These values are the same order of magnitude as the present result, of $\Delta C_D = 9.1 \times 10^{-3}$ at $Re = 300$. The reported results for an infinite cylinder by Sumer and Fredsøe (1997), indicate a mean drag coefficient which is almost twice of the present, at $Re = 300$. For $Re = 100$ and 200, Meneghini et al. (2001), report a mean drag coefficient, which is 33.9% and 74.0%, above the present C_D' at corresponding Re.

Similar to the drag coefficient, the resulting lift coefficient of the present work compares well to the previous findings for a sphere. The magnitude of the averaged lift of 0.052, is somewhat smaller than the magnitude of the reported $C_L' = $ -0.069 and -0.061 respectively by Johnson and Patel (1999) and Ploumhans et al. (2002). The sign difference may be caused by the orientation of the shed vortices or differently oriented coordinate systems. For the lift coefficient amplitude at $Re = 300$, the present $\Delta C_L = 4.6 \times 10^{-2}$ is about three times the reported values for a sphere, of $\Delta C_L = 1.6 \times 10^{-2}$ and 1.4×10^{-2}, by Johnson and Patel (1999) and Ploumhans et al. (2002). However, compared with $\Delta C_L = 0.70$ for a cylinder at $Re = 200$ reported by Meneghini et al. (2001), all present lift amplitudes are more than one order of magnitude lower.

Table 5.6: Force coefficient results from present work and previous studies. Presented by mean value and amplitude of the lift and drag coefficient. ^{cyl} cylinder data; ^{sph} sphere data.

Author	Re	Drag coefficient		Lift coefficient	
		C_D'	ΔC_D	C_L'	ΔC_L
Present work	100	1.023	0	0	2.2×10^{-9}
	200	0.747	1.8×10^{-6}	-0.055	1.0×10^{-3}
	250	0.693	3.0×10^{-3}	0.031	1.5×10^{-2}
	300	0.664	9.1×10^{-3}	0.052	4.6×10^{-2}
	500	0.564	2.2×10^{-2}	-0.007	4.5×10^{-2}
(Meneghini et al., 2001)^{cyl}	100	1.37	-	-	-
	200	1.30	-	0	0.70
(Sumer and Fredsøe, 1997)^{cyl}	300 - 3×10^5	1.20	-	-	-
(Johnson and Patel, 1999)^{sph}	300	0.656	3.5×10^{-3}	-0.069	1.6×10^{-2}
(Ploumhans et al., 2002)^{sph}	300	0.683	2.5×10^{-3}	-0.061	1.4×10^{-2}
	500	≈0.60	-	-	-

According to experiments by Schouveiler and Provansal (2001), the critical Reynolds number for a cylinder with free hemispherical ends and aspect ratio $L_R = 1.3$, lies between $Re_c = 200$ and 250. The critical Reynolds number defines the onset of unsteady periodic flow. Even though the present study investigates a prolate spheroid, the predicted Re_c by Schouveiler and Provansal (2001) is assumed to be closely related to the present value, due to aspect ratio similarities.

To indicate the onset of unsteadiness, time series of the drag and lift coefficients as well as the corresponding force coefficient amplitudes, are plotted in figure 5.9. For the time series in figure 5.9(a) and 5.9(c), both the drag and lift coefficient start to oscillate between $Re = 200$ and 250. The oscillating behavior of the force coefficients is assessed after the flow reaches a steady state. Even though no oscillations are present for $Re = 200$, a lift amplitude of $\Delta C_L = 1\times10^{-3}$ is computed for this Reynolds number. The lift coefficient amplitude is caused by the steady descending C_L, observed in figure 5.9(c). The reason for the constant rate of decay for the computed C_L is not known to the author. Because of the small decay rate the issue was not addressed further.

Therefore, by the onset of oscillating force coefficients, the critical Reynolds number for the $L_R = 4/3$ prolate spheroid seems to lie between 200 and 250. This critical Reynolds number range coincides with the experimentally determined Re_c by Schouveiler and Provansal (2001) for a $L_R = 1.3$ finite cylinder. The onset of unsteadiness, will be further investigated by flow visualization in sections 5.2.3 and 5.2.4.

5.2.2 Separation

The separation pattern along the span of the prolate spheroid may be visualized by plotting streamlines close to its surface. In the present thesis, this was done by the OpenFOAM
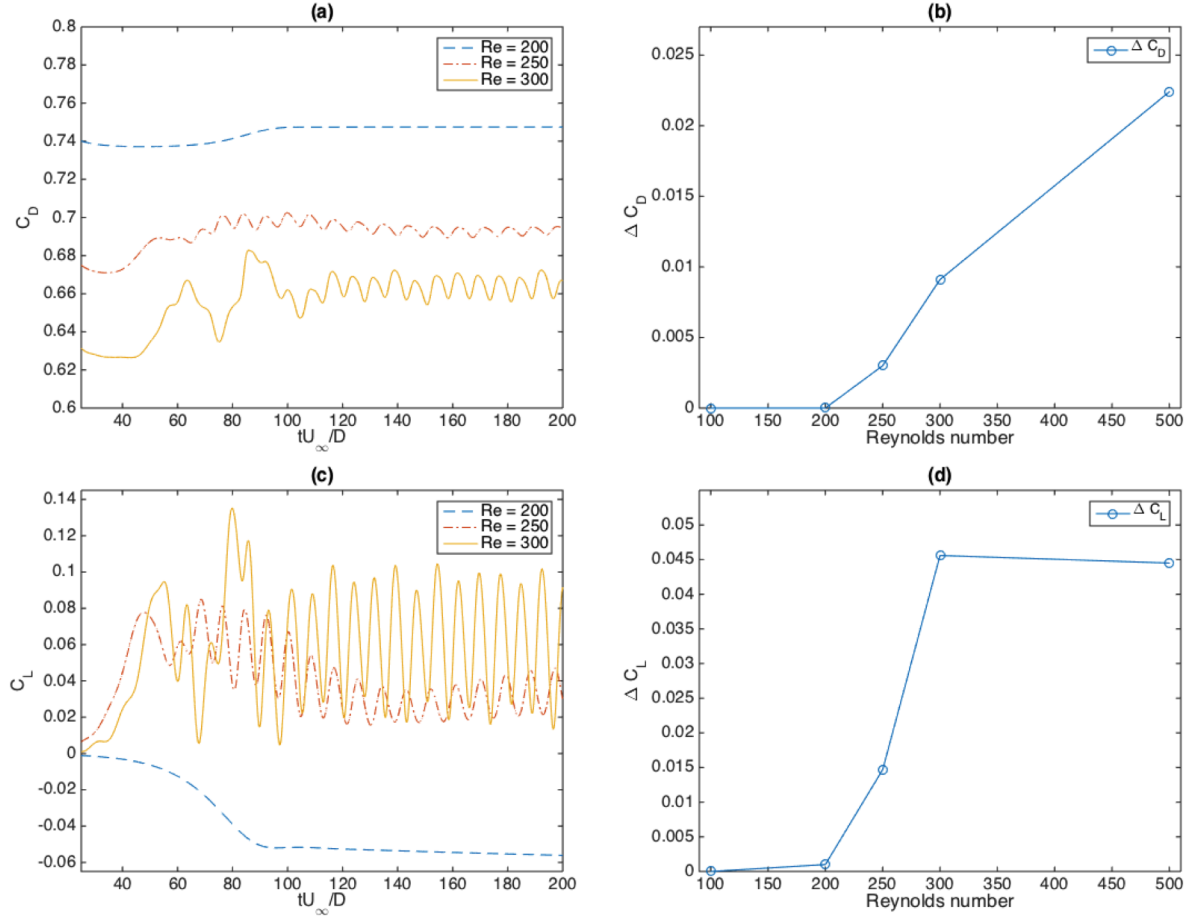
Figure 5.9: Resulting drag and lift coefficient. (a) Time series of C_D for $Re = 200$, 250 and 300; (b) drag amplitude, $\Delta C_D = (C_D^{max} - C_D^{min})/2$, for $Re = 100$ - 500; (c) Time series of C_L for $Re = 200$, 250 and 300; (b) lift amplitude $\Delta C_L = (C_L^{max} - C_L^{min})/2$, for $Re = 100$ - 500.

utility *WallBoundedStreamlines*. The streamlines are configured as shown in appendix A.4. Hence, sampled at a radial distance of $0.005\ m$ from the surface.

Instantaneous wall bounded streamlines for $Re = 100$, are shown in figure 5.10. The coloring represents the magnitude of the velocity in x-direction, near the surface. For the top and upstream view, in figure 5.10(a) and 5.10(b), it is seen that u increases from the front stagnation point, until it reaches a maximum, somewhere along the upstream half of the spheroid. As the flow reaches the downstream half of the spheroid, the flow is retarded, and the u-velocity eventually turns negative, indicating a back-flow region. The point where $u = 0$, is the separation point. Thus, by plotting several separation points along the span of the prolate spheroid, the separation pattern is revealed.

In figure 5.11, the separation pattern at $Re = 100$ is shown by plotting values of u in the range -10^{-4} to 10^{-4}, along with the streamlines. The negative signed velocity, $u \leq -10^{-4}$, is represented by blue colored streamlines, whereas $u \geq 10^{-4}$ is red. Hence, the magnitudes of u between the two limits containing $u = 0$, are found in the transition region between the red and blue colored streamlines. Therefore, the separation line is clearly illustrated, as seen
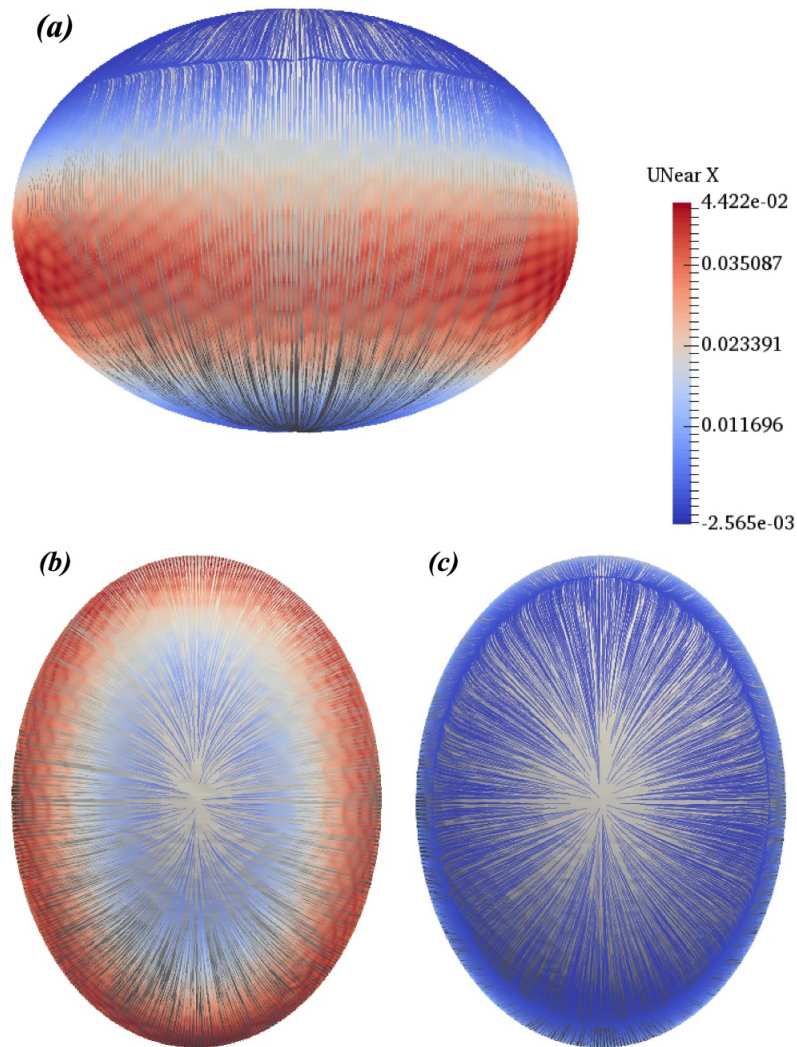
Figure 5.10: Instantaneous wall bounded streamlines at $Re = 100$. (a) top view; (b) upstream view; (c) downstream view. The coloring represents the velocity in x-direction, close to the spheroid surface.
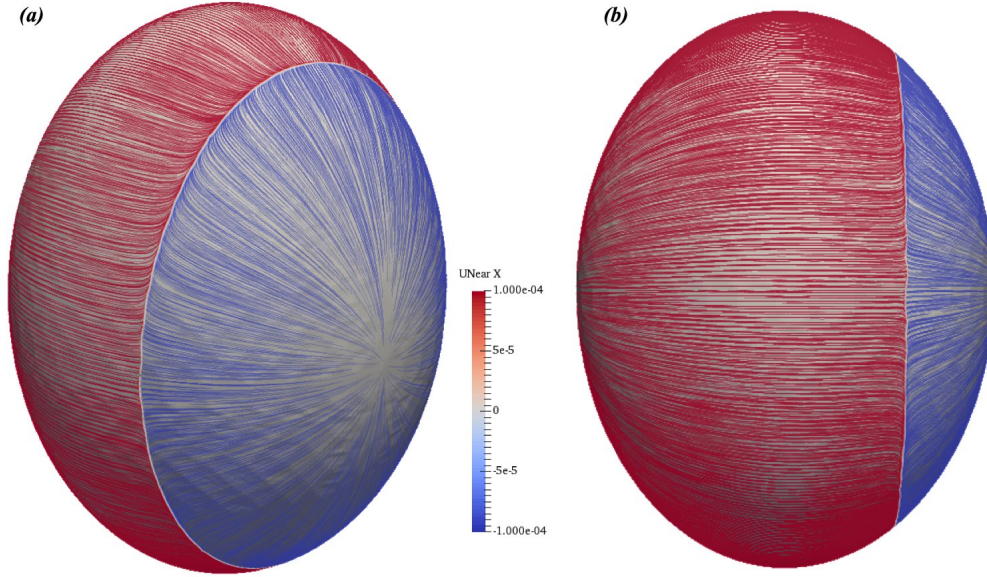
Figure 5.11: Separation line along the span of the spheroid at $Re = 100$, visualized by streamwise velocity u, close to the spheroid surface. The blue and red coloring represent $u \leq -10^{-4}$ and $u \geq 10^{-4}$, respectively. (a) perspective view; (b) side view.

in figure 5.11. By the side view in figure 5.11(b), it is evident that the separation takes place along an even line, parallel to the spheroid's major axis.

Appendix D.1 shows the resulting separation line at all tested Reynolds numbers, in a similar manner as figure 5.11(b). Therefore, the separation was found to move upstream as the Reynolds number is increased, as well as maintaining a quite even shape, parallel to the major axis, even at the highest tested Reynolds number, $Re = 500$.

Table 5.7: Resulting separation angles at $Re = 100$ - 500.

Author	Re	Separation angle, θ_s [°] (from front stagnation point)
	100	121
	200	110
Present work	250	109
	300	108
	500	103

Computed separation angles θ_s of the $L_R = 4/3$ prolate spheroid, are presented in table 5.7, and compared with previous studies in figure 5.12. The separation angle is measured from the front stagnation point, in the minor plane at $z = 0$ ($\phi = 0°$). A maximum separation angle, $\theta_s = 121°$ was found at $Re = 100$. As the Reynolds number is increased, the separation angle decreases steadily towards $\theta_s = 103°$ at $Re = 500$. A similar trend is seen for the separation around a sphere, found by Mittal (2005). The reported θ_s^{sph} plotted by the upward-pointing triangles in figure 5.12, follows an equal rate of decay as the Reynolds number is increased, as
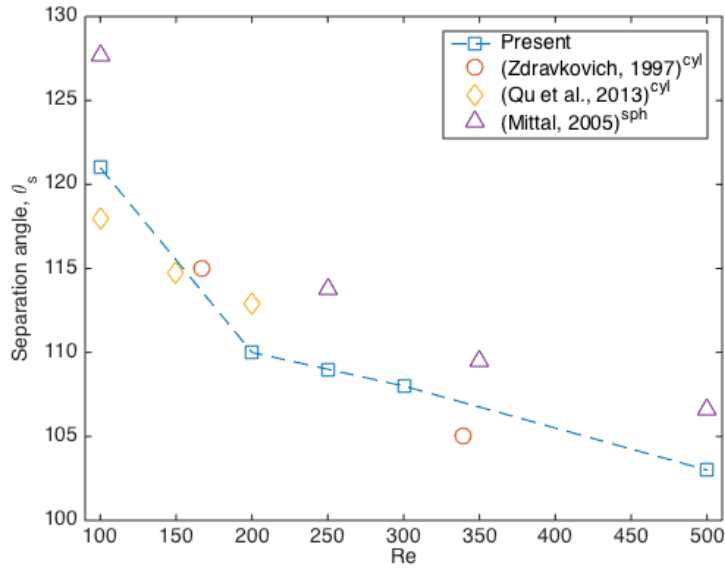
Figure 5.12: Resulting separation angle, compared with reported data for a cylinder and a sphere.

the present values. However, the flow around a sphere is found to separate at a higher angle from the front stagnation point, for all the compared Reynolds numbers. At $Re = 100$ and 500, $\theta_s^{sph} = 127.7°$ and $106.6°$ respectively, which is $6.7°$ and $3.6°$ above the corresponding θ_s of the present study.

Additionally, figure 5.12 presents the separation angle for a cylinder, suggested by Zdravkovich (1997) and Qu et al. (2013), plotted as circles and diamonds, respectively. Reported θ_s^{cyl} is in the Reynolds number range $Re = 100$ to 339. The separation angle for a cylinder θ_s^{cyl} seems to deviate less from the present results, than the results of a sphere. At $Re = 100$ and 200, $\theta_s^{cyl} = 118°$ and $112.9°$ respectively, which deviate $3°$ and $2.9°$ from the corresponding present values. The present θ_s at $Re = 300$, differs $3°$ from the reported $\theta_s^{cyl} = 105°$ at $Re = 339$.

5.2.3   Steady Flow

The flow was found to be steady for the two lowest Reynolds numbers tested, $Re = 100$ and 200. The steady flow is indicated by no force coefficient oscillations and no observed changes during a time series of the velocity in the wake. Instantaneous velocity vectors at three succeeding instants are shown in appendix D.2 and D.3 to demonstrate the steadiness. In this section, the topology of the wake flow is presented by contours of streamwise velocity and computed streamlines.

The resulting contour lines of streamwise velocity, u, in the middle (x,z)-plane, are depicted in figure 5.13. The inner contour represents $u = 0 \ m/s$, whereas $u = 0.5 \ m/s$ for the outer curve. The area encircled by the inner contour is therefore defined as the back-flow region of $u < 0$. The contour lines in figure 5.13(a) and 5.13(b), represent the exact same values, to compare the wake differences for the two Reynolds numbers. In the previous section, the separation angle at the middle (x,y)-plane at $Re = 100$ and 200, was found to
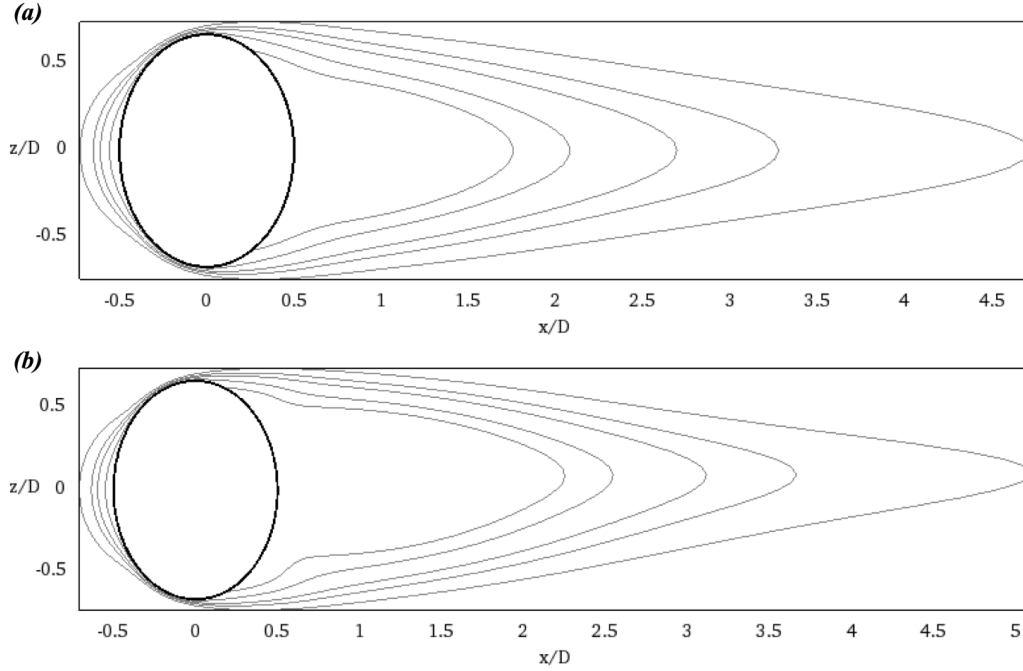
Figure 5.13: Contours of streamwise velocity, u, in the (x,z)-plane. The inner contour correspond to zero streamwise velocity, $u = 0$ m/s, and the outer to $u = 0.5$ m/s. (a) $Re = 100$; (b) $Re = 200$.

be $\theta_s = 121°$ and $110°$, respectively. A similar decreasing trend is observed in figure 5.13, by investigating the intersection point between the inner contour ($u = 0\ m/s$), and the surface of the prolate spheroid. The separation point moves upstream, toward the poles of the spheroid, $\phi = \pm 90°$, as the Reynolds number is increased. Hence, the angle ϕ_s from the front stagnation point decreases. The separation angle in the middle major plane was found to be $\phi_s = 114°$ and $106°$ at $Re = 100$ and 200, respectively.

The contours of streamwise velocity at $Re = 200$, depicted in figure 5.13(b), are stretched downstream, compared with the corresponding contours at $Re = 100$. Resulting in a longer and narrower wake region. As illustrated by the streamlines in figure 5.14, the flow is seen to separate from the spheroid surface and then rejoin at a certain distance downstream, forming a recirculation region behind the body. According to El Khoury et al. (2012), the separation length L_s is defined as the streamwise distance behind the rear end of the body to the point where the streamwise velocity changes sign from negative to positive. Hence, the zero-velocity contour in figure 5.13, outlines the local separation length along the span of the prolate spheroid. Similar to the results by El Khoury et al. (2012), the local separation length is smallest close to the poles and increases towards the mid-span. The maximum separation length was found to be $L_s = 1.26D$ and $1.75D$ for $Re = 100$ and 200, respectively. For the same Reynolds numbers, El Khoury et al. (2012) found a separation length $L_s = 4.23D$ and $3.42D$ for a $L_R = 6$ prolate spheroid. The reduced L_s as Re is increased from 100 to 200, is caused by the onset of unsteadiness at Reynolds number between 75 and 100. For a sphere, Johnson and Patel (1999) report a separation length $L_s = 0.90D$ and $1.45D$ at $Re = 100$ and 200, respectively. Therefore, by increasing the aspect ratio from $L_R = 1$ for a sphere,
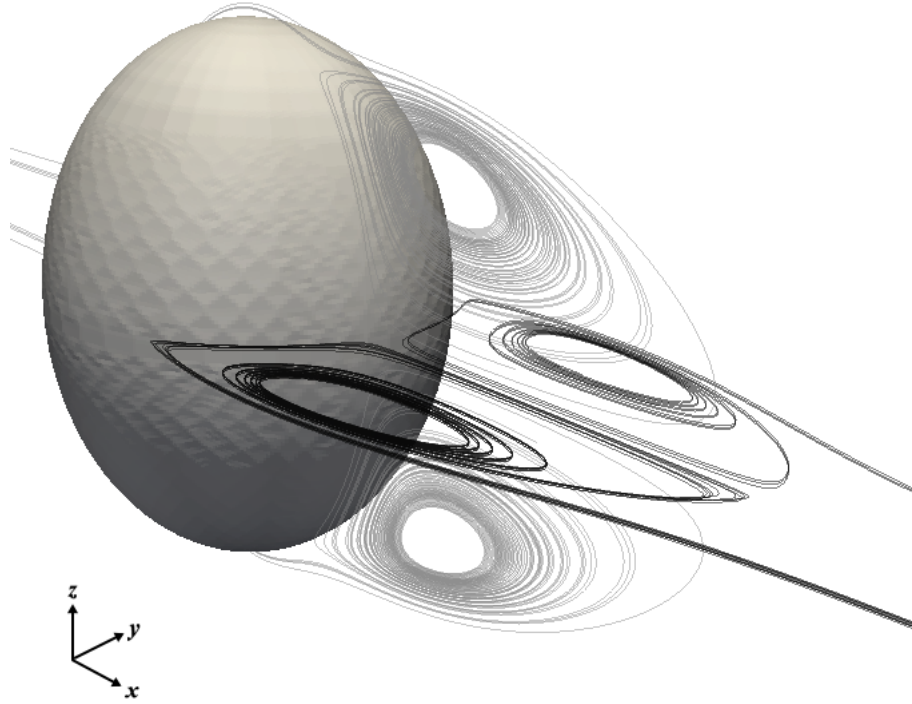
Figure 5.14: Computed streamlines at $Re = 100$. Streamlines in the major and minor plane are colored gray and black, respectively. The flow propagates in the positive x-direction.

to $L_R = 4/3$ for the present prolate spheroid, the separation length increases $0.36D$ at $Re = 100$, and $0.30D$ at $Re = 200$. The stretched separation length is caused by the asymmetrical projected area.

To illustrate the topology of the near wake flow, streamlines at $Re = 100$ are plotted in figure 5.14. The flow propagates in the positive x-direction, defined by the depicted coordinate axes. The gray and black colored streamlines are drawn in the middle major and minor plane, respectively. As illustrated by the figure, the flow is symmetric in each of the two planes, with a pair of counter-rotating vortices in each. Compared with the vortices in the minor (x,y)-plane, the vortices in the (x,z)-plane is slightly stretched. This is caused by the elliptic cross-section of the spheroid, normal to the inflow. Thus, the axisymmetry evident for a sphere at corresponding Reynolds numbers is broken. However, the wake topology of the present study is closely related to the steady and planar symmetric wake for a $L_R = 6$ prolate spheroid at $Re = 50$ and 75, in El Khoury et al. (2012).

The presence of vortices and their direction of rotation is apparent by the plotted velocity vectors in appendix D.2 at $Re = 100$ and D.3 at $Re = 200$. A pair of counter-rotating vortices in the middle (x,y) and (x,z)-plane are observed at both Reynolds numbers. At $Re = 100$, the flow is symmetric in each plane, as suggested by the streamlines of figure 5.14. However, as the Reynolds number reaches 200, the symmetry of the minor (x,y)-plane is broken. Even though the lack of symmetry, the flow is found to be steady as no changes occur for the three subsequent instants, plotted in appendix D.3.

5.2.4 Unsteady Flow

For the three highest Reynolds numbers tested, the flow was found to be unsteady. The unsteadiness is evident by oscillating lift and drag coefficient, in addition to observed changes regarding time series of flow parameters appearing in the wake of the spheroid. Time series of velocity and vorticity are presented in appendix D at $Re = 250$, 300 and 500. This section presents flow visualization results in terms of pressure contours, velocity vectors and vortex structures in the wake region.

Pressure Distribution in the Near-Wake

The pressure distribution in the near-wake of the middle (x,y) and (x,z)-plane is illustrated in figure 5.15 and 5.16, respectively. Each figure shows the resulting pressure for three different Reynolds numbers, at an arbitrary time after the flow has reached a steady state. The regions of lowest pressure are colored dark blue, whereas the maximum pressure areas are dark red. Contour lines of constant pressure are drawn by steps of 0.05, in addition to contours at $p = \pm 0.01$, ± 0.02, ± 0.03 and ± 0.04.

A distinct pressure maximum is observed close to the surface at the upstream half of the spheroid, for all Re. The pressure maxima are caused by the decelerated flow and reveal the location of the front stagnation point, aligned with the center of the prolate spheroid, $y = z = 0$.

Further downstream, along with the surface of the spheroid, a minimum pressure point is observed at each side in the minor plane, and close to each pole in the major plane. The pressure minima in figure 5.15, seem to coincide with the regions of accelerated flow around a circular cylinder, as described in section 1.1.2, suggested by Zdravkovich (1997).

Since the pressure difference between neighboring contour lines in figure 5.15 and 5.16 are equal, it is possible to compare the pressure gradient by the distance between the contours. Thus, for the upstream part of the flow $-1.5 < x/D < 0$, the pressure is seen to change equally for $Re = 250$, 300 and 500. However, in the wake, for $x/D > 0$, both the pressure magnitude and gradient are significantly changed for the three different Reynolds numbers. The figures show that the regions of rapidly changing pressure, grow for increasing Re. Additionally, the rate of change increases, seen by a reduced spacing between the contour lines. Therefore, the resulting pressure distribution indicates an increased degree of chaotic flow for the highest tested Reynolds number $Re = 500$.

For $Re = 300$ in figure 5.16(b), the pressure contours show a clear symmetry about $z = 0$, in the middle (x,z)-plane. Consisting of a pressure minima pair located at $x/D \approx 1$. The symmetry features in the major plane are comparable to the observations in the wake of a $L_R = 6$ prolate spheroid at $Re = 100$. A similar pressure minima pair was observed by El Khoury et al. (2012), in the very-near wake, caused by a pair of counter-rotating vortices. It is therefore assumed that the present pressure minima of figure 5.16(b) correspond to a similar pair of vortices. The symmetry features of the wake will be further investigated in subsequent sections.
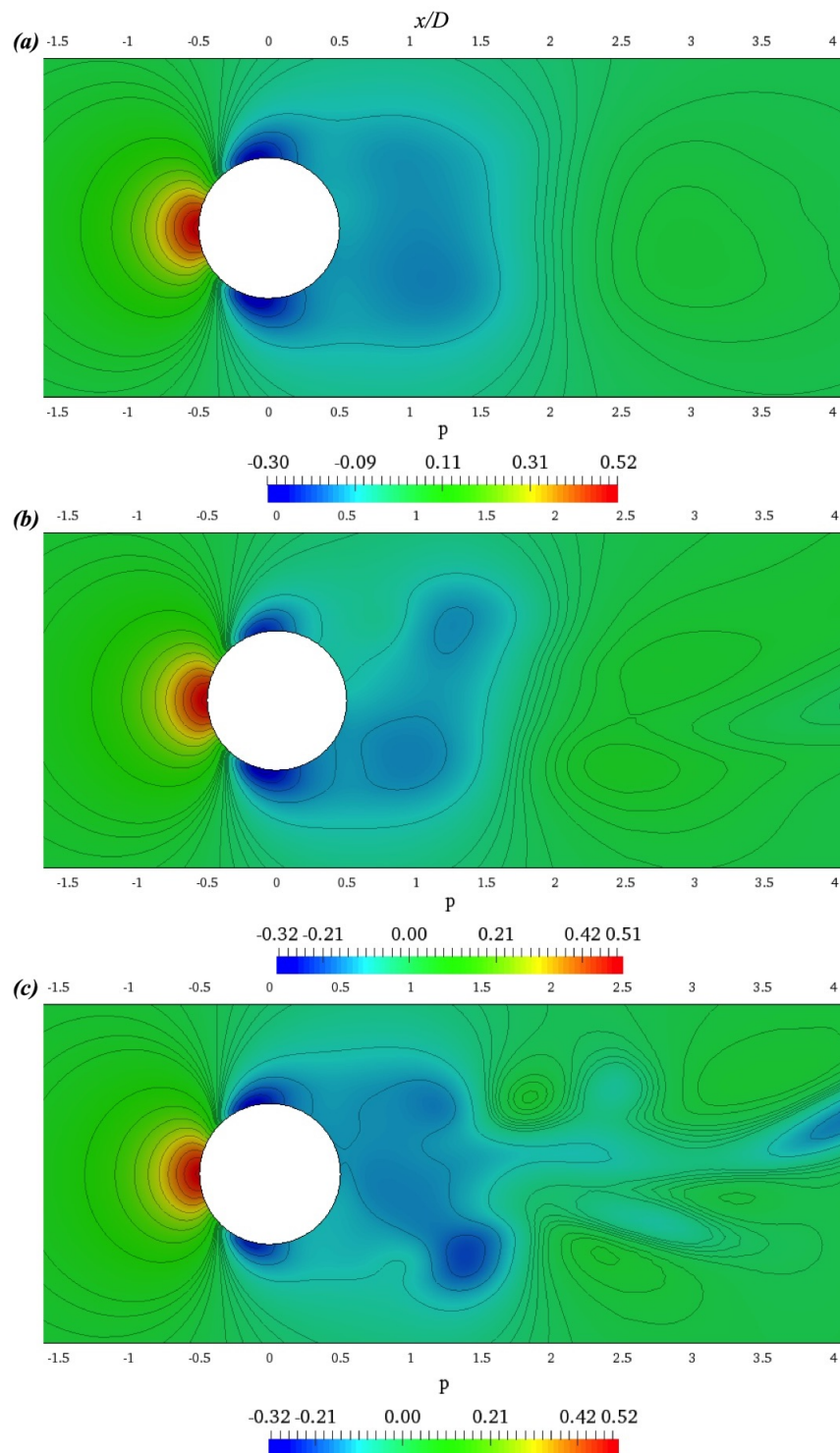
Figure 5.15: Instantaneous pressure contours in the middle (x,y)-plane. Levels are by steps of 0.05, in addition to contours at $p = \pm 0.01$, ± 0.02, ± 0.03 and ± 0.04. (a) $Re = 250$; (b) $Re = 300$; (c) $Re = 500$.
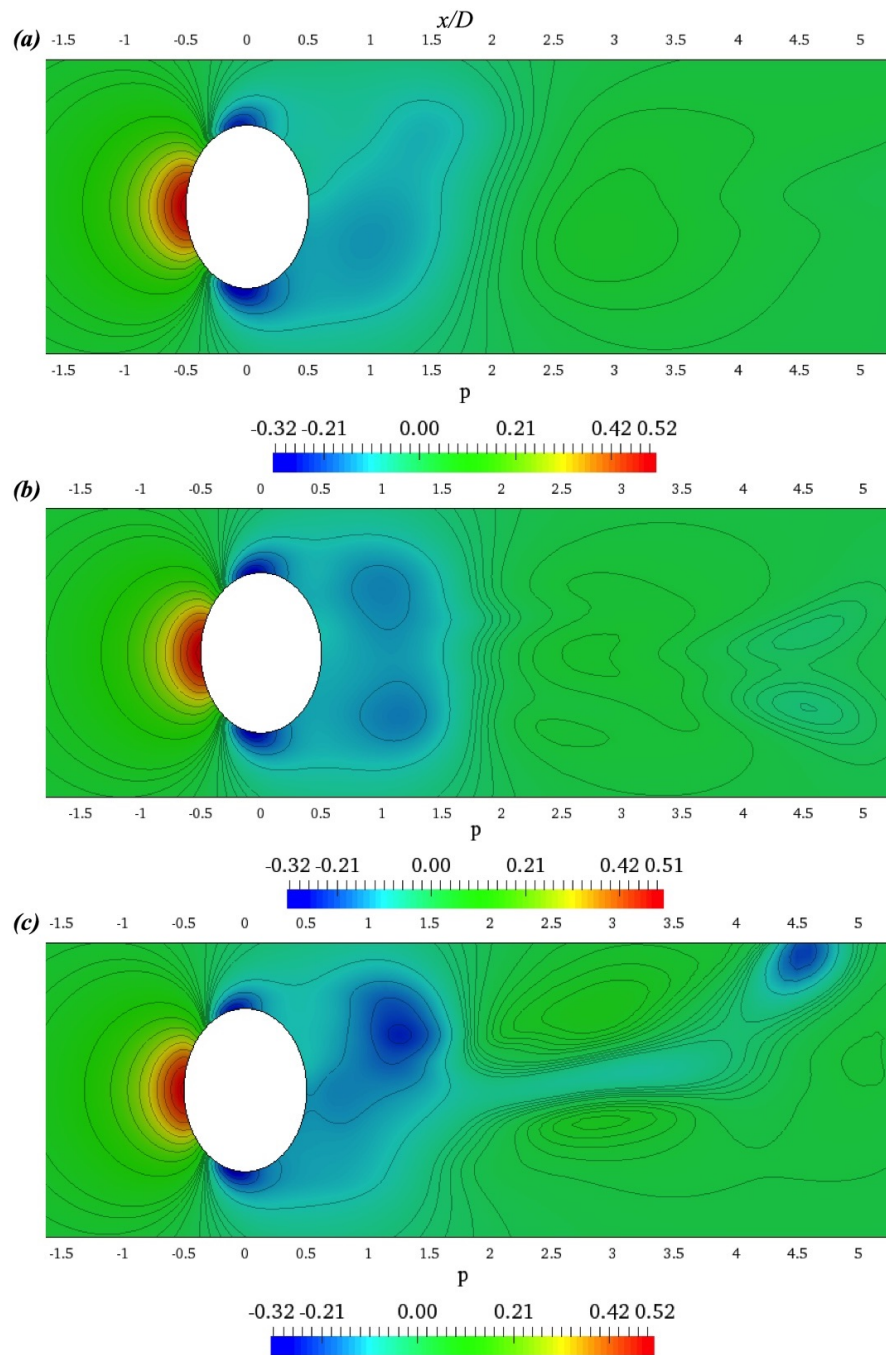
Figure 5.16: Instantaneous pressure contours in the middle (x,z)-plane. Levels are by steps of 0.05, in addition to contours at $p = \pm 0.01$, ± 0.02, ± 0.03 and ± 0.04. (a) $Re = 250$; (b) $Re = 300$; (c) $Re = 500$.

Velocity Field in the Near-Wake

Figure 5.17 shows the resulting instantaneous velocity vectors in the middle (x,y) and (x,z)-plane for three different Reynolds numbers. The vectors are scaled and colored according to the velocity magnitude. Dark blue corresponds to zero fluid motion, and dark red to 1.16 m/s, which is somewhat higher than the inlet velocity, $U_\infty = 1 \; m/s$.

Regions of accelerated flow are located close to the sides $\theta = \pm 90°$ and poles $\phi = \pm 90°$ of the spheroid in the (x,y) and (x,z)-plane, respectively. From $x/D \approx 0$ onward, a band of accelerated and displaced flow seems to embed the decelerated wake region. The dark red velocity vectors continue downstream, to $x/D \approx 2$, for all Re.

By studying the direction of the velocity vectors, it is seen that regions of circulating flow, or vortices, appear in the near-wake. These areas are indicated by arrows forming closed rings. For both the major and minor plane in figure 5.17 the upper vortex rotates clockwise, whereas the lower rotates counterclockwise at all Re. Thus, the vortex rotates in the same direction as the vorticity of the associated boundary layer.

All images of figure 5.17 are captured at the same instant as the pressure distribution in the previous section. Thus, the relationship between the pressure and velocity field may be found by comparing the corresponding figures. Thereof, the location of each vortex center seems to coincide with a pressure minimum. These pressure minima are easiest to observe for $Re = 300$ and 500, in figures 5.15(b,c) and 5.16(b,c), shown by blue regions encircled by contour lines forming closed circles. For instance, in figure 5.15(b), two regions of minimum pressure are located approximately at $x/D = 1$ and 1.5, indicating that one of the two vortices is shed and has started to propagate downstream. The corresponding velocity field in figure 5.17(c) clearly shows a pair of vortices in the near-wake, with its center points coinciding with each pressure minimum of figure 5.15(b).

To demonstrate temporal changes in the near-wake flow, time series of the velocity at $Re = 250$, 300 and 500 are shown in appendix D.4, D.6 and D.8, respectively. For each Reynolds number, the velocity vectors are presented in the middle (x,y) and (x,z)-plane at five subsequent instants. A constant time step $\Delta t = 1.82D/U_\infty$ is applied. The time difference between each picture equals one quarter of the shedding period at $Re = 300$. Thus, the periodic flow at $Re = 300$ is demonstrated, since the first and last picture of the time series in appendix D.6 are identical. Between the first and last instant, a vortex in the upper part of the minor plane is shed and a new vortex is formed in the near-wake as seen in appendix D.6.

In figure 5.18, the shape of the wake is visualized by plotting the streamwise velocity, u, in cross-sectional slices. The slices are located at three downstream locations, $x/D = 1$, 4 and 7. The coloring defines the magnitude of u. Dark blue areas indicate $u \leq 0.8$ m/s, and dark red $u \geq 1.0$ m/s. Thus, the region of significantly disturbed flow is shaped by the transition from blue to red. This way of visualizing the wake is inspired by El Khoury et al. (2012), who revealed the axis switching phenomenon for a $L_R = 6$ prolate spheroid, in a similar fashion. The present results, depicted in figure 5.18 show that the shape of the wake at $x/D = 1$ resembles the projected area of the prolate spheroid for all Re. However, at x/D = 4 and 7, the outline of the wake is clearly changed. For the lowest Reynolds number $Re =$ 250 in figure 5.18(b), the wake seems to loose its antisymmetric shape and attains a circular cross-section at the two rightmost slices. Unlike $Re = 250$, the shape of the wake at $Re =$
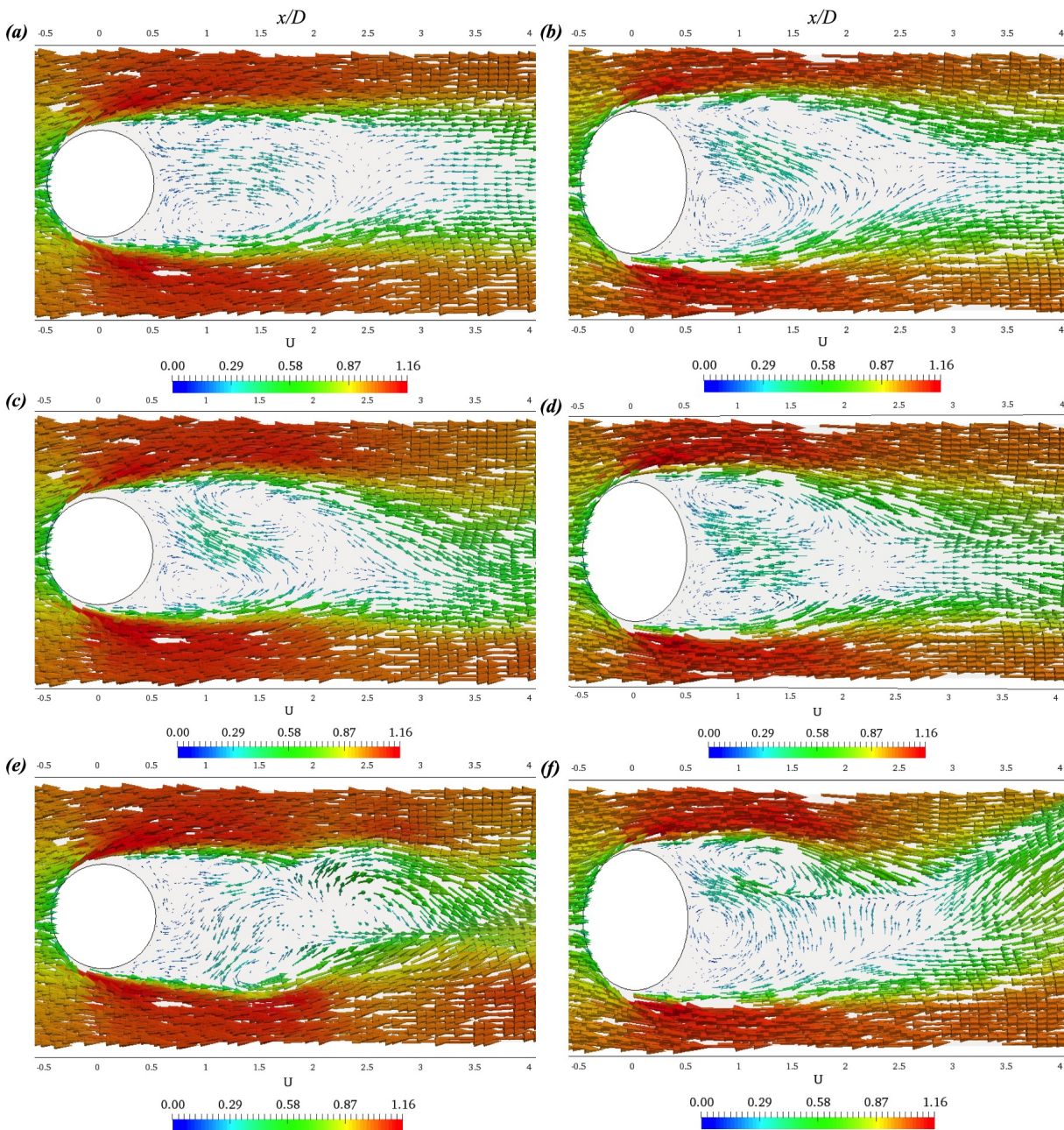
Figure 5.17: Instantaneous velocity vectors in the middle (x,y)-plane (left images) and middle (x,z)-plane (right images). The vectors are colored according to the velocity magnitude, defined by the associated color bar. (a,b) $Re = 250$; (c,d) $Re = 300$; (e,f) $Re = 500$.
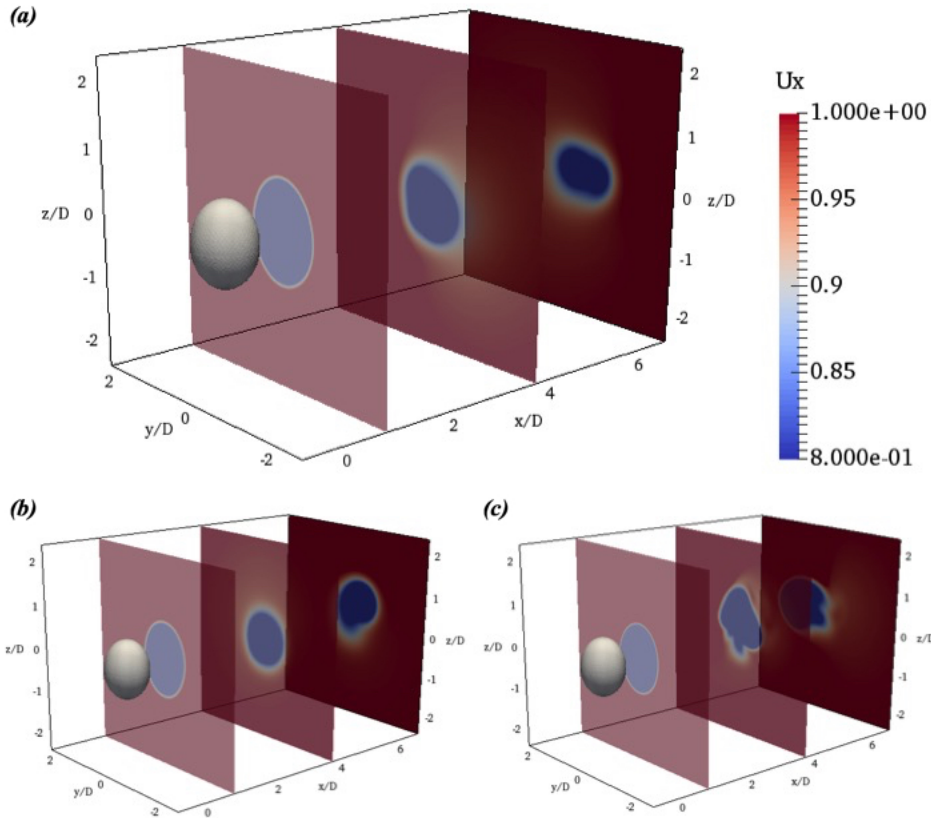
Figure 5.18: Plots of instantaneous streamwise velocity u. The velocity fields are shown by cross-sectional slices at three downstream locations $x/D = 1$, 4 and 7. (a) $Re = 300$; (b) $Re = 250$; (c) $Re = 500$.

300 and 500 maintain its antisymmetry. However, at $x/D = 7$ the major axis of the wake is rotated 90° relative to the major axis of the spheroid. Therefore, an axis switching seems to occur somewhere between $x/D = 4$ and $x/D = 7$. A Similar axis switching was found in the wake of elliptical disks with aspect ratio $L_R = 3$ at $Re = 200$, by Kiya and Abe (1999). The authors suggest that the axis switching is caused by the vortex shedding. The observed hairpin-shaped vortices had a greater growth rate in the minor plane compared with the major. The reason for the present axis switching is investigated in the following section by visualizing the vortex structures in the wake.

Vorticity and Vortical Structures of the Wake

In this section, the vorticity and vortical structures of the wake are first presented at the second highest Reynolds number, $Re = 300$. Contours of the vorticity components ω_x, ω_y and ω_z are presented for both the major and minor plane, whereas the vortex structures of the wake are illustrated by isosurfaces of constant λ_2. After determining the relationship between the vorticity contours and vortical structures, the λ_2-definition is implemented for the remaining Reynolds numbers, $Re = 250$ and 500.

Figure 5.19 depicts instantaneous vorticity contours at $Re = 300$ in the middle (x,y) and

(x,z)-plane. The coloring of the figure is given by the magnitude of the respective vorticity components. Red and green denote positive and negative values, respectively. Hence, representing fluid rotating in opposite directions. Regions of local maximum or minimum vorticity are indicated by the contour lines forming closed rings.

Figures 5.19(a,b) show contours of streamwise and transverse vorticity in the middle major plane. The figures seem to confirm the symmetry features of the flow as previously suggested by the pressure distribution. The vorticity extrema are seen to emerge in pairs with a symmetry line approximately at the mid-span, $z/D = 0$. However, each pair consists of two counter-rotating vortices, indicated by the coloring.

Contours of transverse vorticity ω_z plotted in figure 5.19(c) clearly show that the planar symmetry is broken in the minor plane. Additionally, the width of the vortices in the minor plane increases quickly for $x/D > 4$. At approximately $5.5D$ downstream of the prolate spheroid, a point of maximum ω_z is located at $y/D \approx$ -1.5. Further downstream, another extremum is observed with its centre point at $x/D \approx 11$, $y/D \approx$ -2. At the opposite side of the wake, $y/D > 0$, the contour lines reach an outer point of $y/D \approx 1$, at approximately $10D$ downstream. The suggested cause of the axis switching phenomenon by Kiya and Abe (1999) of rapidly growing vortices in the minor plane, therefore seems to agree with the present results.

Time series of the vorticity components plotted in a similar fashion as shown in figure 5.19 are presented in appendix D.7. A series of five successive instants are depicted with a fixed time step equal to a quarter of the shedding period at $Re = 300$. The periodicity of the flow is evident by the contours of ω_z in the middle (x,y)-plane.

Figure 5.20 shows the resulting vortical structures in the wake at $Re = 300$ computed by the λ_2-definition. The wake is inspected by three different views. To be able to compare the wake structures with the vorticity contours, the results are visualized at the corresponding moment. The shedding of one-sided vortices is clearly illustrated by the perspective view in figure 5.20(a). At a distance downstream of the recirculating region in the near-wake, the vortex structure eventually rolls up and forms interconnected loops. These vortex structures have the characteristic shape of a hairpin. Equally shaped vortices are seen to emerge in the wake of similar bluff bodies as presented in section 1.1. One-sided and hairpin-shaped vortices was also observed by Sakamoto and Haniu (1990) and Tomboulides and Orszag (2000) in the wake of a sphere at $Re = 300$. For a prolate spheroid with $L_R = 6$, El Khoury et al. (2012) found that vortices are shed from $Re = 100$ onwards. However, in this case, the vortex loops were found to have an alternate orientation. Similar double-sided and hairpin-shaped vortices were seen in the wake of an elliptical disk with $L_R = 3$ at $Re = 200$ by Kiya and Abe (1999).

The top view in figure 5.20(c) confirms the planar symmetry in the middle (x,z)-plane, as suggested in previous sections. A corresponding plane of symmetry aligned with the major axis was reported by El Khoury et al. (2012). Even for an axisymmetric sphere, a plane of symmetry for the unsteady wake at $300 < Re < 420$ was observed in the experiments by Sakamoto and Haniu (1990).

To demonstrate the relationship between the vorticity contours and computed vortical structures, the two are combined in figure 5.21. Contours of streamwise vorticity at the middle (x,z)-plane and transverse vorticity in the middle (x,y)-plane, are shown in figure 5.21(a) and 5.21(b), respectively. In the first figure, the vorticity extrema for ω_x are seen
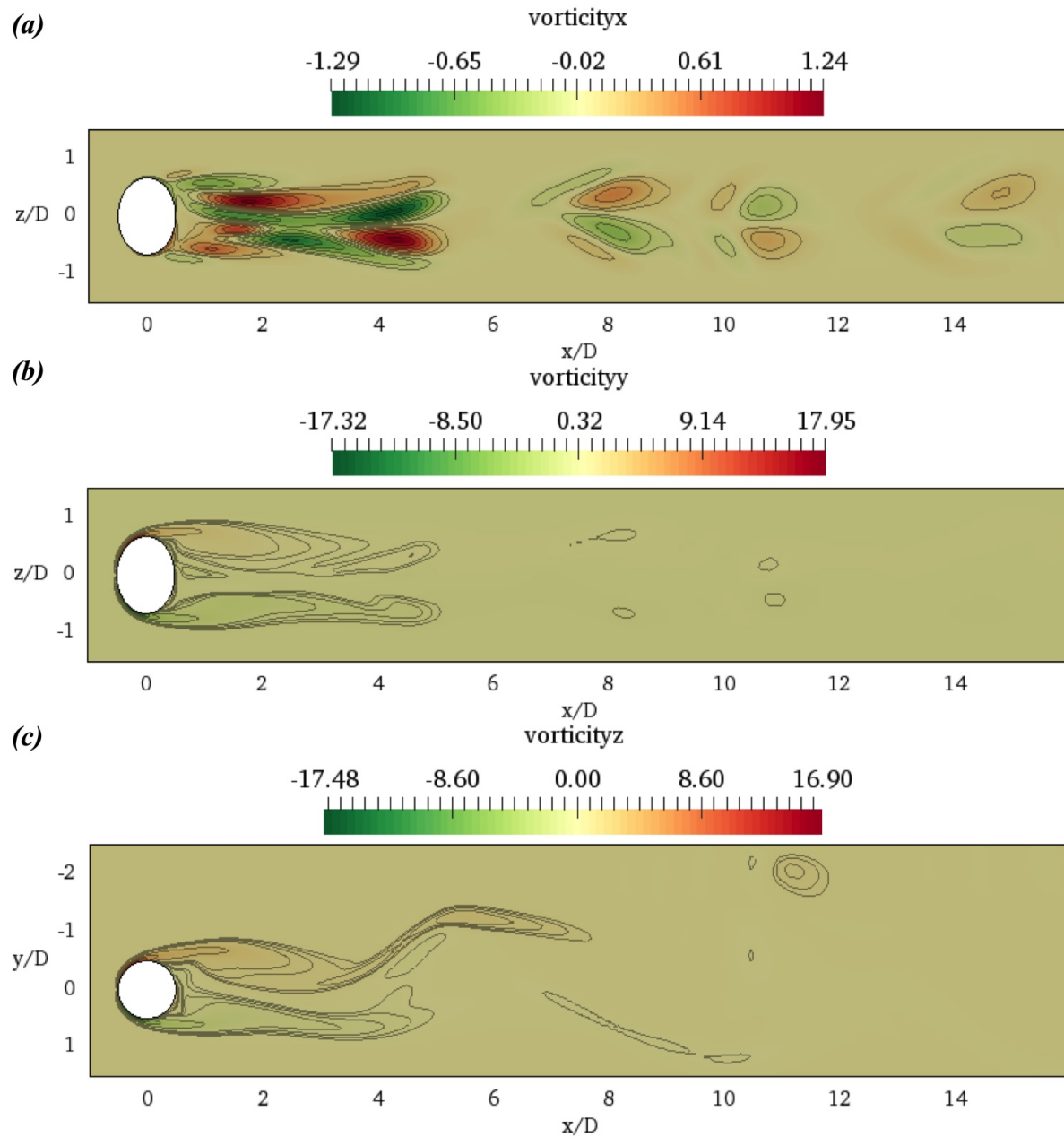
Figure 5.19: Instantaneous vorticity contours at $Re = 300$. (a) ω_x in the middle (x,z)-plane; (b) ω_y in the middle (x,z)-plane; (c) ω_z in the middle (x,y)-plane.
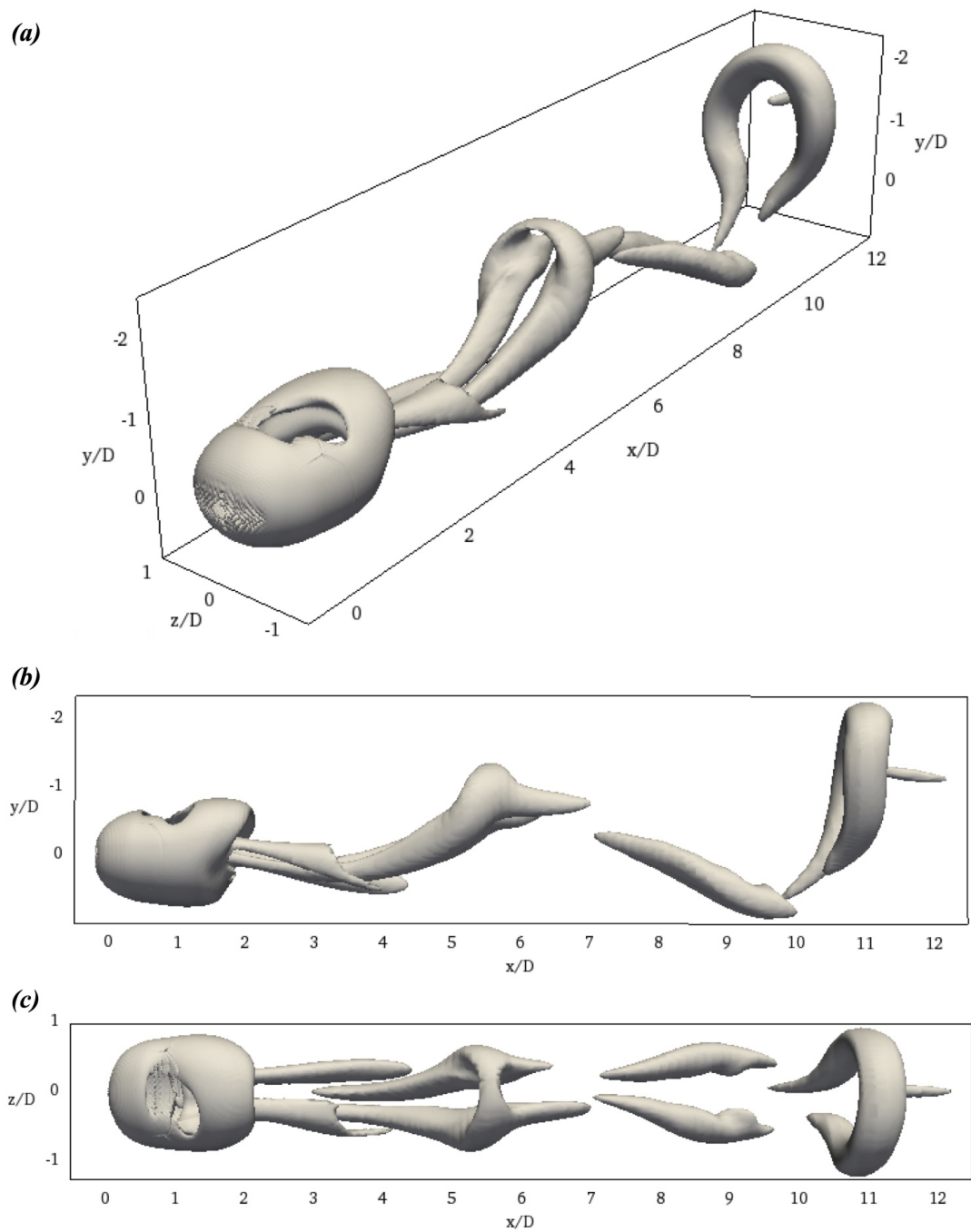
Figure 5.20: Vortical structures in the wake at $Re = 300$, visualized by the λ_2-definition. Isosurfaces are drawn for $\lambda_2 = 0.02$. (a) perspective view; (b) side view, (x,y)-plane; (c) top view (x,z)-plane.
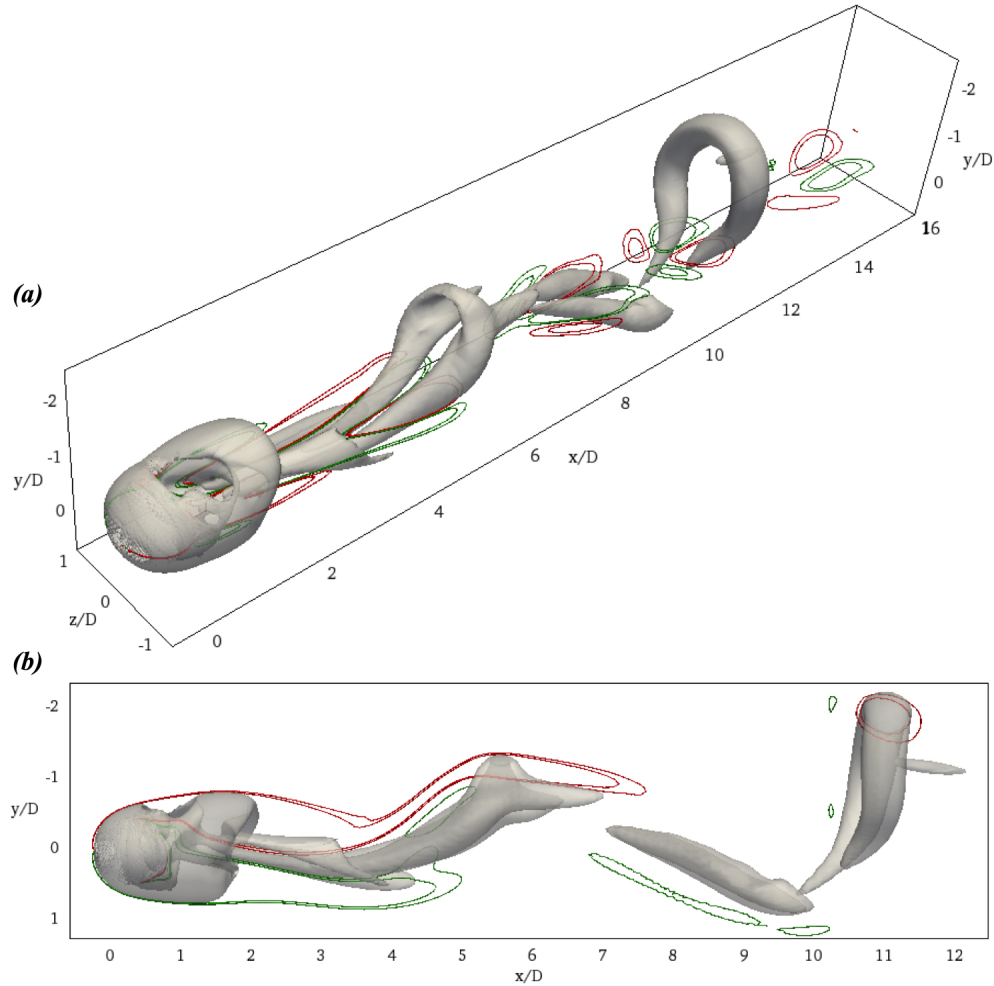
Figure 5.21: Vorticity contours plotted together with the vortical structures at $Re = 300$. Positive vorticity contours are colored red, whereas green denotes negative vorticity. (a) ω_x in the middle (x,z)-plane; (b) ω_z in the middle (x,y)-plane.

to coincide with the legs of the hairpin structures. The coloring illustrates that the swirling motion in each leg rotates in opposite directions. Similarly, in figure 5.21(b) the regions of maximum transverse vorticity overlap the top part of the two vortex loops at $x/D \approx 5.5$ and $x/D \approx 11$.

Figure 5.22 illustrates the vortical structures at the two remaining Reynolds numbers, $Re = 250$ and 500. Isosurfaces are computed for constant λ_2. For the lowest Reynolds number, the characteristic hairpin-shaped vortices as seen for $Re = 300$ are absent. Instead, a pair of counter-rotating vortices twists around each other as they propagate downstream. For comparison, Sheard et al. (2008) simulated the flow normal to a cylinder with hemispherical ends with an aspect ratio $L_R = 1.04$. Unlike the present study, the author found the wake to be steady at $Re = 250$, consisting of two counter-rotating vortices extending downstream as illustrated in figure 2.8 in section 2.3. The increased aspect ratio from $L_R = 1.04$ to $L_R = 4/3$, therefore seems to introduce a clearly higher degree of unsteadiness.

In figure 5.22(b), at the highest tested Reynolds number $Re = 500$, it is seen that the
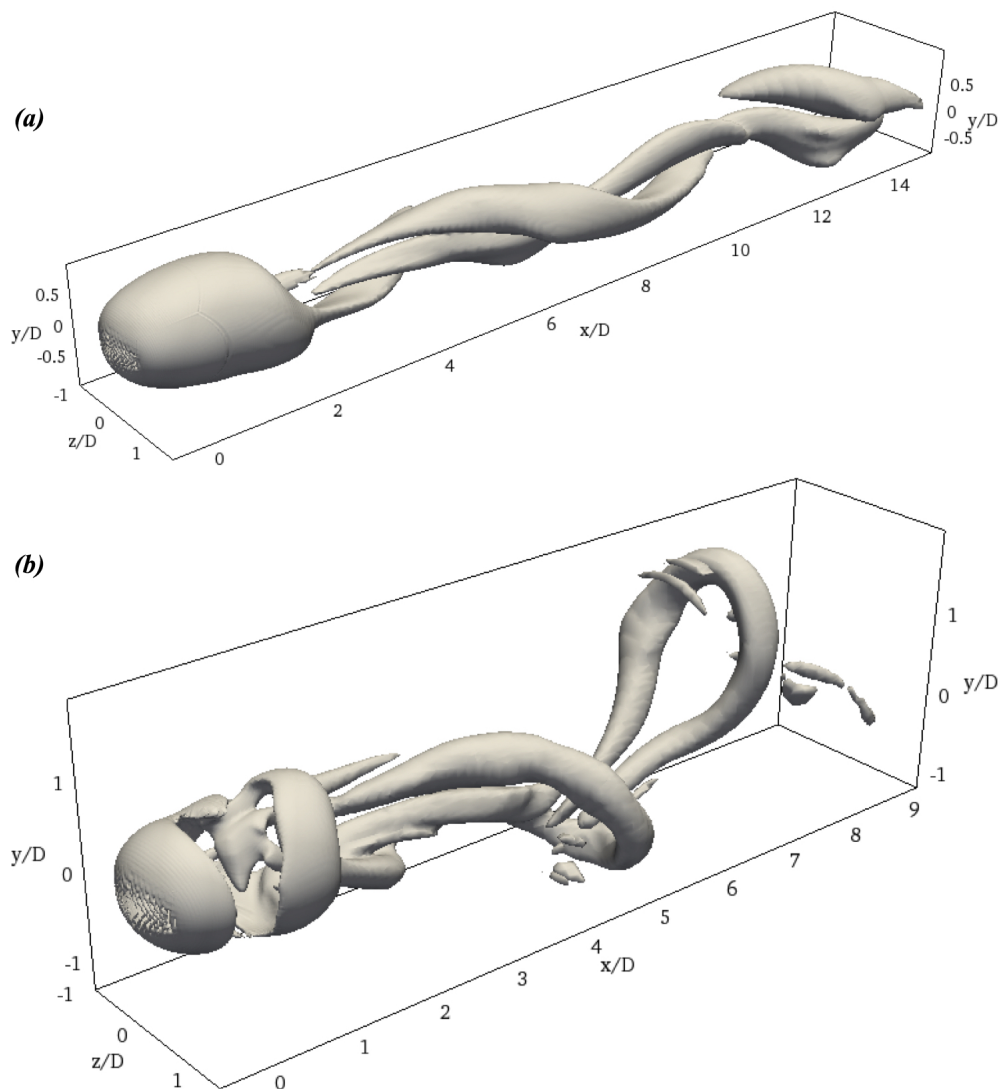
Figure 5.22: Instantaneous vortical structures in the wake visualized by the λ_2-definition. (a) $Re = 250$; (b) $Re = 500$.

vortex structures of the wake maintains the familiar hairpin-shape as observed at $Re = 300$. However, the loops are oppositely oriented, unlike the vortices of constant orientation at $Re = 300$. This wake structure is closely related to the results by El Khoury et al. (2012) for a $L_R = 6$ prolate spheroid at $Re = 100$. For a visual comparison, the vortical structures by El Khoury et al. (2012) are shown in figure 1.9 in section 1.1.4.

In a similar fashion as that of $Re = 300$, time series of the vorticity components are plotted for $Re = 250$ and 500 in appendix D.5 and D.9, respectively. The time difference $\Delta t = 1.82D/U_\infty$ between each picture is equal to the time step applied for $Re = 300$. A periodic flow behavior is suggested by a repeated pattern of vorticity at $Re = 250$. However, at $Re = 500$ the contours of vorticity in the wake seem to develop randomly and no periodicity is noticeable.

Wake Fluctuations

A frequency analysis is performed for $Re = 250$, 300 and 500 by Fourier transforming a measured time series of the transverse velocity v. The velocity was sampled at two probes located $5.75D$ downstream of the prolate spheroid centre, at $y = \pm0.3D$ and $z = 0$. Corresponding to *probe 7* and *probe 8*, defined in section 4.6. The resulting time series of v are shown in the leftmost images of figure 5.23. The vertical axis defines the y-coordinate normalized by the diameter D. The data from *probe 7* and *probe 8* is shifted $\pm0.3D$, respectively, to avoid overlapping. The curves are therefore plotted to demonstrate velocity fluctuations and possible periodicity, not magnitude. The right images of figure 5.23 show the resulting power spectra from the Fourier transformation of v at *probe 7* with the Strouhal number defined on the horizontal axis. The dominant frequencies are marked by the corresponding St.

Figure 5.23(a) and 5.23(c) indicate a periodic wake flow for $Re = 250$ and 300 by a steady and oscillating transverse velocity. Therefore, the resulting power spectra for the two Re consists of few significant peaks. At $Re = 250$, a single peak for $St = 0.107$ is shown in figure 5.23(b). At $Re = 300$, the power spectra contains a dominant peak at $St = 0.137$ which is somewhat higher than the Strouhal number at $Re = 250$. However, in this case, the presence of a second frequency $St_2 = 0.259$ is observed. As the Reynolds number reaches 500, the periodicity of the transverse velocity is clearly broken, shown in figure 5.23(e). Thereof, the resulting power spectra consists of several peaks. Although the flow at this Re is more chaotic, a dominant peak is observed for $St = 0.183$, in addition to a lower and a higher frequency of $St_1 = 0.092$ and $St_2 = 0.259$, respectively.

Compared with previously reported frequencies appearing in the wake of similar shaped bodies, the present results agree well with the results of a sphere. At $Re = 300$ Johnson and Patel (1999) found a dominant frequency at the exact same Strouhal number, $St = 0.137$. Whereas Ploumhans et al. (2002) and Tomboulides and Orszag (2000) observed slightly lower shedding frequencies of $St = 0.135$ and 0.136, respectively. By a frequency analysis of the axial velocity component, Tomboulides and Orszag (2000) discovered a pronounced peak at $St = 0.167$ at $Re = 500$. In addition, the authors discovered the existence of a lower frequency at $St = 0.045$, which is in the same order of magnitude as the present St_1 at the same Re. However, Tomboulides and Orszag (2000) did not evaluate this frequency further. The frequencies appearing in the wake of a $L_R = 6$ prolate spheroid are investigated by El Khoury et al. (2012) for $100 \le Re \le 300$. For $Re = 200$ and 300, the author found nearly identical Strouhal numbers, equal to $St = 0.149$ and 0.151, respectively. For the highest tested Reynolds number $Re = 300$, additional lower and higher frequencies were obtained, similar to the present results at $Re = 500$. El Khoury et al. (2012) suggest that the appearance of several frequencies in the wake indicates a transitional flow regime, from laminar to turbulent.
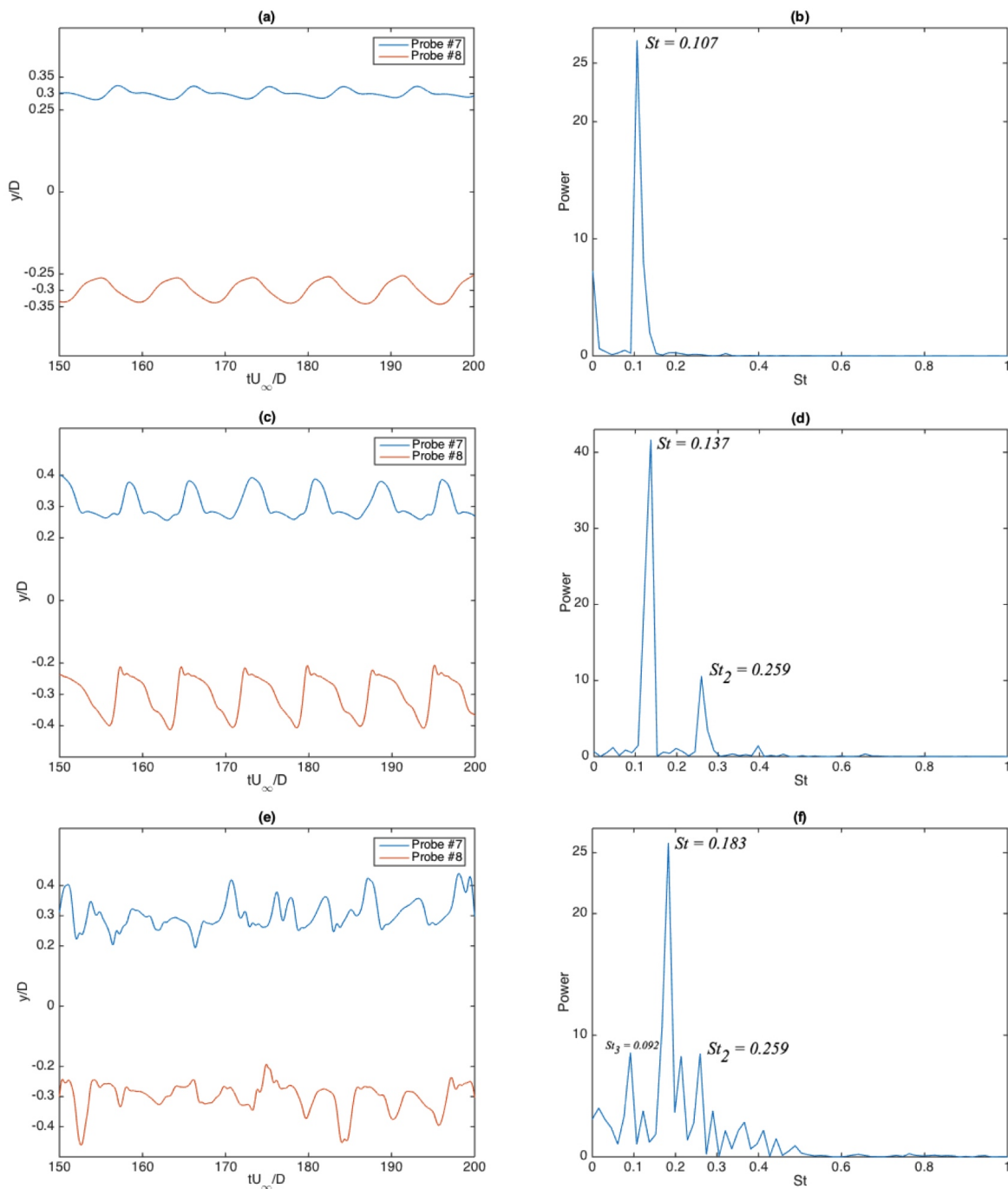
Figure 5.23: Frequency analysis of the transverse velocity v for the unsteady wake. The leftmost images show time series of velocity at two probe locations, and resulting Strouhal number to the right. (a,b) $Re = 250$; (c,d) $Re = 300$; (e,f) $Re = 500$.

Chapter 6

Conclusions and Recommendations for Further Work

6.1 Conclusions

Numerical simulations of the flow around a $L_R = 4/3$ prolate spheroid in an infinite fluid are performed for five different Reynolds numbers, $Re = 100, 200, 250, 300$ and 500. The viscous and incompressible flow was computed by the CFD software OpenFOAM. From an extensive grid dependency study at $Re = 300$, a grid consisting of 19 104 000 cells was found sufficient. The domain extends $48D$ in the streamwise direction and $24D$ in the transverse and spanwise directions. The numerical method was found to be stable for a constant time step $\Delta t = 0.002D/U_\infty$, corresponding to a maximum CFL-number well below unity over the entire mesh.

Throughout the results section, the flow around the $L_R = 4/3$ prolate spheroid are continuously compared with previously reported findings of similarly shaped bluff bodies. The main intention was to relate the present results to the flow features appearing in the wake of a sphere. The most striking discovery relating the two is the periodically shed one-sided and hairpin-shaped vortices at $Re = 300$. The wake flow rolls up and forms interconnected loops of swirling motion. A plane of symmetry is observed and aligned with the major axis of the prolate spheroid. Even though an axisymmetric sphere has no preferred orientation of the wake structures, the hairpin vortices are found to be shed with a constant orientation, resulting in a similar planar symmetry. For both the $L_R = 4/3$ prolate spheroid and the reviewed results of a sphere, the symmetry features of the wake are lost at $Re = 500$. For the highest tested Re the resulting vortex structures indicate a that the hairpin-shaped vortices are shed with alternate orientation, similar to a $L_R = 6$ prolate spheroid at $Re \geq 100$ by El Khoury et al. (2012). Correspondingly, at $Re = 500$, Tomboulides and Orszag (2000) observed that the vortices are shed with a different and chaotic orientation without planar symmetries.

By Fourier transforming a time series of transverse velocity in the wake at $Re = 300$ and 500, dominant frequencies were found for $St = 0.137$ and 0.183, respectively. For $Re = 300$, the exact same Strouhal number was observed for a sphere by Tomboulides and Orszag (2000). However, for a $L_R = 6$ prolate spheroid and infinite cylinder, higher shedding frequencies are previously reported by El Khoury et al. (2012) and Sumer and Fredsøe (1997)

of $St = 0.151$ and 0.2, respectively. The findings suggest that vortices are shed with a higher frequency as the aspect ratio L_R is increased at $Re = 300$.

For the lowest Reynolds number tested $Re = 100$, the flow was found to be steady and symmetric in the major and minor plane. A similar flow was found at $Re = 200$, but the planar symmetry in the minor plane was lost. For the same two Reynolds numbers, the flow around a sphere is steady. However, due to its circular cross-section the wake is axisymmetric. The wake behind a sphere remains steady until a critical Reynolds number in the range 270 $< Re < 300$ is reached. The present study suggests an onset of unsteadiness in the range $200 < Re < 250$. The critical Reynolds number is consistent with the experimentally found Re_c for a $L_R = 1.3$ cylinder with hemispherical ends by Schouveiler and Provansal (2001).

An interesting discovery, relating the $L_R = 4/3$ prolate spheroid to similar bluff bodies with asymmetric cross-sections, is the axis switching phenomenon. At a distance between $4D$ and $7D$ downstream, the major axis of the wake is rotated and aligns with the minor axis of the prolate spheroid. The described axis switching was observed for $Re = 300$ and 500 of the present study. A similar wake behavior was observed behind a $L_R = 6$ prolate spheroid with an axis switching at approximately $10D$ downstream at $Re \geq 100$ (El Khoury et al., 2012). However, for the unsteady flow at $Re = 250$, the asymmetry of the $L_R = 4/3$ prolate spheroid wake is lost, and a circular cross-section is observed at a distance $4D$ and $7D$ downstream.

The resulting force coefficients of the present study confirm the close relationship to the flow around a sphere. The mean drag coefficient at $Re = 300$, $C_D' = 0.664$, deviates only 1.22% and -2.78% from the numerically obtained C_D' by Johnson and Patel (1999) and Ploumhans et al. (2002), respectively.

Therefore, several flow features appearing in the wake of a sphere are maintained for the low aspect ratio ($L_R = 4/3$) prolate spheroid at the tested Re. However, the presence of an asymmetric cross-section introduces similarities to the results of higher aspect ratio bluff bodies, as the $L_R = 6$ prolate spheroid.

6.2   Recommendations for Further Work

Because of no previously reported studies of the flow around a $L_R = 4/3$ prolate spheroid, the present work has been limited to low Reynolds number flow up to $Re = 500$ in an infinite fluid. Therefore, compared with the flow around a full-scale fish farm, significant simplifications are introduced. To increase the practical relevance, the following alterations are suggested:

Increase Reynolds number to simulate turbulent flow. The dimensions of the full-scale model will induce turbulent flow behavior even at low current velocities. To simulate a realistic wake flow, an appropriate turbulence model must, therefore, be chosen.

Introduce a near wall boundary condition below the model to simulate a shallow water condition. The presence of a rigid wall in the proximity of a cylinder has been thoroughly studied, and found to affect both the flow and forces on it. Therefore, it is of interest to investigate how the flow changes as the water depth decrease. This would

also indicate possible depth limitations or preferences for the closed containment fish cage.

Simulate a tandem configuration consisting of two identical prolate spheroids. Regarding an entire fish farm, the flow is expected to be influenced by neighboring fish cages. Therefore, the resulting hydrodynamic forces for a prolate spheroid placed in the wake of an identical body are of interest.

Introduce a free surface to simulate the real level of submergence. According to the developer Hauge Aqua (2016), 90 percent of the "The-Egg" is supposed to be submerged when operated. For a partly submerged body, the hydrodynamic forces will also be caused by waves. Depending on the presence of waves for the full-scale fish farm, the simulation of a free surface might be of relevance.

Validate the numerical findings by flow visualization experiments at corresponding Reynolds numbers. For this purpose, a physical model of the present prolate spheroid has been made with a diameter $D = 40$ mm.

Bibliography

Çengel, Y. A. and Cimbala, J. M. (2008). *Essentials of fluid mechanics: fundamentals and applications.* McGraw-Hill Higher Education.

El Khoury, G. K., Andersson, H. I., and Pettersen, B. (2012). Wakes behind a prolate spheroid in crossflow. *Journal of Fluid Mechanics*, 701:98–136.

Ferziger, J. H. and Peric, M. (2012). *Computational methods for fluid dynamics.* Springer Science & Business Media.

Greenshields, C. (2015a). "openfoam programmers guide. *http://foam.sourceforge.net/docs/Guides-a4/ProgrammersGuide.pdf*.

Greenshields, C. (2015b). "openfoam user guide. *http://foam.sourceforge.net/docs/Guides-a4/UserGuide.pdf*.

Hauge Aqua, A. (2016). Technology for sustainable growth in aquaculture. `http://www.haugeaqua.com/`. [Online; accessed 26-August-2016].

Issa, R. I. (1986). Solution of the implicitly discretised fluid flow equations by operator-splitting. *Journal of computational physics*, 62(1):40–65.

Jeong, J. and Hussain, F. (1995). On the identification of a vortex. *Journal of fluid mechanics*, 285:69–94.

Johnson, T. and Patel, V. (1999). Flow past a sphere up to a reynolds number of 300. *Journal of Fluid Mechanics*, 378:19–70.

Kiya, M. and Abe, Y. (1999). Turbulent elliptic wakes. *Journal of fluids and structures*, 13(7):1041–1067.

Meneghini, J., Saltara, F., Siqueira, C., and Ferrari, J. (2001). Numerical simulation of flow interference between two circular cylinders in tandem and side-by-side arrangements. *Journal of fluids and structures*, 15(2):327–350.

Mittal, S. (2005). Excitation of shear layer instability in flow past a cylinder at low reynolds number. *International journal for numerical methods in fluids*, 49(10):1147–1167.

Ong, M. C., Utnes, T., Holmedal, L. E., Myrhaug, D., and Pettersen, B. (2010). Numerical simulation of flow around a circular cylinder close to a flat seabed at high reynolds numbers using a k–ε model. *Coastal Engineering*, 57(10):931–947.

Ploumhans, P., Winckelmans, G., Salmon, J. K., Leonard, A., and Warren, M. (2002). Vortex methods for direct numerical simulation of three-dimensional bluff body flows: application to the sphere at re= 300, 500, and 1000. *Journal of Computational Physics*, 178(2):427–463.

Qu, L., Norberg, C., Davidson, L., Peng, S.-H., and Wang, F. (2013). Quantitative numerical analysis of flow past a circular cylinder at reynolds number between 50 and 200. *Journal of Fluids and Structures*, 39:347–370.

Sakamoto, H. and Haniu, H. (1990). A study on vortex shedding from spheres in a uniform flow. *Journal of Fluids Engineering*, 112(4):386–392.

Sandberg, P. (2016). Speech: The government's strategy for sustainable growth. `https://www.regjeringen.no/en/aktuelt/speech-the-governments-strategy-for-sustainable-growth/id2502481/`. [Online; accessed 25-October-2016].

Schlichting, H. (1979). *Boundary-layer theory, 7th ed.* McGraw-Hill.

Schouveiler, L. and Provansal, M. (2001). Periodic wakes of low aspect ratio cylinders with free hemispherical ends. *Journal of fluids and structures*, 15(3):565–573.

Sheard, G., Thompson, M., and Hourigan, K. (2008). Flow normal to a short cylinder with hemispherical ends. *Physics of Fluids (1994-present)*, 20(4):041701.

Sheard, G., Thompson, M. C., and Hourigan, K. (2004). Flow past a cylinder with free hemispherical ends: Comments on grid independence and wake symmetry characteristics. In *Under consideration for presentation at the Fifteenth Australasian Fluid Mechanics Conference.*

Sumer, B. M. and Fredsøe, J. (1997). *Hydrodynamics around cylindrical structures*, volume 12. World Scientific.

Taneda, S. (1956). Experimental investigation of the wake behind a sphere at low reynolds numbers. *Journal of the Physical Society of Japan*, 11(10):1104–1108.

Taneda, S. (1978). Visual observations of the flow past a sphere at reynolds numbers between 10 4 and 10 6. *Journal of Fluid Mechanics*, 85(01):187–192.

The Norwegian Ministry of Trade, I. and Fisheries (2014). Aquaculture. `http://www.fisheries.no/aquaculture/Aquaculture/`. [Online; accessed 13-September-2016].

Tomboulides, A. G. and Orszag, S. A. (2000). Numerical investigation of transitional and weak turbulent flow past a sphere. *Journal of Fluid Mechanics*, 416(1):45–73.

Versteeg, H. K. and Malalasekera, W. (2007). *An introduction to computational fluid dynamics: the finite volume method.* Pearson Education.

Zdravkovich, M. (1997). *Flow around circular cylinders. Fundamentals, vol. 1.* Oxford university press.

List of Figures

List of Tables

Appendix A

OpenFOAM Scripts

A.1 fvSchemes

```
1  /*————————————*— C++ —*————————————*\
2  | ========                 |                                  |
3  | \\      /  F ield         | The Open Source CFD Toolbox|
4  |  \\    /   O peration     | Version:   2.3.0             |
5  |   \\  /    A nd           | Web:        www.OpenFOAM.org |
6  |    \\/     M anipulation  |                                  |
7  \*————————————————————*/
8  FoamFile
9  {
10      version     2.0;
11      format      ascii;
12      class       dictionary;
13      location    "system";
14      object      fvSchemes;
15  }
16  // * * * * * * * * * * * * * * * * * * * * * * * * * * * *  //
17
18  ddtSchemes
19  {
20      default         Euler;
21  }
22
23  gradSchemes
24  {
25      default         Gauss linear;
26      grad(p)         Gauss linear;
27      grad(U)         Gauss linear;
28  }
29
```

```
30  divSchemes
31  {
32      default             none;
33      div(phi,U)          Gauss linear;
34      div((nuEff*dev2(T(grad(U))))) Gauss linear;
35  }
36
37  laplacianSchemes
38  {
39      default             Gauss linear corrected;
40  }
41
42  interpolationSchemes
43  {
44      default             linear;
45  }
46
47  snGradSchemes
48  {
49      default             corrected;
50  }
51
52  fluxRequired
53  {
54      default             no;
55      p                   ;
56  }
57
58
59  // ********************************************************* //
```

A.2 fvSolution

```
1   /*--------------------------------*- C++ -*----------------------------------*\
2   | =========                 |                                                 |
3   | \\      /  F ield          | The Open Source CFD Toolbox|
4   |  \\    /   O peration      | Version:   2.3.0           |
5   |   \\  /    A nd            | Web:       www.OpenFOAM.org |
6   |    \\/     M anipulation   |                             |
7   \*---------------------------------------------------------------------------*/
8   FoamFile
9   {
10      version     2.0;
11      format      ascii;
12      class       dictionary;
```

```
13      location        "system";
14      object          fvSchemes;
15  }
16  // * * * * * * * * * * * * * * * * * * * * * * * * * * * * * * //
17
18  solvers
19  {
20      p
21      {
22          solver              GAMG;
23          tolerance           1e-06;
24          relTol              0.05;
25          smoother            GaussSeidel;
26          nPreSweeps          0;
27          nPostSweeps         2;
28          cacheAgglomeration  on;
29          agglomerator        faceAreaPair;
30          nCellsInCoarsestLevel  10;
31          mergeLevels         1;
32      }
33
34      pFinal
35      {
36          $p;
37          tolerance           1e-06;
38          relTol              0;
39      }
40
41      U
42      {
43          solver              PBiCG;
44          preconditioner      DILU;
45          tolerance           1e-05;
46          relTol              0;
47      }
48  }
49
50  PISO
51  {
52      nCorrectors         2;
53      nNonOrthogonalCorrectors 1;
54      pRefCell            0;
55      pRefValue           0;
56  }
57
```

```
58  // ****************************************************** //
```

A.3   controlDict

```
1   /*--------------------------------*- C++ -*----------------------------------*\
2   | =========                 |                                                 |
3   | \\      /  F ield          | The Open  Source  CFD Toolbox|
4   |  \\    /   O peration       | Version:    2.3.0                 |
5   |   \\  /    A nd            | Web:          www.OpenFOAM.org |
6   |    \\/     M anipulation    |                                                 |
7   \*---------------------------------------------------------------------------*/
8   FoamFile
9   {
10      version         2.0;
11      format          ascii;
12      class           dictionary;
13      location        "system";
14      object          fvSchemes;
15  }
16  // * * * * * * * * * * * * * * * * * * * * * * * * * * * * * //
17
18  application     pisoFoam;
19
20  startFrom       latestTime;
21
22  //startTime         0;
23
24  stopAt          endTime;
25
26  endTime         418.6;
27
28  deltaT          0.004;
29
30  writeControl    timeStep;
31
32  writeInterval   455;
33
34  purgeWrite      0;
35
36  writeFormat     ascii;
37
38  writePrecision  6;
39
40  writeCompression off;
41
```

```
42  timeFormat          general;
43
44  timePrecision       6;
45
46  runTimeModifiable   false;
47
48  functions
49  {
50          forces
51          {
52                  type                    forces;
53                  functionObjectLibs      ("libforces.so");
54                  origin                  (0 0 0);
55                  CofR                    (0 0 0);
56                  outputControl           timeStep;
57                  outputInterval          1;
58                  patches                 (spheroid);
59                  pName                   p;
60                  UName                   U;
61                          rhoName                         rhoInf;
62                  rhoInf                  1000;
63                  magUInf                 1.00;
64                  log                     true;
65                  liftDir                 (0 1 0);
66                  dragDir                 (1 0 0);
67                  cofR                    (0 0 0);
68                  pitchAxis               (0 0 1);
69                  lRef                    2;
70                  Aref                    4.19;
71          }
72          forceCoeffs
73          {
74                  type                    forceCoeffs;
75                  functionObjectLibs      ("libforces.so");
76                  origin                  (0 0 0);
77                  CofR                    (0 0 0);
78                  outputControl           timeStep;
79                  outputInterval          1;
80                  patches                 (spheroid);
81                  pName                   p;
82                  UName                   U;
83                  rhoName                 rhoInf;
84                  rhoInf                  1000;
85                  magUInf                 1.00;
86                  log                     true;
```

```
87                liftDir                (0  1  0);
88                dragDir                (1  0  0);
89                cofR                   (0  0  0);
90                pitchAxis              (0  0  1);
91                lRef                   2;
92                Aref                   4.19;
93         }
94      probes
95      {
96                functionObjectLibs ( "libsampling.so" );
97                type         probes;
98                name         probes;
99                fields (
100                        p
101                        U
102                       );
103        probeLocations
104        (
105        (2.0    0.4   0)       // x = 1D,  y =  0.2D,  z = 0
106        (2.0   -0.4   0)       // x = 1D,  y = -0.2D,  z = 0
107        (2.0    0.4   0.67)    // x = 1D,  y =  0.2D,  z = 0.33D
108        (2.0   -0.4   0.67)    // x = 1D,  y = -0.2D,  z = 0.33D
109        (2.0    0.4  -0.67)    // x = 1D,  y =   0.2D,  z = -0.33D
110        (2.0   -0.4  -0.67)    // x = 1D,  y = -0.2D,  z = -0.33D
111        (11.5   0.6   0)       // x = 5.75D,  y = 0.3D,  z = 0
112        (11.5  -0.6   0)       // x = 5.75D,  y = -0.3D,  z = 0
113        );
114     }
115      #include "wallBoundedStreamLines"
116  }
117
118  // ***************************************************** //
```

A.4 WallBoundedStreamLines

```
1  /*---------------------------*- C++ -*---------------------------*\
2  | =========                 |                                     |
3  | \\      /  F ield          | The Open Source CFD Toolbox|
4  |  \\    /   O peration      | Version:   2.3.0               |
5  |   \\  /    A nd            | Web:        www.OpenFOAM.org |
6  |    \\/     M anipulation   |                                 |
7  \*---------------------------------------------------------------*/
8
9  // Interpolate U to create near-wall UNear
10  near
```

```
11  {
12      functionObjectLibs ("libfieldFunctionObjects.so");
13      type nearWallFields;
14
15      outputControl    outputTime;
16
17      fields
18      (
19          (U UNear)
20          (p pNear)
21      );
22
23      patches (spheroid); // Patches to sample
24
25      distance 0.005; // Radial distance to sample
26  }
27
28  wallBoundedStreamLines
29  {
30
31      functionObjectLibs ("libfieldFunctionObjects.so");
32      type              wallBoundedStreamLine;
33
34      outputControl    outputTime;
35
36      setFormat         vtk;
37
38      UName UNear; // Velocity field to use for tracking.
39
40      // Interpolation method.
41
42      trackForward       true;
43
44      interpolationScheme cellPoint;
45
46      fields (p U UNear);
47
48      lifeTime          100; // Steps particles can travel before
              being removed
49
50      cloudName         wallBoundedParticleTracks;
51
52      seedSampleSet    patchSeed; // Seeding method
53
54      uniformCoeffs
```

```
55      {
56          type            uniform;
57          axis            x;
58
59          start           (0.0035  0.0999  0.0001);
60          end             (0.0035  0.0999  0.0099);
61          nPoints         20;
62      }
63      cloudCoeffs
64      {
65          type            cloud;
66          axis            x;
67          points          ((0.351516548679288  -0.0116085375585099  1.24))
                ;
68      }
69      patchSeedCoeffs
70      {
71          type            patchSeed;
72          patches         (spheroid);
73          axis            x;
74          maxPoints       20000;
75      }
76  }
77
78  // ***************************************************** //
```

Appendix B

MATLAB Script

B.1 Frequency Analysis by a Fast Fourier Transformation

```matlab
%%%%%%%%% POST−PROCESSING DATA FROM OPENFOAM %%%%%%%%%%
clear all;
close all;

%%%%%%%%%%%%%%% IMPORT PROBE DATA %%%%%%%%%%%%%%%%%%%

%——————— t = 0 − 400s ——————————%
path = '/Users/Stiannev/Documents/MATLAB/Master thesis/grid_study/
    Re300/domain_size/bigger_12D/postProcessing/probes/0';
paths1 = path;
%——————— Import velocity ——————————%
fid = fopen([paths1,'/U'],'rt');
A = textscan(fid,'%f (%f %f %f) (%f %f %f) (%f %f %f) (%f %f %f)
    (%f %f %f) (%f %f %f) (%f %f %f) (%f %f %f)','HeaderLines',10);
Length_U = length(A{1,1}(:,1));
cut = 75000:Length_U;  % Cut for t = 300 − 400s
%————————————————————————%

%%%%%%%%%%%%% FREQUENCY ANALYSIS %%%%%%%%%%%%%%%%%%%

%—— FFT of the transverse velocity signal ——%
probenr = 7;  % Looking at probe # n.
trans_velocity = probe_vel(cut,(probenr+1)*3)';  % Transverse
    velocity component for probe # n.
n = length(trans_velocity);  % Length of velocity vector.
dt = 0.004;  % Time step between each measured velocity.
fs = 1/dt;  % Sampling frequency.
t = (0:(n−1))/fs;  % Creates time vector.
```

```matlab
26  o = pow2(nextpow2(n));  % Zero-pads the signal to give it the
        closest power-of-two number of sample points.
27  y = fft(trans_velocity,o);  % Fourier transforms the signal.
28  f = (0:(o-1))*(fs/o);  % Computes the frequency vector associated
        with the signal
29  power = y.*conj(y)/o; % Computes the power spectra (energy at
        various frequencies) by means of the complex conjugate
30  %————————————————————————————————————————————%
31
32  %—— Plot the resulting power spectra ——%
33  figure
34  plot(f*2,power); % Multiplying frequency by diameter of spheroid (
        D = 2) to get Strouhal number along x-axis. (inflow = 1m/s)
35  set(gca,'FontSize',14);
36  xlim([0 1]);
37  ylim([0 43]);
38  xlabel('St');
39  ylabel('Power');
40  %————————————————————————————————————————————%
```

Appendix C

Mesh Properties

C.1   checkMesh Results for the Final Grid

```
1  /*————————————————*— C++ —*————————————————*\
2  |  ========                 |                                           |
3  |  \\      /    F ield        |  The  Open  Source  CFD  Toolbox|
4  |   \\    /     O peration    |  Version:     2.3.0                 |
5  |    \\  /      A nd          |  Web:         www.OpenFOAM.org   |
6  |     \\/       M anipulation |                                           |
7  \*————————————————————————————————*/
8  Build   : v3.0+−e941ee6c15e9
9  Exec    : checkMesh
10 Date    : Nov  25  2016
11 Time    : 13:48:39
12 Host    : "r3i5n15"
13 PID     : 7454
14 Case    : /work/stiannev/grid_study/Re300/domain_size/bigger_12D
15 nProcs  : 1
16 sigFpe : Enabling  floating  point  exception  trapping  (FOAM_SIGFPE) .
17 fileModificationChecking : Monitoring  run−time  modified  files
       using  timeStampMaster
18 allowSystemOperations : Allowing  user−supplied  system  call
       operations
19
20 // * * * * * * * * * * * * * * * * * * * * * * * * *  //
21 Create  time
22
23 Create  polyMesh  for  time = 0
24
25 Time = 0
26
27 Mesh  stats
```

```
28      points :           19317242
29      faces :            57524600
30      internal  faces :  57099400
31      cells :            19104000
32      faces  per  cell :  6
33      boundary  patches : 5
34      point  zones :      0
35      face  zones :       0
36      cell  zones :       0
37
38  Overall  number  of  cells  of  each  type :
39      hexahedra :        19104000
40      prisms :           0
41      wedges :           0
42      pyramids :         0
43      tet  wedges :       0
44      tetrahedra :        0
45      polyhedra :         0
46
47  Checking  topology ...
48      Boundary  definition  OK.
49      Cell  to  face  addressing  OK.
50      Point  usage  OK.
51      Upper  triangular  ordering  OK.
52      Face  vertices  OK.
53      Number  of  regions : 1  (OK).
54
55  Checking  patch  topology  for  multiply  connected  surfaces ...
56      Patch              Faces      Points      Surface  topology
57      spheroid           55800      55802       ok ( closed  singly
            connected )
58      outlet             48300      48741       ok (non−closed  singly
            connected )
59      inlet              48300      48741       ok (non−closed  singly
            connected )
60      topAndBottom       130200     131242      ok (non−closed  singly
            connected )
61      frontAndBack       142600     143682      ok (non−closed  singly
            connected )
62
63  Checking  geometry ...
64      Overall  domain  bounding  box  (−24  −24  −24)  (72  24  24)
65      Mesh  has  3  geometric  (non−empty/wedge)  directions  (1 1 1)
66      Mesh  has  3  solution  (non−empty)  directions  (1 1 1)
67      Boundary  openness  (−1.21004e−14  −2.02728e−14  −3.41435e−15)  OK.
```

```
68        Max cell openness = 3.62322e−16 OK.
69        Max aspect ratio = 8.82723 OK.
70        Minimum face area = 7.35462e−05. Maximum face area = 0.49949.
            Face area magnitudes OK.
71        Min volume = 7.99913e−07. Max volume = 0.296547.  Total volume
            = 221178.  Cell volumes OK.
72        Mesh non−orthogonality Max: 55.4075 average: 10.1962
73        Non−orthogonality check OK.
74        Face pyramids OK.
75        Max skewness = 0.768401 OK.
76        Coupled point location match (average 0) OK.
77
78  Mesh OK.
79
80  End
```

Appendix D

Flow Visualization Results

D.1   Separation Lines
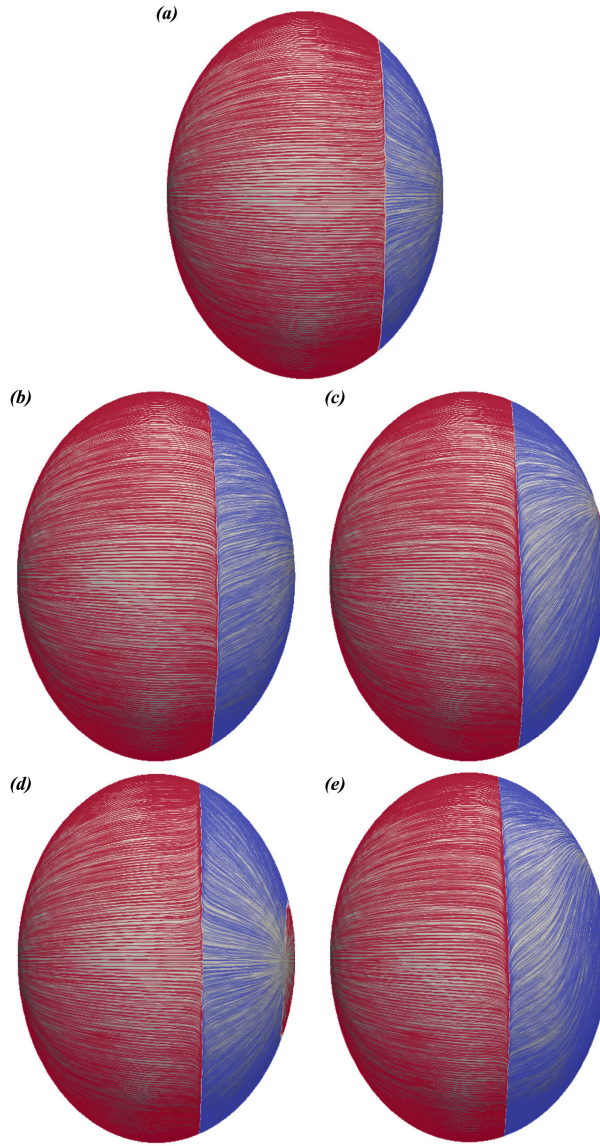
Figure D.1: Separation line along the span of the spheroid, visualized by streamwise velocity (u) close to the spheroid surface. The blue and red coloring represent $u \leq -10^{-4}$ and $u \geq 10^{-4}$, respectively. (a) $Re = 100$; (b) $Re = 200$; (c) $Re = 250$; (d) $Re = 300$; (e) $Re = 500$.

D.2   Time series of Velocity at Re = 100
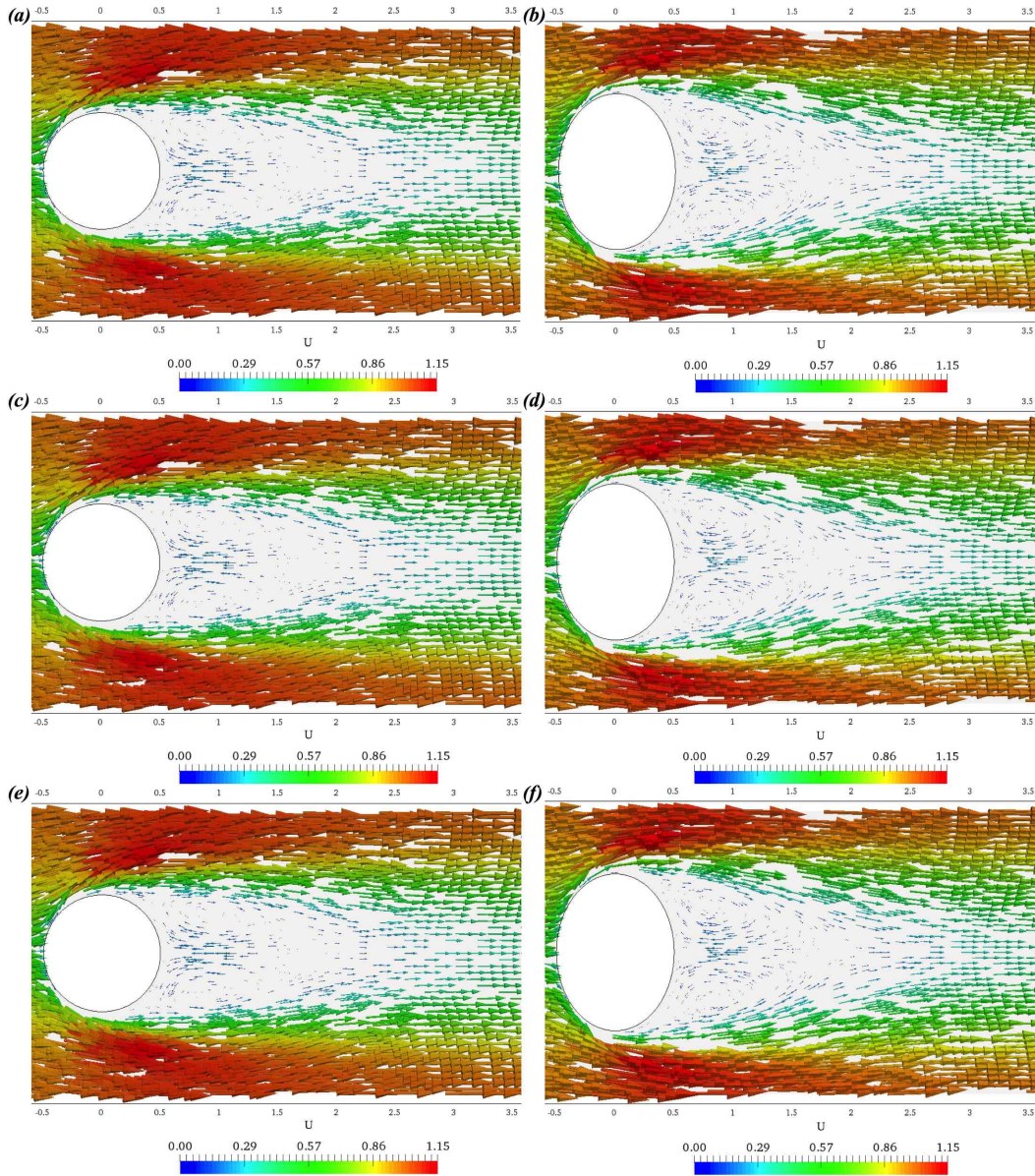
Figure D.2: Time series of the near velocity field in the middle minor plane (left images) and middle major plane (right images). (a,b) t = t_0; (c,d) t = $t_0 + 2.5D/U_\infty$; (e,f) t = $t_0 + 5D/U_\infty$.

D.3   Time series of Velocity at Re $= 200$
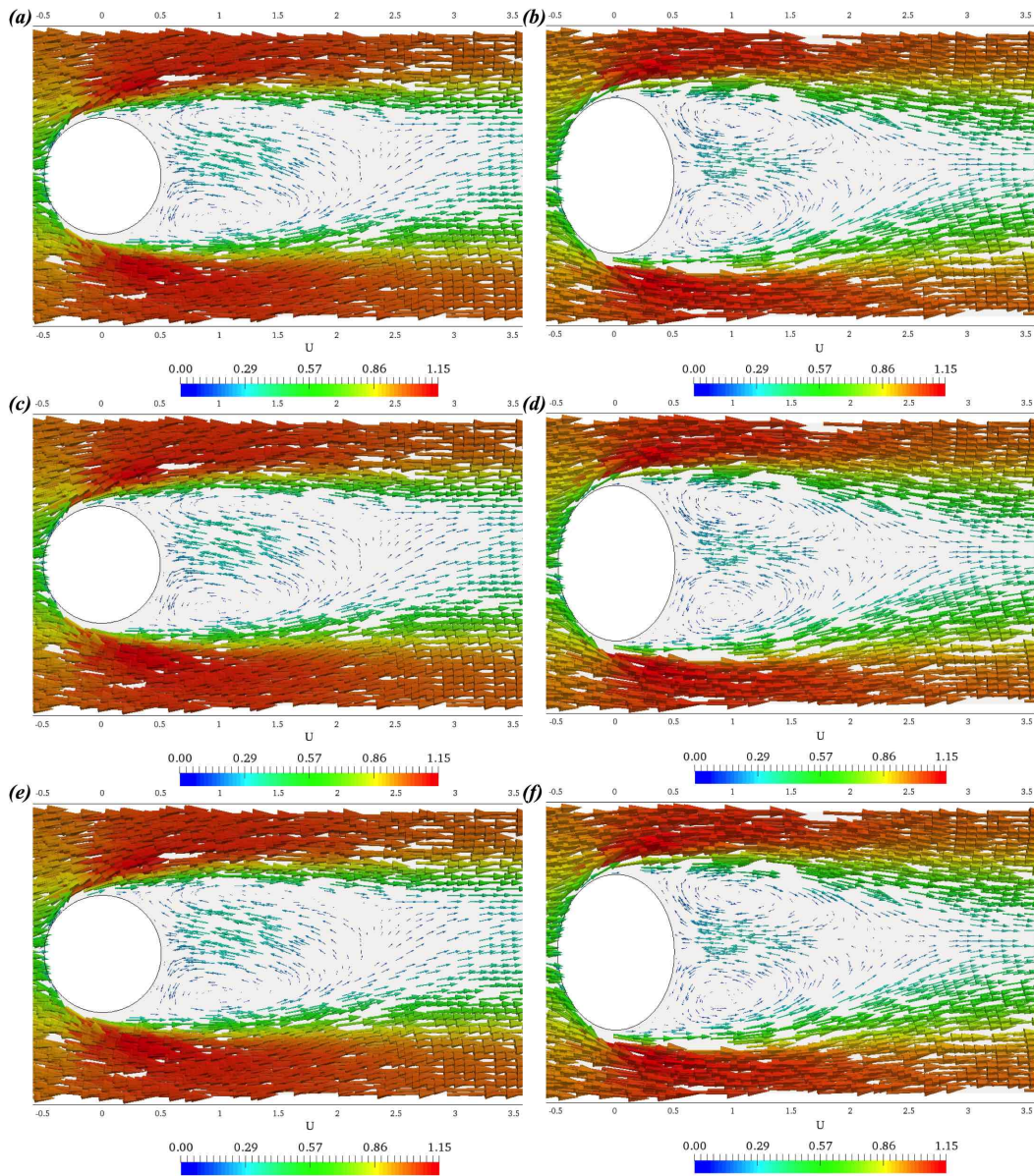
Figure D.3: Time series of the near velocity field in the middle minor plane (left images) and middle major plane (right images). (a,b) t $= t_0$; (c,d) t $= t_0 + 1.82D/U_\infty$; (e,f) t $= t_0 + 3.64D/U_\infty$.
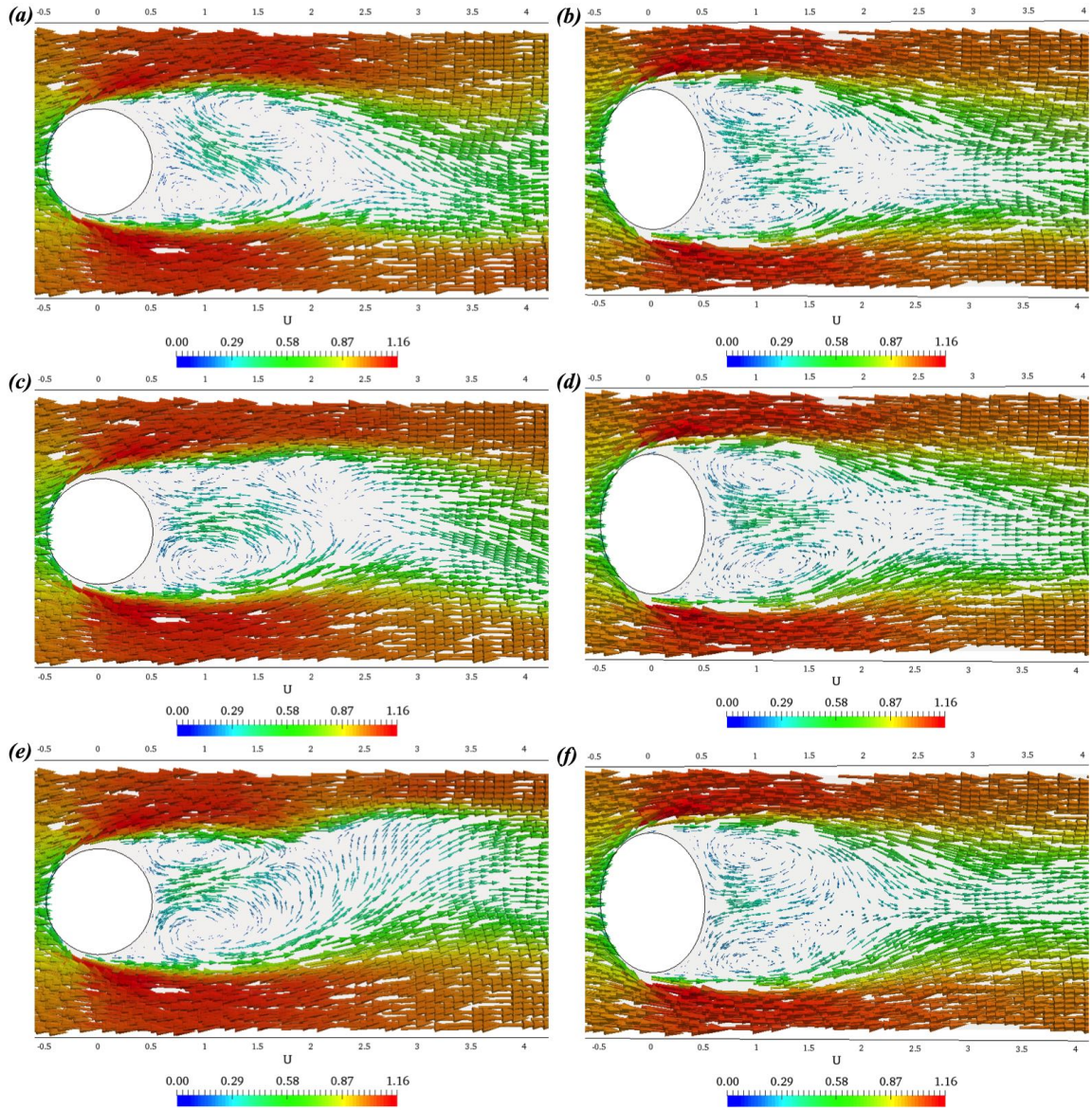
D.4   Time Series of Velocity at Re = 250
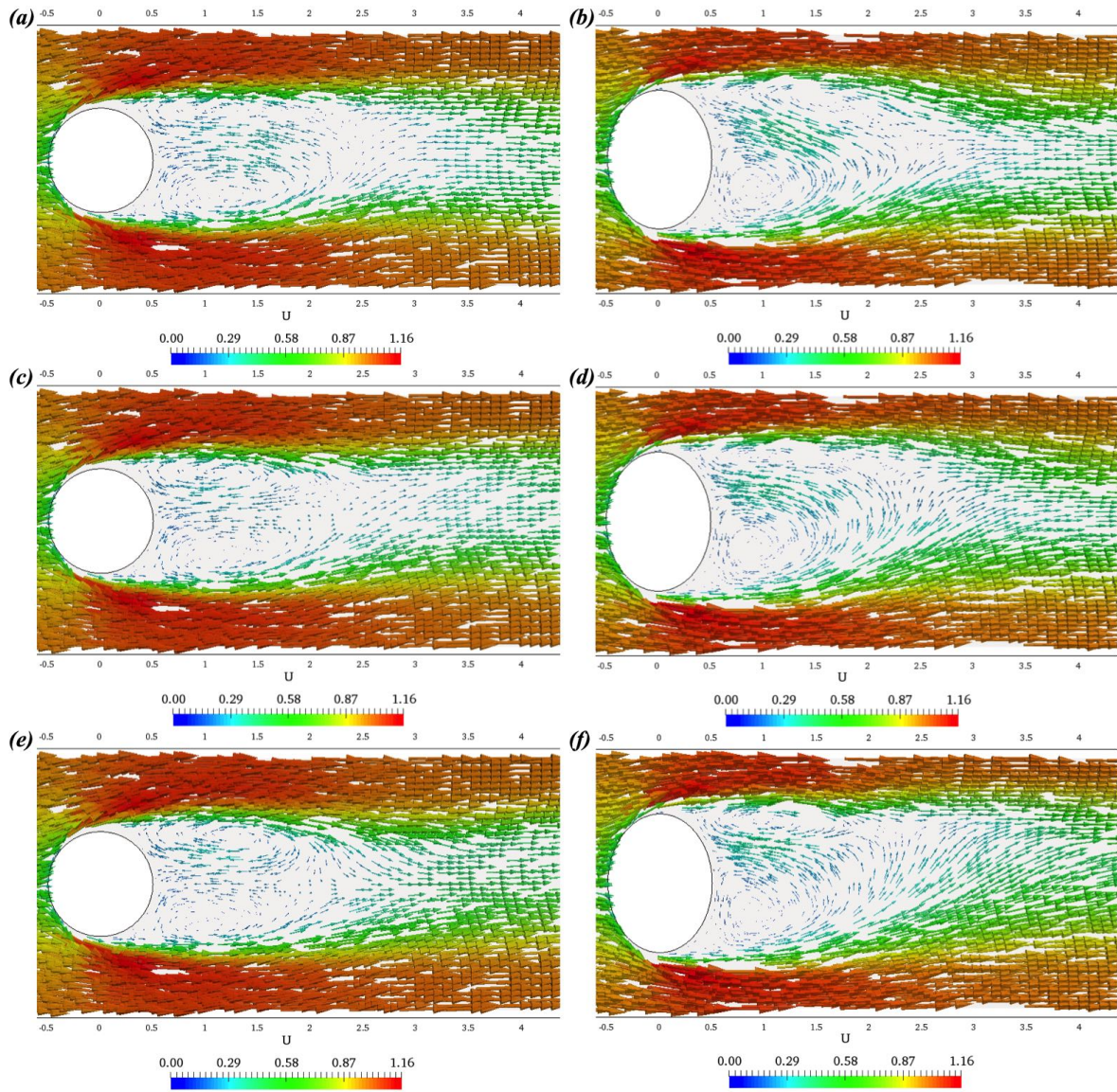
Figure D.4: (Part 1 of 2) Time series of the near velocity field in the middle minor plane (left images) and middle major plane (right images). (a,b) t = t_0; (c,d) t = $t_0 + 1.82D/U_\infty$; (e,f) t = $t_0 + 3.64D/U_\infty$.
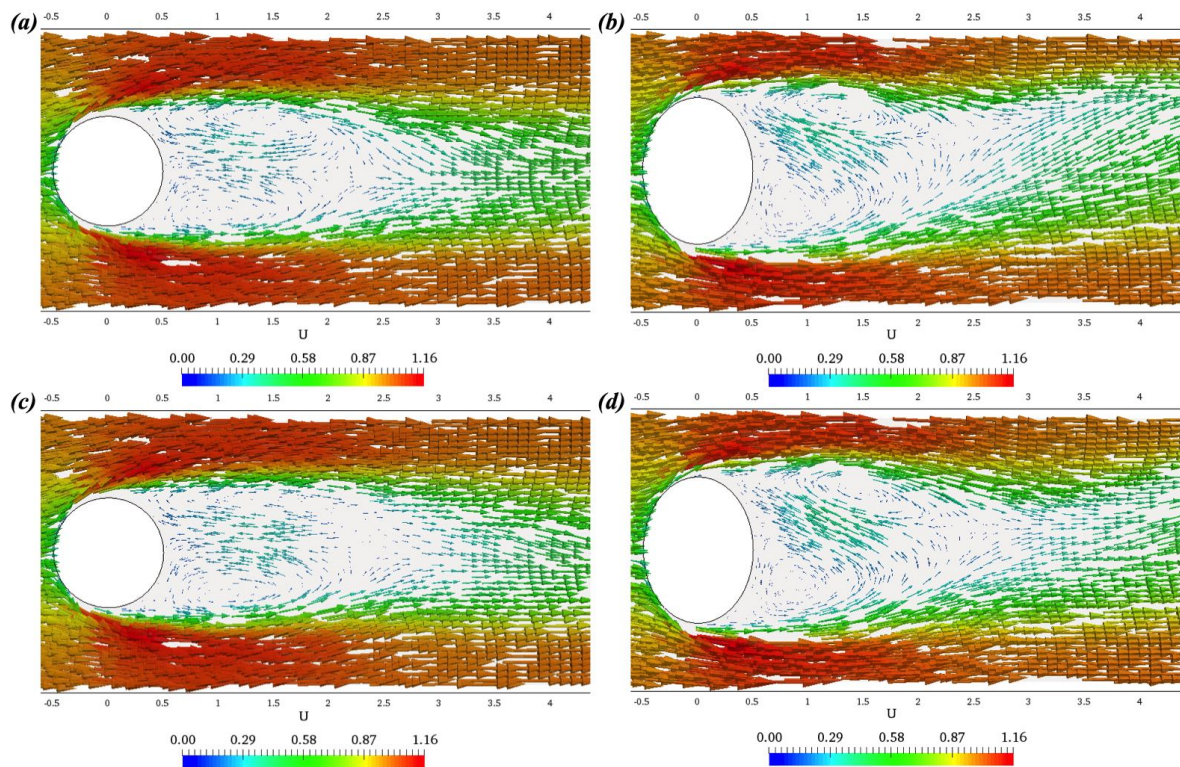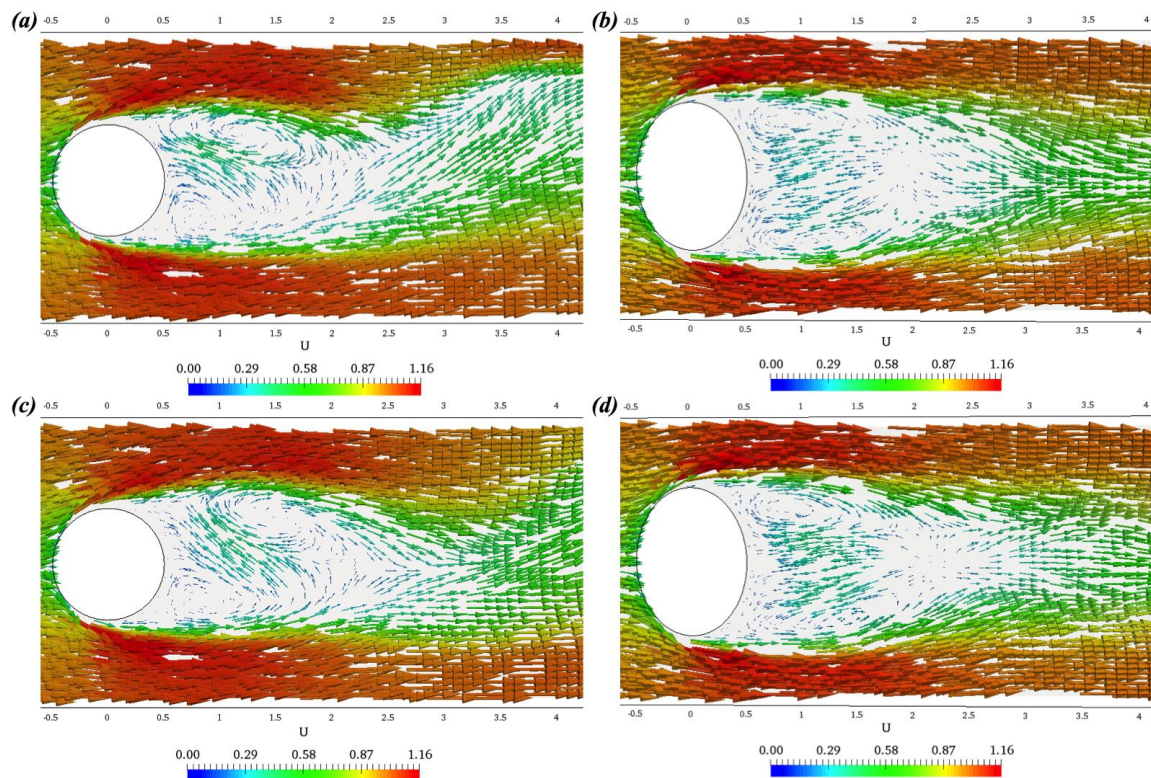
Figure D.5: (Part 2 of 2) Time series of the near velocity field in the middle minor plane (left images) and middle major plane (right images). (a,b) t = t_0 + $5.46D/U_\infty$; (c,d) t = t_0 + $7.28D/U_\infty$.
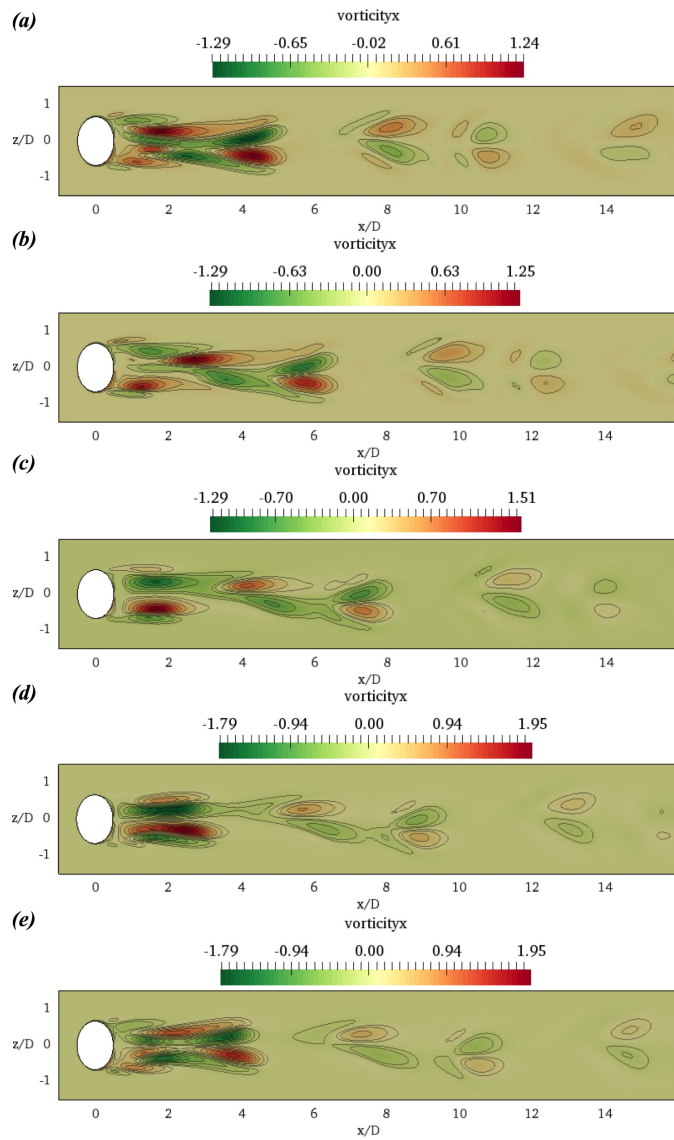
D.5 Time Series of Vorticity at Re = 250
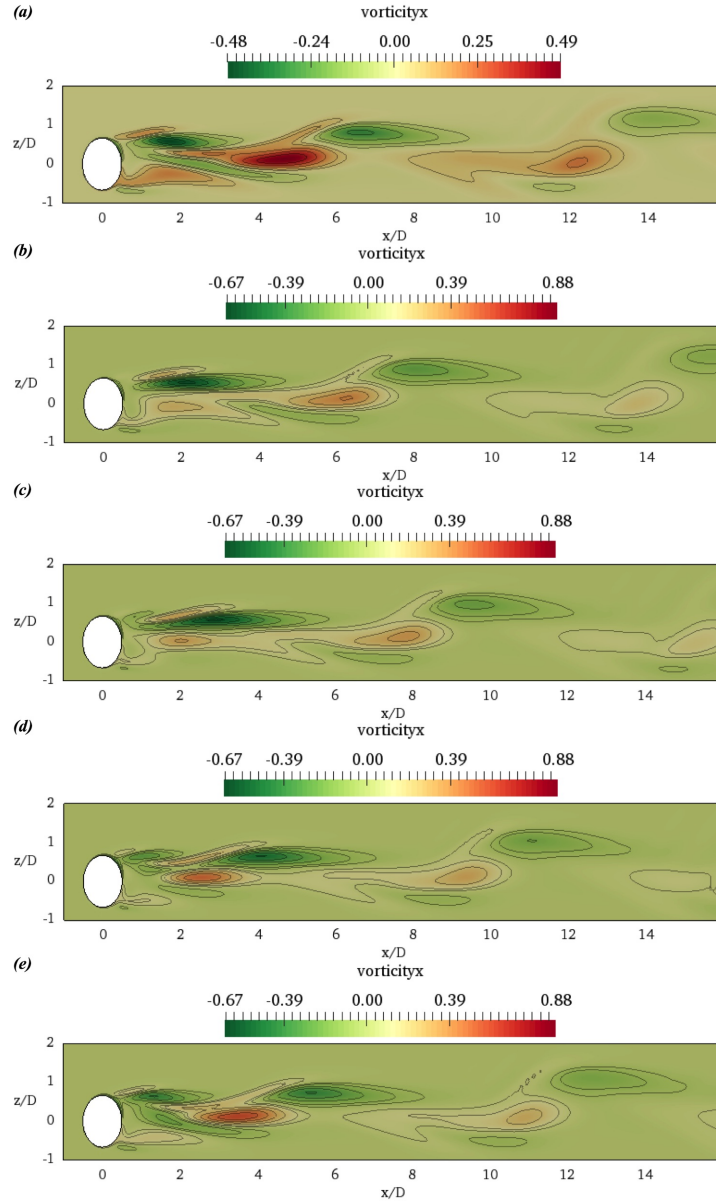
Figure D.6: Time series of streamwise vorticity ω_x contours, in the middle (x,z)-plane. (a) t = t_0; (b) t = $t_0 + 1.82D/U_\infty$; (c) t = $t_0 + 3.64D/U_\infty$; (d) t = $t_0 + 5.46D/U_\infty$; (e) t = $t_0 + 7.28D/U_\infty$.
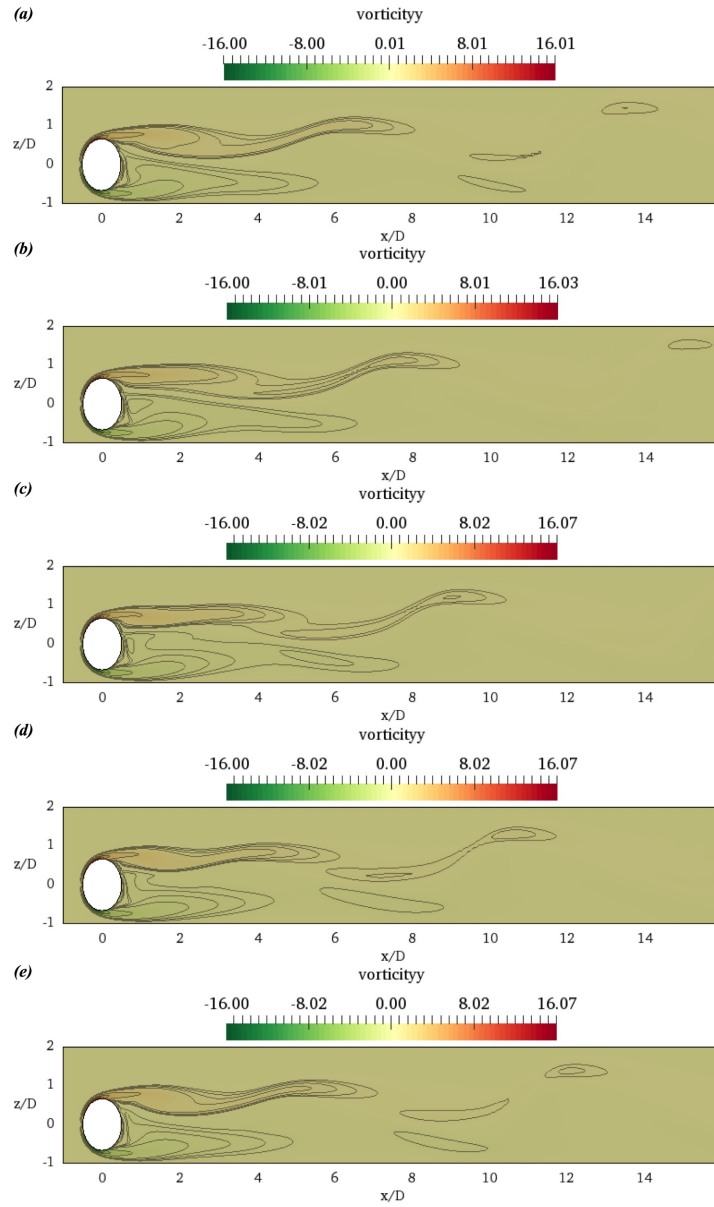
Figure D.7: Time series of transverse vorticity ω_y contours, in the middle (x,z)-plane. (a) t $= t_0$; (b) t $= t_0 + 1.82D/U_\infty$; (c) t $= t_0 + 3.64D/U_\infty$; (d) t $= t_0 + 5.46D/U_\infty$; (e) t $= t_0 + 7.28D/U_\infty$.
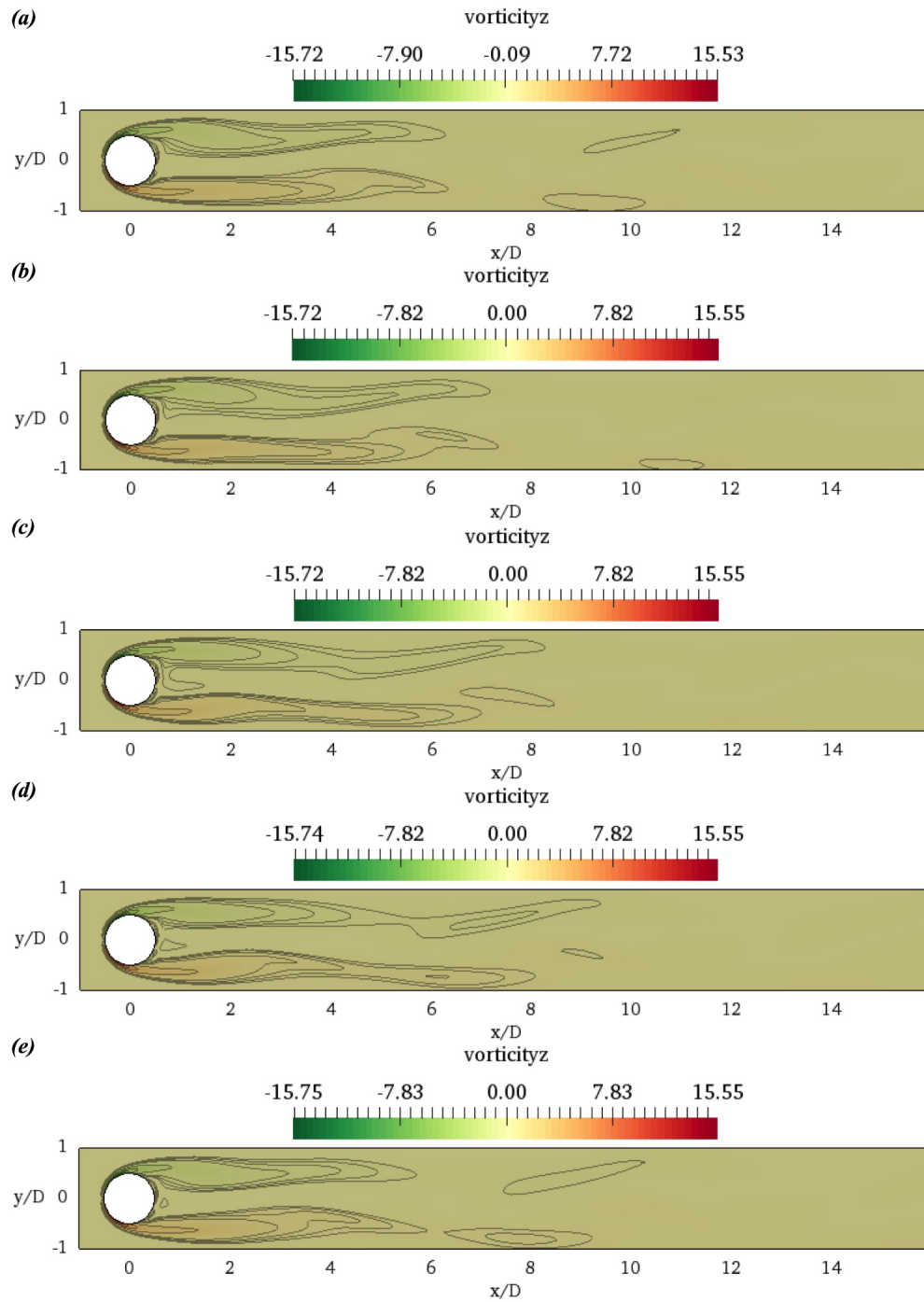
Figure D.8: Time series of transverse vorticity ω_z contours, in the middle (x,y)-plane. (a) t $= t_0$; (b) t $= t_0 + 1.82D/U_\infty$; (c) t $= t_0 + 3.64D/U_\infty$; (d) t $= t_0 + 5.46D/U_\infty$; (e) t $= t_0 + 7.28D/U_\infty$.
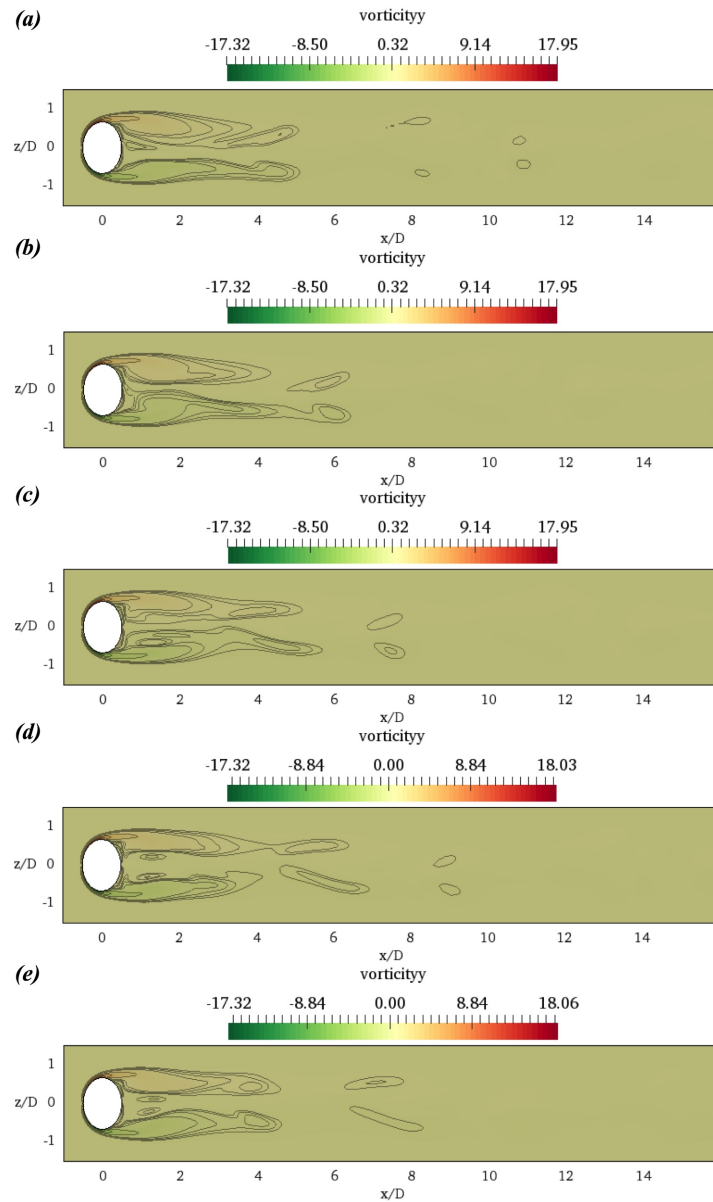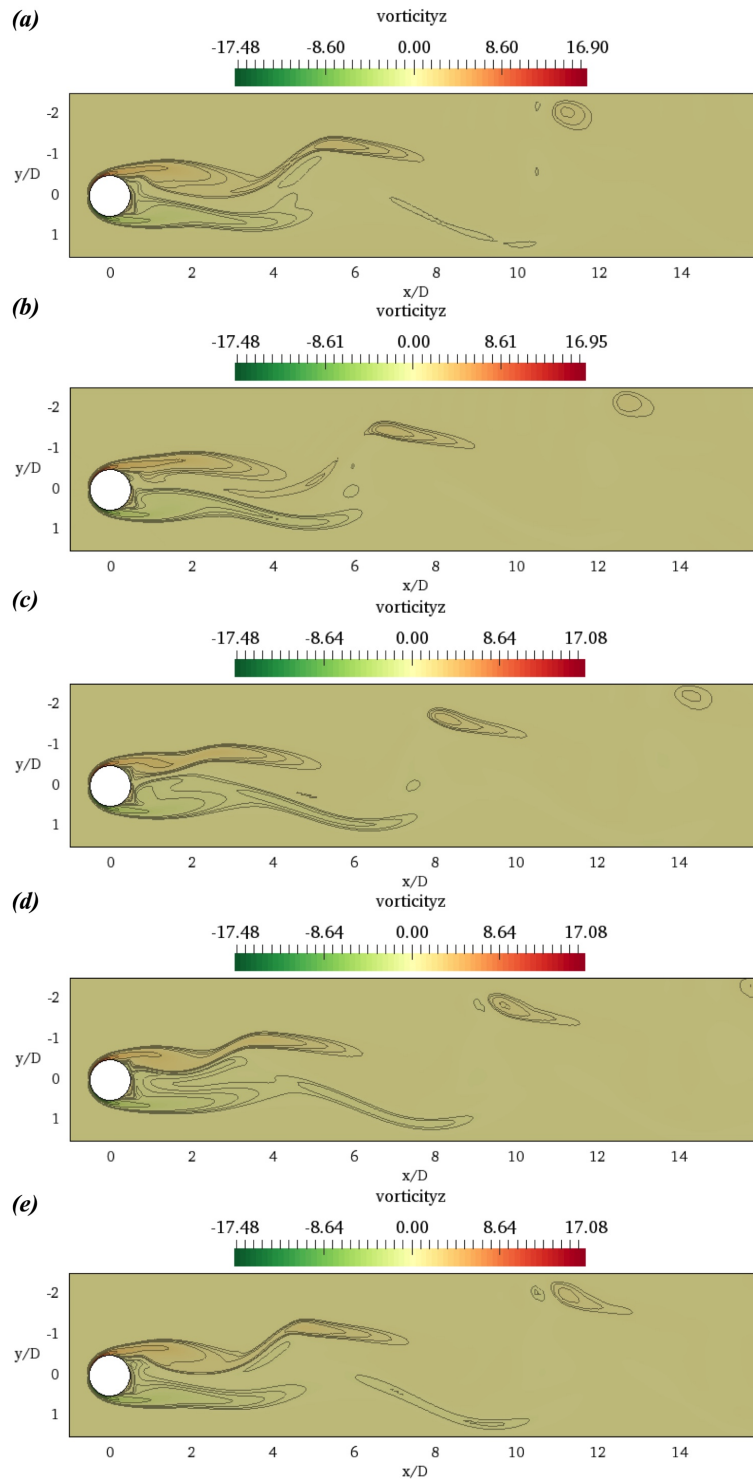
D.6   Time Series of Velocity at Re = 300

Figure D.9: (Part 1 of 2) Time series of the near velocity field in the middle minor plane (left images) and middle major plane (right images). (a,b) t $= t_0$; (c,d) t $= t_0 + 1.82D/U_\infty$; (e,f) t $= t_0 + 3.64D/U_\infty$.

Figure D.10: (Part 2 of 2) Time series of the near velocity field in the middle minor plane (left images) and middle major plane (right images). (a,b) t = t_0 + 5.46D/U_∞; (c,d) t = t_0 + 7.28D/U_∞.

D.7   Time Series of Vorticity at Re = 300

Figure D.11: Time series of streamwise vorticity ω_x contours, in the middle (x,z)-plane. (a) t = t_0; (b) t = t_0 + 1.82D/U_∞; (c) t = t_0 + 3.64D/U_∞; (d) t = t_0 + 5.46D/U_∞; (e) t = t_0 + 7.28D/U_∞.
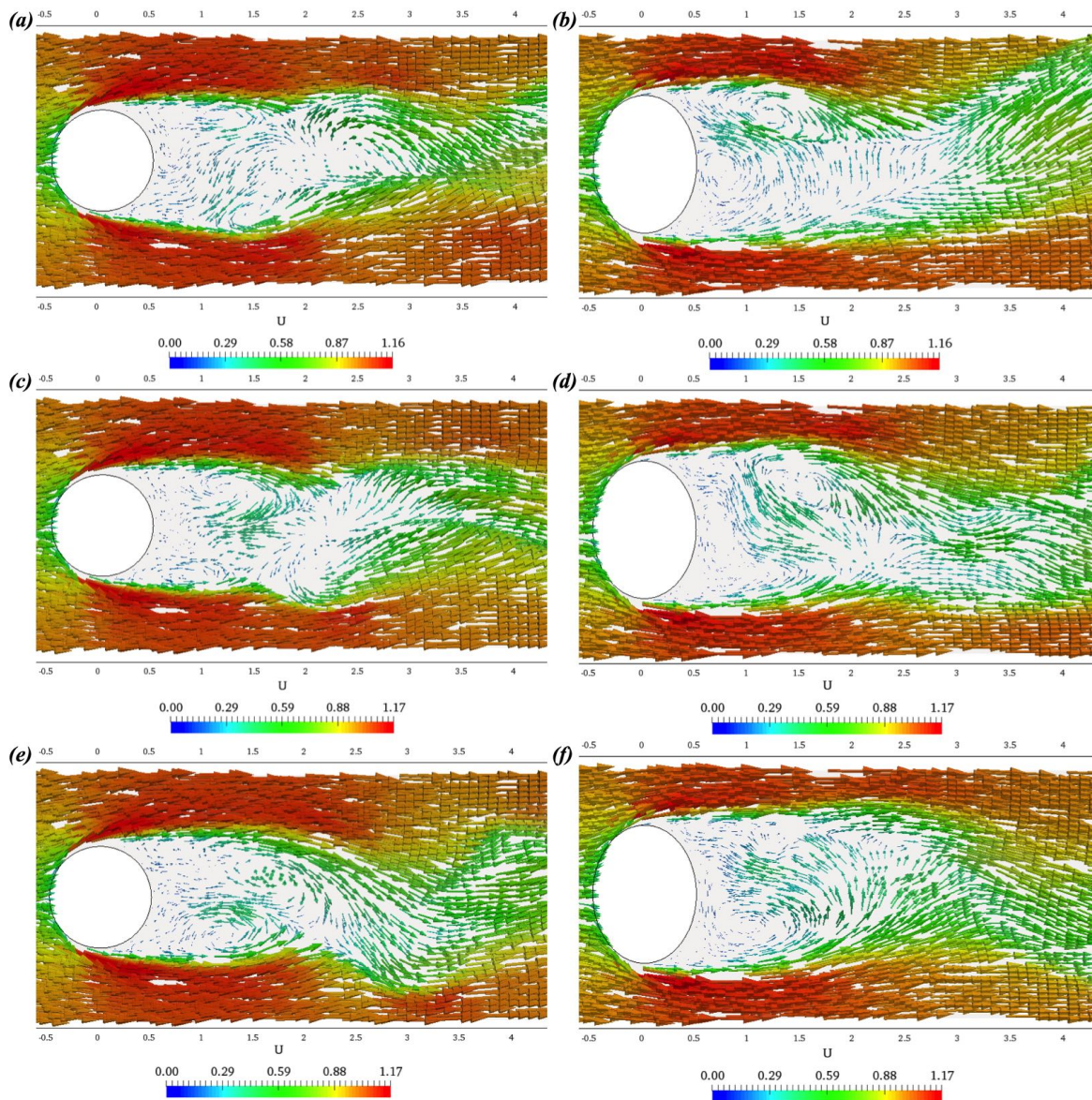
Figure D.12: Time series of transverse vorticity ω_y contours, in the middle (x,z)-plane. (a) t $= t_0$; (b) t $= t_0 + 1.82D/U_\infty$; (c) t $= t_0 + 3.64D/U_\infty$; (d) t $= t_0 + 5.46D/U_\infty$; (e) t $= t_0 + 7.28D/U_\infty$.

Figure D.13: Time series of transverse vorticity ω_z contours, in the middle (x,y)-plane. (a) t = t_0; (b) t = $t_0 + 1.82D/U_\infty$; (c) t = $t_0 + 3.64D/U_\infty$; (d) t = $t_0 + 5.46D/U_\infty$; (e) t = $t_0 + 7.28D/U_\infty$.
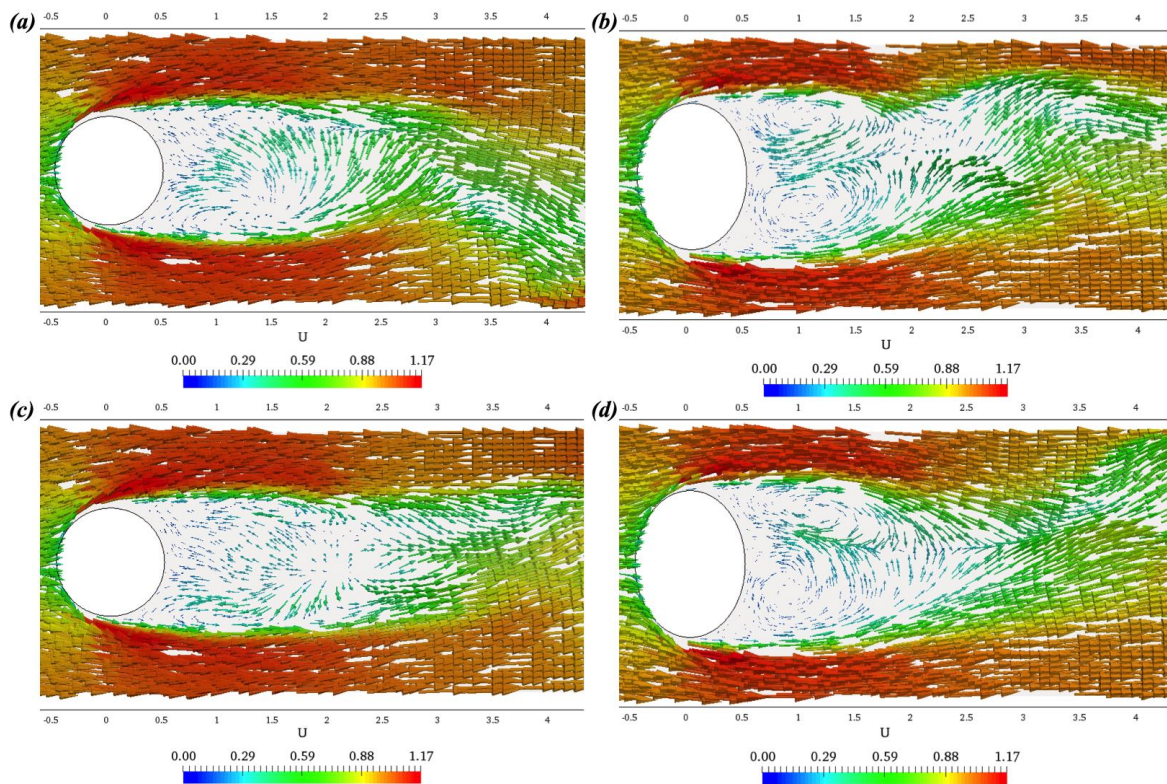
D.8 Time Series of Velocity at Re = 500

Figure D.14: (Part 1 of 2) Time series of the near velocity field in the middle minor plane (left images) and middle major plane (right images). (a,b) t = t_0; (c,d) t = $t_0 + 1.82D/U_\infty$; (e,f) t = $t_0 + 3.64D/U_\infty$.

Figure D.15: (Part 2 of 2) Time series of the near velocity field in the middle minor plane (left images) and middle major plane (right images). (a,b) t = t_0 + 5.46D/U_∞; (c,d) t = t_0 + 7.28D/U_∞.

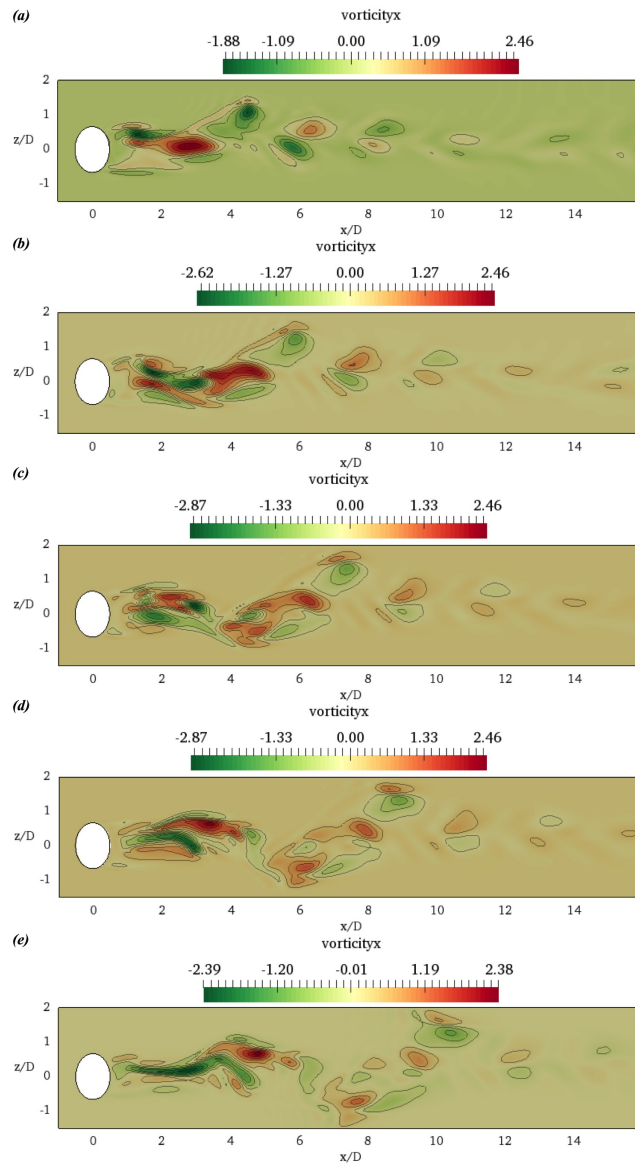# D.9 Time Series of Vorticity at Re = 500

Figure D.16: Time series of streamwise vorticity ω_x contours, in the middle (x,z)-plane. (a) t = t_0; (b) t = $t_0 + 1.82D/U_\infty$; (c) t = $t_0 + 3.64D/U_\infty$; (d) t = $t_0 + 5.46D/U_\infty$; (e) t = $t_0 + 7.28D/U_\infty$.
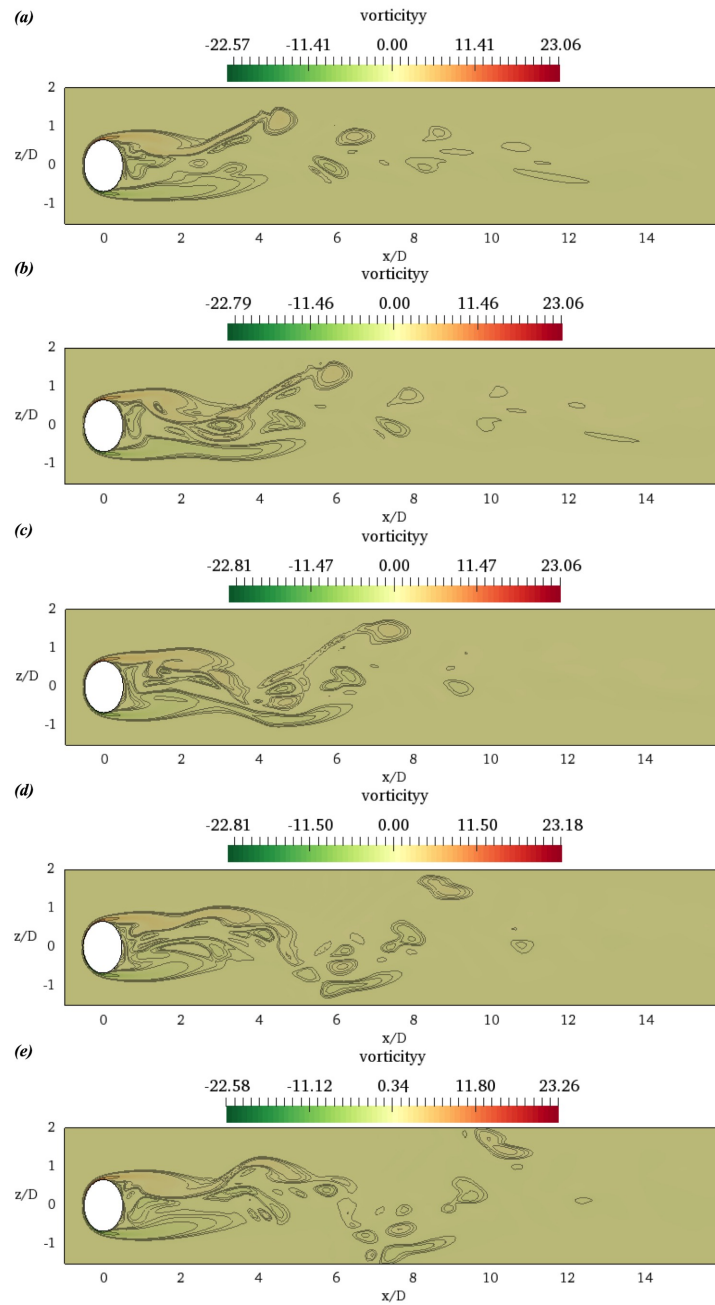
Figure D.17: Time series of transverse vorticity ω_y contours, in the middle (x,z)-plane. (a) t $= t_0$; (b) t $= t_0 + 1.82D/U_\infty$; (c) t $= t_0 + 3.64D/U_\infty$; (d) t $= t_0 + 5.46D/U_\infty$; (e) t $= t_0 + 7.28D/U_\infty$.
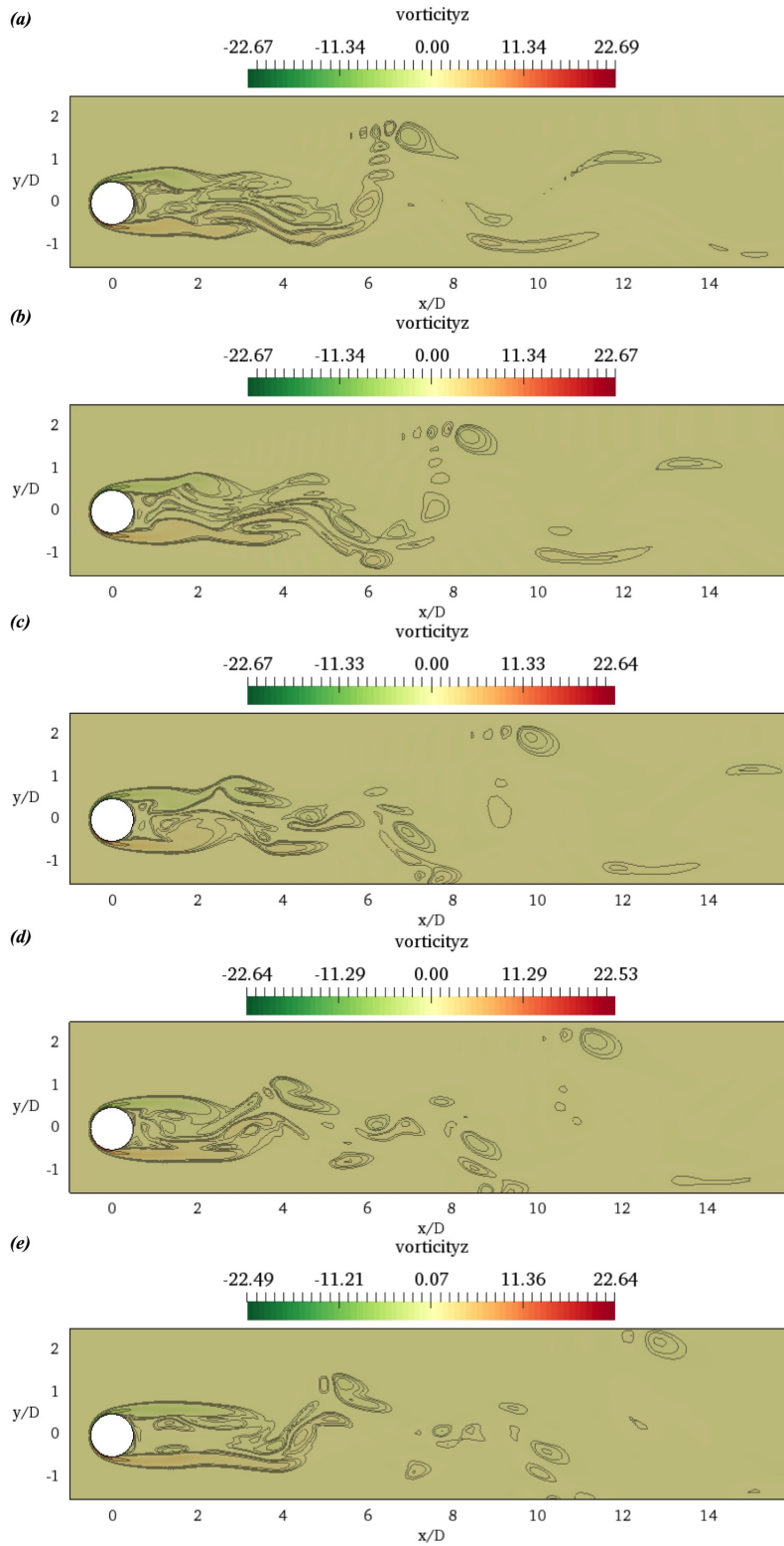
Figure D.18: Time series of transverse vorticity ω_z contours, in the middle (x,y)-plane. (a) t $= t_0$; (b) t $= t_0 + 1.82D/U_\infty$; (c) t $= t_0 + 3.64D/U_\infty$; (d) t $= t_0 + 5.46D/U_\infty$; (e) t $= t_0 + 7.28D/U_\infty$.